UNIVERSITY OF CALIFORNIA

Santa Barbara

The Genome-wide Elucidation of Genes Involved in Peroxisome Homeostasis and its Consequences on Interlinked Cell Regulation Pathways

A dissertation submitted in partial satisfaction

of the requirements for the Degree Doctor of Philosophy

in Biochemistry and Molecular Biology

by

Jonathan Thieng Vu

Committee in charge:

Professor Brooke Gardner, Co-Chair

Professor Chris Richardson, Co-Chair

Professor Joel Rothman, Co-Chair

Professor Meghan Morrissey

Professor Christopher Hayes

September 2024

The dissertation of Jonathan Thieng Vu is approved.

_____

Meghan Morrisey

_____

Christopher Hayes

_____

Brooke Gardner, Committee Co-Chair

_____

Chris Richardson, Committee Co-Chair

_____

Joel Rothman, Committee Co-Chair

June 2024

Copyright © 2024

by

Jonathan Thieng Vu

ACKNOWLEDGMENTS

With deep gratitude for

Kristina, Julija, Toai, and Sid,

whose love, friendship, and understanding are the astral beacons

that give warmth to this aphotic void,

and for Chris and Brooke,

for their patience, mentorship, and kindness,

and for giving this fatuitous reprobate

a chance.

VITA OF JONATHAN THIENG VU
June 2024

EDUCATION

Bachelor of Science in Biochemistry and Molecular Biology, University of California, Davis, June 2015
Doctor of Philosophy in Biomolecular Sciences and Engineering, University of California, Santa Barbara, June 2024 (expected)

PROFESSIONAL EMPLOYMENT

2015-2016: Manufacturing Technician, Genentech
2016-2017: Research Associate, Joint BioEnergy Institute LBNL
2018-2019: Research Associate, CellFE, Inc.
2016-2019: Staff Research Associate, Corn Lab, Innovative Genomics Institute

PUBLICATIONS

Vu, J. T., Tavasoli, K. U., Sheedy, C. J., Chowdhury, S.P., Mandjikian, L., Bacal, J., Morrissey, M. A., Richardson, C. D., Gardner, B. M. (2024). A genome-wide screen links peroxisome regulation with Wnt signaling through RNF146 and tankyrase. in press at Journal of Cell Biology 2024.05.30.578667.

Shin, J. J., Schröder, M. S., Caiado, F., Wyman, S. K., Bray, N. L., Bordi, M., Dewitt, M. A., Vu, J. T., Kim, W.-T., Hockemeyer, D., Manz, M. G., & Corn, J. E. (2020). Controlled Cycling and Quiescence Enables Efficient HDR in Engraftment-Enriched Adult Hematopoietic Stem and Progenitor Cells. Cell Reports, 32(9), 108093.

Wienert, B., Wyman, S. K., Richardson, C. D., Yeh, C. D., Akcakaya, P., Porritt, M. J., Morlock, M., Vu, J. T., Kazane, K. R., Watry, H. L., Judge, L. M., Conklin, B. R., Maresca, M., Corn, J. E. (2019) Unbiased detection of CRISPR off-targets in vivo using DISCOVER-Seq. Science, 364(6437), 286-289.

Chung, J. E., Magis, W., Vu, J., Heo, S.-J., Wartiovaara, K., Walters, M. C., Kurita, R., Nakamura, Y., Boffelli, D., Martin, D. I. K., Corn, J. E., & DeWitt, M. A. (2019). CRISPR-Cas9 interrogation of a putative fetal globin repressor in human erythroid cells. PLOS ONE, 14(1), e0208237.

Chen, Y., Vu, J., Thompson, M. G., Sharpless, W. A., Chan, L. J. G., Gin, J. W., Keasling, J. D., Adams, P. D., & Petzold, C. J. (2019). A rapid methods development workflow for high-throughput quantitative proteomic applications. PLOS ONE, 14(2), e0211582.

AWARDS

UCSB 25th MCDB/BMSE Retreat and Symposium Short Talk Award, 2022
Connie Frank Fellowship, 2021

ABSTRACT

The Genome-wide Elucidation of Genes Involved in Peroxisome Homeostasis and its Consequences on Interlinked Cell Regulation Pathways

by

Jonathan Thieng Vu

Peroxisomes are compartmentalized membrane-bound organelles evolved to enable cells to metabolically adapt to their environment, that are themselves near omnipresent throughout eukarya. In humans, peroxisomes are essential for normal development, insofar that peroxisome dysfunction causes both pre- and post-natal mortal insufficiencies that would disbar one from addressing the vicissitudes of life; and yet there is a dearth of data detailing the genes governing peroxisome function and homeostasis. To this end, we executed a genome-wide CRISPRi screen to identify novel factors involved in peroxisomal homeostasis. We uncovered various genes that hold potential as novel regulators of peroxisomes, such as suppressor of cytokine signaling-3 (SOCS3), C2orf15, Insulin Degrading Enzyme (IDE), and Ring finger protein 146 (RNF146). Through rigorous inspection, we were able to classify SOCS3 as a spurious hit generated by off-target effects, while potentially developing a novel way to find Cas9 related off-targets. Contemporaneously, we found through study of C2orf15 that there were computational aberrations embedded in the sgRNA generation processes of our colleagues' CRISPRi library, leading us to the discovery that Mitochondrial Ribosomal Protein L30 (MRPL30) modulates peroxisome abundance. Our dual-screen experiments then showed that IDE resembled a profligate peroxisome cargo regulator where its suppression strongly bolstered peroxisome matrix import, an antipodal effect relative to most peroxisome biogenesis gene

knockdowns. We chose to focus our efforts on RNF146, an E3 ligase with a predilection for poly(ADP-ribose), where its suppression caused an ebbing in the import function of peroxisomes. Loss of RNF146 caused peroxisome import malfunction by unfettered oversaturation of the poly(ADP-ribose) polymerases TNKS and TNKS2, which then bind, PARsylate, and impair peroxisomal proteins, chiefly PEX14. Because RNF146/TNKS/2 are more renowned for their connection to Wnt-signaling, mainly the degradation of AXIN1, a component of the destruction complex, we hypothesized that the peroxisome, via PEX14, would participate in the homeostatic equilibrium of RNF146/TNKS/2's proteasomal facilitations. We discovered that both loss of PEX14 and PEX19 destabilized AXIN1, as predicted, which subsequently compromised the steady-state levels of beta-catenin induced transcription. We then extrapolated these findings to other realms of developmental biology, mainly the Wnt-signaling influenced stem cell fate of neural progenitor cells (NPCs) and neural crest stem cells (NCSCs). Interestingly, our early results suggest that loss of PEX14 and PEX19 may bias the differentiation decision of stem cells similar to a loss in AXIN1, in line with our model. In totality, the consequences of our genome-wide screen, the collective observations, and various data paint a larger picture in which peroxisomes are interlinked to, and participate in, multifarious regulatory pathways of the cell.

TABLE OF CONTENTS

I. Introduction 1

II. A genome-wide screen links peroxisome regulation with Wnt signaling through RNF146 and TNKS/2 5

A. Sequestration of ZeoR in peroxisomes links peroxisome import to viability ... 5

B. A genome-wide CRISPRi screen in Pex-ZeoR cells enriches known PEX genes ..... **Error! Bookmark not defined.**

C. Guides targeting RNF146, INTS8, KCNN4 reduce peroxisomal foci intensity 11

D. RNF146 regulates peroxisome foci intensity in multiple cell lines 12

E. RNF146-mediated loss of mVenus-PTS1 foci depends on TNKS/2, but not autophagy 15

F. Loss of RNF146 specifically inhibits import into peroxisomes 20

G. PARP activity of TNKS/2 impedes import into peroxisomes 25

H. PEX proteins alter RNF146/TNKS/2 activity towards other substrates 29

I. Increased Wnt/beta-catenin signaling in PEX knockdown cells 30

III. The influence of PEX14/PEX19 stability on Wnt induced NPC/NCSC differentiation . 35

IV. Peroxisome homeostasis candidate - SOCS3 44

V. Peroxisome homeostasis candidate – C2orf15/MRPL30 50

VI. Peroxisome homeostasis candidate - IDE 53

Materials & Methods 67

References 80

LIST OF FIGURES

Figure 1. A genome-wide screen uncovers genes that regulate peroxisome biology 8

Figure S1 Genome-wide screen extended data 9

Figure 2. Peroxisome abundance is regulated locally by RNF146. 13

Figure S2 Secondary microscopy screen extended data 14

Figure 3. RNF146's effect on peroxisomes is mediated by TNKS/2, but not autophagy 17

Figure S3 Extended RNF146/TNKS/2 and autophagy data. 18

Figure 4. Loss of RNF146 impairs peroxisome protein import 21

Figure S4 Extended RNF146/TNKS/2 import and PEX14 interaction data 23

Figure 5. TNKS/2 PARP activity impairs peroxisome protein import. 27

Figure 6. Peroxisome abundance influences RNF146/TNKS substrate selection. 32

Figure S5 Extended H4 PEX KD AXIN1 stabilization data 34

Figure 7. PEX14/PEX19 expression and the iPSC developmental fate between NPCs/NCSCs 41

Figure 8. Dual screen strategy reveals and validates false-positive SOCS3 47

Figure 9. SOCS3 G1, but not SOCS3 G4, resembles a PEX19 KD 48

Figure 10. Peroxisome phenotype of SOCS3 G1 is based on PEX19 off-target activity 49

Figure 11. C2orf15 sgRNAs target the promoter region of MRPL30 causing increased peroxisomal foci 52

Figure 12. IDE KD causes increase in peroxisomal foci 62

Figure 13. IDE nominally suppresses peroxisome homeostasis via its catalytic activity and PTS1 tag 63

Figure 14. LC-MS/MS of IDE FLAG-IP does not reveal IDE peroxisome regulator target 64

Figure 15. IDE overlaps with peroxisomes but does not have singular localization to the peroxisomal matrix 65
Figure 16. IDE does not strongly modulate PEX5 or PTS1 cargo stability but modulates localization 66

I. Introduction

Note: Some figures, methods, and discussion from this chapter have been previously published in ©Vu et al (2024) and are reproduced here under the Creative Commons Attribution License.

The peroxisome is a membrane-bound organelle that harbors enzymes for specialized metabolic reactions. The most conserved peroxisomal functions include the beta-oxidation of fatty acids and regulation of reactive oxygen species [Wanders and Waterham 2006]; however, cells tune peroxisome function according to need. For example, peroxisomes in the large intestine of mice contain enzymes for optimal plasmalogen synthesis, while peroxisomes in the small intestines contain enzymes for optimal beta-oxidation of fatty acids [Morvay et al 2017]. Peroxisome function differentiates alongside cell type: for example, in inner ear cells, sound-induced autophagy of peroxisomes protects against noise overexposure [Defourny et al 2019], while in macrophages, peroxisomal metabolism improves phagocytosis [Di Cara et al 2017]. Accordingly, mutations in peroxisomal genes in humans cause a spectrum of Peroxisome Biogenesis Disorders (PBDs) with phenotypes ranging in severity from early infant mortality, developmental abnormalities, and liver dysfunction to more specific metabolic syndromes, sensorineural hearing loss, and retinal degeneration [Braverman et al 2016]. It is therefore important to know both the genes dedicated to peroxisome function in human cells, as well as the mechanisms by which peroxisome abundance and function are coordinated to meet the needs of cell.

The steady state level of peroxisomes is a balance of *de novo* biogenesis, fission of existing peroxisomes, and degradation by peroxisome-specific autophagy. In *de novo*

biogenesis, membranes and peroxisomal membrane proteins bud in pre-peroxisomal vesicles from either the endoplasmic reticulum and/or mitochondria. The fusion of these vesicles forms an import-competent peroxisome, which matures through the import of proteins from the cytosol bearing one of two peroxisome targeting signals. The receptor PEX5 binds the common C-terminal tri-peptide peroxisome targeting signal (PTS1), and subsequently binds PEX13/PEX14 at the peroxisome membrane and mediates translocation of the PTS1-tagged protein fully folded across the membrane (Dammai et al 2001). The PEX7 receptor recognizes the more rarely used N-terminal peroxisome targeting signal (PTS2) and through binding to a PEX5-like protein, feeds into a similar translocation process (Braverman et al 1997). During import of PTS-tagged proteins, PEX5 becomes embedded in the membrane. Following ubiquitination by the PEX2/PEX10/PEX12 E3 ligase complex, the PEX1/PEX6/PEX26 complex extracts PEX5 from the membrane for subsequent cycles of import (Platta et al. 2009, Platta et al. 2005). Peroxisomes can also proliferate through growth and division. PEX11, in collaboration with mitochondrial fission proteins DRP1, FIS1, and MFF, facilitates fission of existing peroxisomes (Koch et al. 2010, Titorenko et al. 2001). Finally, peroxisomes can be targeted for peroxisome-specific autophagy by numerous adaptor proteins, including NBR1, SQSTM1 (p62), and MARCH5 (Kim et al 2008, Deosaran et al 2013, Zheng et al 2021). Peroxisome-specific autophagy is triggered either by peroxisome dysfunction, such as the accumulation of ubiquitinated PEX5 at the peroxisome membrane (Nuttall et al. 2014), or in response to external stimuli, such as oxidative stress (Zhang et al. 2015) or nutrient depletion (Luiken et al. 1992).

Many of the *PEX* genes were originally identified through genetic screens in fungi where growth on methanol or oleic acid depends upon peroxisome function [van Zutphen et

al. 2010, Elgersma et al. 1996), and through genetic studies on cells from patients with Peroxisome Biogenesis Disorders (Wanders et al. 2004, Mignarri et al. 2012, Matsui et al. 2012, Thoms et al. 2012). In mammalian cells, the discovery of genes that influence peroxisome homeostasis is ongoing: MARCH5 was recently identified as an E3 ligase contributing to peroxisome-specific autophagy (Zheng et al 2021); MCTP2 was recently identified as a factor controlling pre-peroxisomal vesicle budding from the endoplasmic reticulum (Joshi et al 2018). More recently, screens in human cells for genes conferring increased resistance to hydrogen peroxide or low oxygen conditions have also enriched for known *PEX* genes, (Dubreuil et al. 2020; Jain et al. 2020), although the identification of genes involved in peroxisome homeostasis was not the direct focus of these screens. Thus, while we know some of the factors contributing to peroxisome homeostasis in mammalian cells, there are likely to be additional factors and specific regulatory mechanisms specific to mammalian cells yet to be identified.

Here we performed a genome-wide CRISPRi screen, coupled with a secondary microscopy screen, in human cells to identify genes that influence the import of proteins targeted to peroxisomes. We confirmed that our screen was successful when a majority of known *PEX* genes were enriched by our strategy, giving us reason to pursue candidate genes. Briefly, we found that suppression of SOCS3 caused near total loss of peroxisomal foci, similar to a PEX19 knockdown, mainly because one sgRNA, SOCS3 G1 targeted PEX19 as an off-target. We also found that the sgRNAs ostensibly targeting C2orf15 actually targeted MRPL30, which had an effect of increasing peroxisome proliferation. Furthermore, a very robust hit that had effervesced out of the dual screens was IDE, where its suppression caused brighter and more numerous peroxisomal foci. In addition, we found

that knockdown of the E3 ligase RNF146 reduces import of PTS1-tagged proteins into the peroxisome, resembling other *PEX* gene KDs, which motivated our decision to focus on RNF146 as our main candidate gene. RNF146 (Ring Finger Protein 146), also known as Iduna, is a RING-domain E3 ubiquitin ligase that recognizes and ubiquitinates proteins modified by poly(ADP-ribosyl)ation (PARsylation) [Zhang et al. 2011, DaRosa et al. 2015]. RNF146 interacts directly with poly(ADP-ribose) polymerases, such as tankyrase-1 and tankyrase-2 (TNKS and TNKS2, referred to here as TNKS/2 together) [Da Rosa et al. 2015] and PARP1 and PARP2 [Gero et al 2014, Kang et al 2011]. Together, the poly(ADP-ribose) polymerases and RNF146 specifically regulate the stability of numerous substrates which are first PARsylated and subsequently polyubiquitinated by RNF146, triggering proteasomal degradation. We found that RNF146-mediated loss of peroxisomes was dependent on the accumulation of the poly(ADP-ribose) polymerases TNKS/2, specifically by impairing import into peroxisomes through a mechanism dependent on TNKS/2's activity as poly(ADP-ribose) polymerases. We thus propose a model in which TNKS/2 binds and PARsylates PEX14 and neighboring proteins, inhibiting the import of PTS1-tagged proteins.

RNF146 and TNKS/2 are better known as co-regulators of protein stability: TNKS/2 binds and PARsylates substrates with a tankyrase-binding motif (TBM), which then triggers poly-ubiquitination by RNF146 [DaRosa et al 2015]. Known RNF146/TNKS/2 substrates include AXIN1, BLZF1, 3BP2, and CASC3 [Nie et al 2020, Levaot et al 2011]. Surprisingly, we found that in a variety of cell lines, a loss of *PEX* genes altered the stability of RNF146/TNKS/2 substrates and could therefore alter the output of downstream signaling pathways, including the Wnt/beta-catenin pathway. These observations suggest that not only

is peroxisome abundance and function integrally intertwined with cell signaling pathways, but also that peroxisomes themselves regulate cellular responses to external stimuli.

II. A genome-wide screen links peroxisome regulation with Wnt signaling through RNF146 and TNKS/2.

Note: Some figures, methods, and discussion from this chapter have been previously published in ©Vu et al (2024) and are reproduced here under the Creative Commons Attribution License.

A. Sequestration of ZeoR in peroxisomes links peroxisome import to viability.

Past screens for peroxisomal genes in mammalian cells have relied on peroxisome-localized enzymatic activity [Zoeller and Raetz 1986, Tsukamoto et al 1990; Morand et al. 1990] and fluorescence microscopy of PTS1-tagged fluorescent proteins [Ito et al 2000], since mammalian cells in tissue culture conditions do not require peroxisomes for growth. To facilitate a CRISPRi screening approach for regulators of peroxisome function, we engineered a cell line, which we term Pex-ZeoR, in which the efficiency of peroxisome import is linked to cell viability by fusing the fluorescent marker mVenus and a peroxisomal targeting signal (PTS1) to the gene encoding resistance to Zeocin, a 1400 Dalton molecule in the bleomycin family that induces DNA double strand breaks and causes cell death [Murray et al 2014; Drocourt et al 1990]. With this fusion construct, mVenus-ZeoR-PTS1, cells with functional peroxisomes should sequester the Zeocin resistance protein (ZeoR), thereby preventing them from neutralizing Zeocin, which is too large to passively diffuse through peroxisome membranes [Antonenkov and Hiltunen 2006]. By contrast, cells with reduced peroxisome import should accumulate mVenus-ZeoR-PTS1 in the cytoplasm where

it can neutralize Zeocin, conferring a selective advantage in the presence of Zeocin **(Fig. 1A**). To affirm our strategy, we transduced HCT116 CRISPRi (dCas9-KRAB) cells [Liang et al 2018; Gilbert et al 2014] to recombinantly express mVenus-ZeoR-PTS1. As predicted, cells expressing a non-targeting control (NTC) sgRNA had fluorescent mVenus foci, while cells expressing a *PEX1* targeting sgRNA exhibited diffuse cytosolic mVenus signal (**Fig. 1B**), consistent with mVenus-ZeoR-PTS1 targeting to the peroxisome. We then assessed cell growth of the HCT116 CRISPRi Pex-ZeoR cell line over a range of Zeocin concentrations, finding a clear growth advantage for cells with sgRNAs targeting *PEX1* or *PEX6* versus NTC at high concentrations of Zeocin (**Fig. S1A**). To identify optimal selection conditions for the genome-wide screen, we performed a competition assay by co-culturing either PEX1 or PEX6 CRISPRI Pex-ZeoR cells with NTC CRISPRi Pex-ZeoR cells at varying dosages of Zeocin, and monitoring the abundance of each cell population by flow cytometry. *PEX1* and *PEX6* knockdown cells started at 5-10% of the cell population and were outcompeted by NTC cells in conditions without Zeocin. However, they displayed a marked competitive advantage in the presence of Zeocin (**Fig. 1C, Fig. S1B**). Together, these validation experiments suggest that peroxisomal sequestration of ZeoR allows for the selection of cells harboring sgRNAs that target peroxisomal genes.

B. A genome-wide CRISPRi screen in Pex-ZeoR cells enriches known PEX genes.

Emboldened, we executed a genome-wide screen with the Pex-ZeoR cell line to identify novel genes that affect peroxisomal homeostasis. Infection with a genome-wide CRISPRi library was followed by chronic treatment with or without Zeocin, combined with regular

passaging of cells over 35 days, with samples collected every 7 days for terminal Illumina sequencing preparation (**Fig. S1C**). We found 1,717 genes that were significantly different ($p<0.05$) between the treated and untreated conditions at the day 14 timepoint (**Fig. 1D**). Day 14 serves as the optimal comparison timepoint because of clear enrichment of the majority of known PEX genes while maintaining sufficient library diversity and replicate quality (**Fig. S1D, S1E**).

We observed enrichment of guides targeting known PEX genes that facilitate PTS1 import (PEX5, PEX13, PEX14, PEX2/PEX12, PEX1/PEX6, PEX26) and peroxisome membrane protein targeting (PEX19) affirming the efficacy of our strategy (**Fig. 1D**). Guides targeting PEX7 and alpha and beta variants of PEX11 were not strongly enriched, consistent with roles in recognition of the alternative PTS2 targeting signal (PEX7) [Braverman et al 1997], and peroxisomal membrane elongation (PEX11) [Koch et al 2010]. Guides targeting one component of the peroxisome RING finger complex, PEX10, were not enriched compared to the other constituents, PEX2 and PEX12, and guides targeting other peroxisome membrane biogenesis factors PEX3 and PEX16, were depleted in the screen (**Fig. 1D, S1E**). While initially unexpected, these results align with recent data that PEX10 and PEX16 CRISPR/Cas knockouts display only partial peroxisomal import defects (Yagita et al 2022; Ott et al 2023). Of the known factors regulating peroxisome specific autophagy, such as NBR1, MARCH5, SQSTM1, HIF1A, and NIX [Kim et al 2008, Deosaran et al 2013, Zheng et al 2022, Wilhelm et al 2022], we found that only guides targeting HIF1A, the loss of which stabilizes peroxisomes [Wilhelm et al 2022], were strongly depleted in our screen. Although most peroxisome-homeostasis related genes behaved according to our predictions, a handful did not align with our a priori prognosis. Our results suggest the

possibility that not all of the aforementioned genes are simple or monotonic in their effect on peroxisome import or autophagy, representing potential new mechanisms for further investigation.

Figure 1

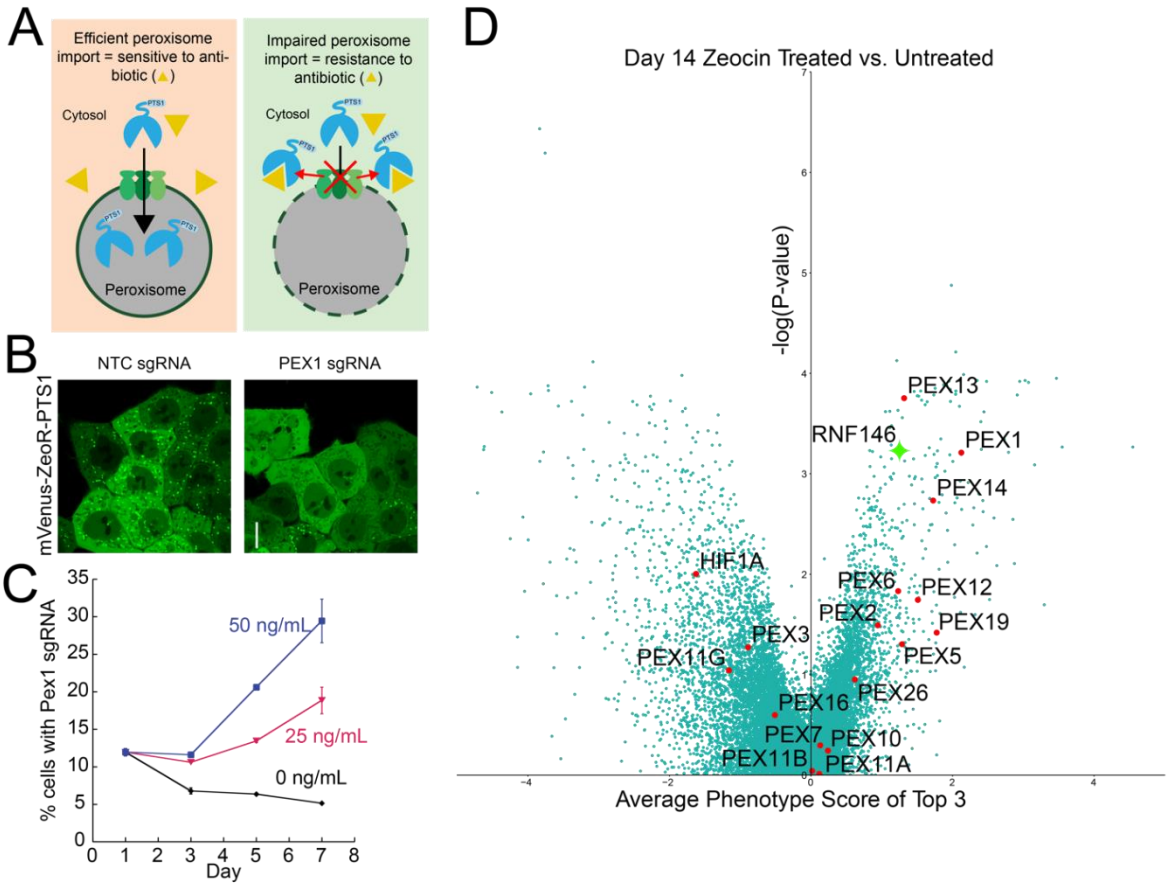

Figure 1. A genome-wide screen uncovers genes that regulate peroxisome biology. (A) Design of the Pex-ZeoR cell line, which sequesters the Zeocin resistance protein in the peroxisome matrix. Loss of PEX genes causes cytosolic Zeocin resistance. **(B)** Representative fluorescence microscopy images of live HCT116 mVenus-ZeoR-PTS1 cells expressing either NTC or PEX1 sgRNAs. Fusion construct forms puncta in WT but not aperoxisomal (PEX1 knockdown) cells. Fluorescent microscopy data are representative of n=49 images from m=2 biological replicates. Scale bar: 10μm **(C)** Quantification of flow cytometry data of BFP- (NTC) and BFP+ (PEX1) cells grown in co-culture competition assay over t=11 days in the presence of 0, 25, or 50 ng/uL of Zeocin. Timepoints are taken every t=2 days. Data shown as the mean ± SD of n=3 biological replicates. **(D)** Volcano plot of NGS data from genome-wide screen with significance (-log base 10 of p-value, y-axis) and phenotype score (normalized fold change of cDNA guide count, x-axis) of guides targeting specific genes for cell cultures either untreated (DMSO mock treated) or treated (50ng/uL Zeocin treated) for 14 days. Red data points represent known PEX genes and HIF1A. The green data point represents RNF146. Data displayed was calculated from m=3 guides per gene and n=2 biological replicates.

Supplementary Figure 1

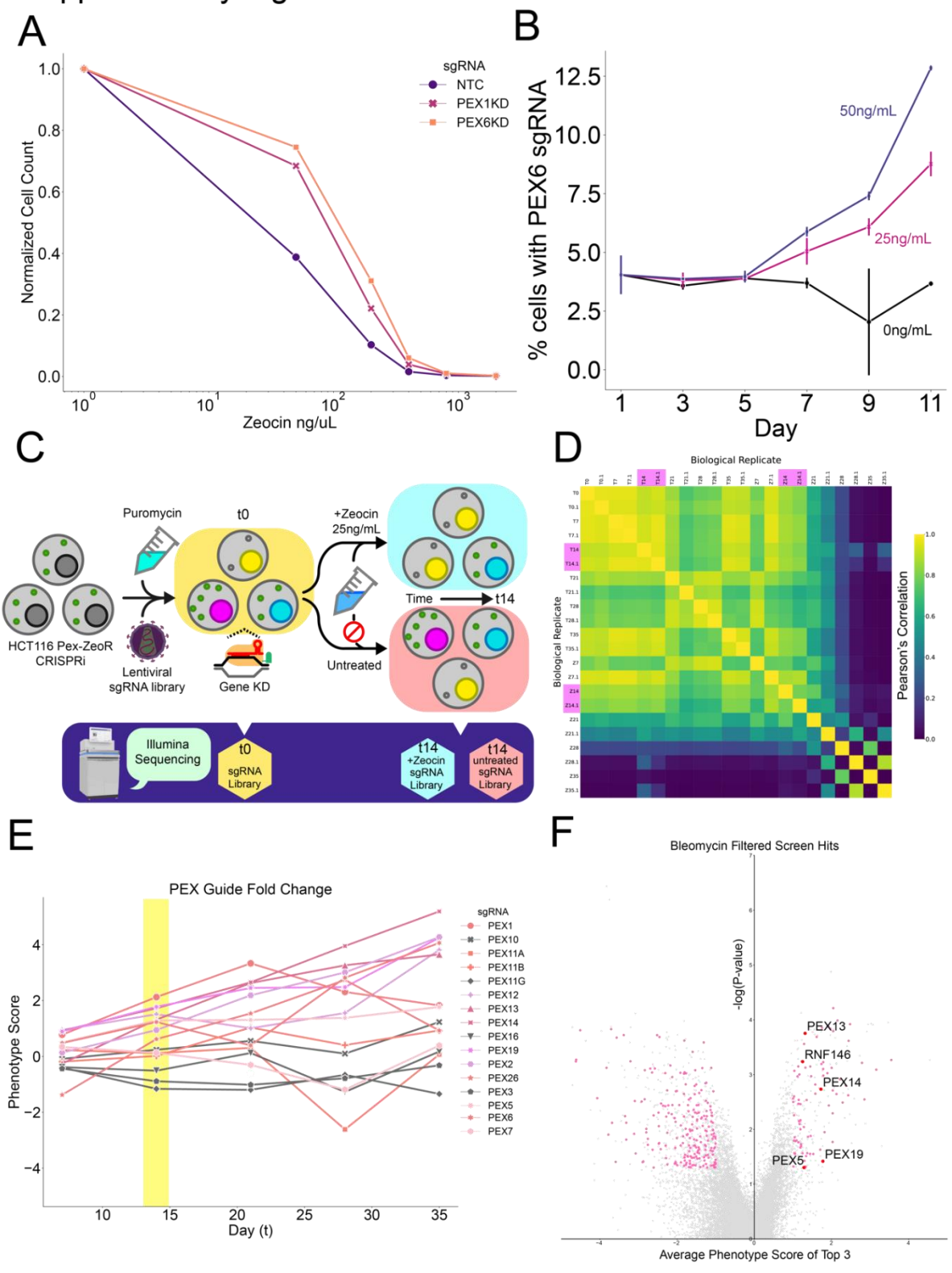

Figure S1. (A) Quantification of cell count by flow cytometry in different concentrations of Zeocin of HCT116 cells with sgRNAs targeting NTC, PEX1, or PEX6, over 72 hrs. Data is representative of n=2 biological replicates. Cell count is normalized to untreated. **(B)** Quantification of flow cytometry data of BFP- (NTC) and BFP+ (PEX6) cells grown in co-culture competition assay over t=11 days in the presence of 0, 25, or 50 ng/uL of Zeocin. Timepoints are taken every t=2 days. Data shown as the mean ± SD of n=3 biological replicates. **(C)** Schematic of the CRISPRi screen. Pex-ZeoR cells were transformed with a genome-wide gRNA library, selected for expression of guides, and split into untreated and +Zeocin growth conditions. Genomic DNA takedowns for NGS sequencing at t=0 and t=7x for all conditions. **(D)** Heatmap showing Pearson's correlation coefficient of guide abundance for all library elements between biological replicates of sequenced timepoints between treated and untreated conditions. T and Z represent untreated and Zeocin treated conditions, respectively, while numbers represent timepoint (days). Highlighting indicates comparisons between day 14 samples. **(E)** Fold change of various PEX sgRNA abundances derived from genome-wide CRISPRi screen comparing Zeocin treated to untreated samples. Highlighting indicates comparisons between day 14 samples. Y-axis is phenotype score, a measure of fold change of 3 of 5 significant guides per gene. X-axis is time (t) in days. Data is representative of n=2 biological samples. **(F)** Volcano plot of NGS data from genome-wide screen with significance (-log base 10 of p-value, y-axis) and phenotype score (normalized fold change of cDNA guide count, x-axis) of guides targeting specific genes for cell cultures either untreated (DMSO mock treated) or treated (50ng/uL Zeocin treated) for 14 days. Pink data points are output genes filtered through the Olivieri et al. Bleomycin screen that also have p-value <.05 and minimum phenotype score of 1. Gray data points are genes that did not pass filter. Red data points represent known PEX genes and RNF146. Data displayed was calculated from m=3 guides per gene and n=2 biological replicates.

C. Guides targeting RNF146, INTS8, KCNN4 reduce peroxisomal foci intensity.

We anticipated that sgRNAs that improve resistance to Zeocin independent of the peroxisomal localization of ZeoR should also be significantly enriched in our dataset. Thus, to narrow the candidate list to genes relevant to peroxisomal localization of ZeoR, we filtered our screen results to exclude factors that modulated resistance to a related DNA damaging agent, bleomycin [Olivieri et al 2020] (**Fig. S1F, Table S1**, Z-score range [-0.5,0.5]). GO analysis of the remaining genes with a fold change greater than 2 and a Mann-Whitney $p<0.05$ revealed a 100-fold enrichment of GO terms related to protein import into the peroxisome, and a greater than 20-fold enrichment related to RNA cleavage involved in mRNA processing (**Table S2**). We note that several *PEX* genes (*PEX1*, *PEX6*, *PEX12*) modulate bleomycin resistance, possibly because there is a direct link between DNA repair and peroxisome biology through localization of the DNA repair kinase ATM to peroxisome membranes [Zhang et al 2015].

We then used fluorescence microscopy of mVenus-PTS1 in the Pex-ZeoR cell line to assess how knockdown of candidate genes altered peroxisome abundance. For each candidate gene, we produced two unique constitutive knockdown cell lines per gene and quantified mVenus-PTS1 foci number, foci and cell area, and foci and cytoplasm fluorescence intensity using CellProfiler [Stirling et al. 2021]. To estimate the efficiency of peroxisome import while accounting for different mVenus-PTS1 expression levels, we calculated the ratio of the intensity of mVenus-PTS1 in peroxisome foci to the intensity of mVenus-PTS1 in the cytoplasm (**Fig. 2A, S2A, S2B, S2C**). We found that several of the guides enriched by Zeocin selection decreased the ratio of peroxisomal to cytosolic

mVenus-PTS1 intensity, including those targeting the E3 ligase RNF146, Integrator complex subunit INTS8, and calcium-activated potassium channel KCNN4 (**Fig. 2A**).

D. RNF146 regulates peroxisome foci intensity in multiple cell lines.

Given the magnitude of the impact of the RNF146 knockdown on mVenus-PTS1 foci (**Fig. 2A, 2B**), we chose to focus our efforts on characterizing the effects of RNF146 on peroxisome homeostasis. We first ruled out possible off-target effects of the RNF146 sgRNA by treating our reporter cell line with RNF146 siRNA, which recapitulated the loss of mVenus foci signal within 24 hours of siRNA treatment (**Fig. 2C**). To determine if the peroxisomal effect of RNF146 knockdown was specific to the HCT116 cell line, we created a secondary cell line, the H4 astrocytoma cancer cell line, harboring the same CRISPRi machinery and our Pex-ZeoR reporter. We observed significant depletion of mVenus-PTS1 foci intensity in both the HCT116 and H4 *RNF146* and *PEX* knockdown cell lines (**Fig. 2B, 2D**). The significant depletion of PTS1 foci in two independent cell lines suggests that RNF146 has a bona fide role in regulating peroxisome homeostasis in human cells.

To determine if *RNF146* KD impacted peroxisome biogenesis through an effect on *PEX* gene expression, we gathered RNA-seq data of *RNF146* KD HCT116 cell mRNA transcripts versus NTC cells. We found that knockdown of *RNF146*, which was confirmed in the data set, mildly repressed transcription of *PEX3* and *PEX10*. Given that neither *PEX3* nor *PEX10* had positive phenotype scores in the CRISPRi screen, we found it unlikely that the RNF146 phenotype can be completely explained by these transcriptional changes, thereby indicating a post-transcriptional role for RNF146 in regard to peroxisomal homeostasis (**Fig. 2E**).

Figure 2

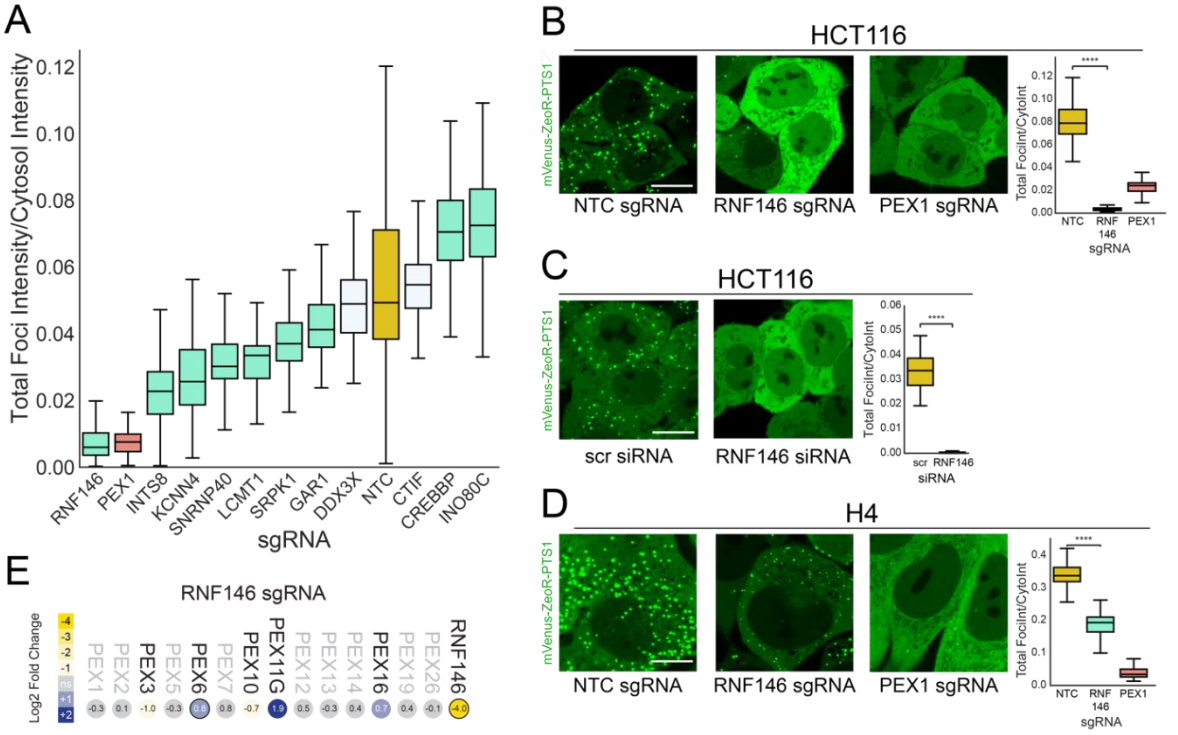

Figure 2. Peroxisome abundance is regulated locally by RNF146. (A) CellProfiler quantification of the ratio of mVenus-PTS1 intensity in foci and in the cytoplasm in fluorescence microscopy images acquired of live HCT116 Pex-ZeoR cells expressing sgRNAs targeting various genes. Data per gene constitutes m=2 unique sgRNAs with n=49 images per gene. Non-targeting control sgRNA shown in yellow, PEX1 sgRNA shown in pink, sgRNAs significantly different from NTC ($p<0.0001$, independent t-test) are in blue, sgRNA with $p>0.05$ are in white. **(B)** Representative fluorescence microscopy images of mVenus expression in HCT116 Pex-ZeoR cells harboring sgRNAs for NTC, PEX1, or RNF146 and quantification of the ratio of mVenus-PTS1 foci intensity to mVenus-PTS1 cytosolic intensity. Data is representative of m= 49 images. n=2 biological replicates. Scale bars: 10 µm. **(C)** Representative fluorescence microscopy images of mVenus expression in HCT116 Pex-ZeoR cells treated with either scrambled (scr) siRNA or RNF146 siRNA, and quantification of the ratio of total mVenus-PTS1 foci intensity to mVenus-PTS1 cytosolic intensity. Data is representative of m= 49 images n=2 biological replicates. Scale bar: 10 µm. **(D)** Representative fluorescence microscopy images of mVenus expression in H4 Pex-ZeoR cells harboring sgRNAs for NTC, PEX1, or RNF146 and quantification of the ratio of mVenus-PTS1 foci intensity to mVenus-PTS1 cytosolic intensity. Data is representative of m= 49 images. n=2 biological replicates. Scale bars: 10µm. Asterisks denote ****$p<0.0001$. **(E)** Heatmap of RNA-seq data displaying significant ($p<0.05$) fold change of *PEX* gene transcription in RNF146 knockdown cells versus NTC controls. Data is representative of n=3 biological replicates.

Supplementary Figure 2

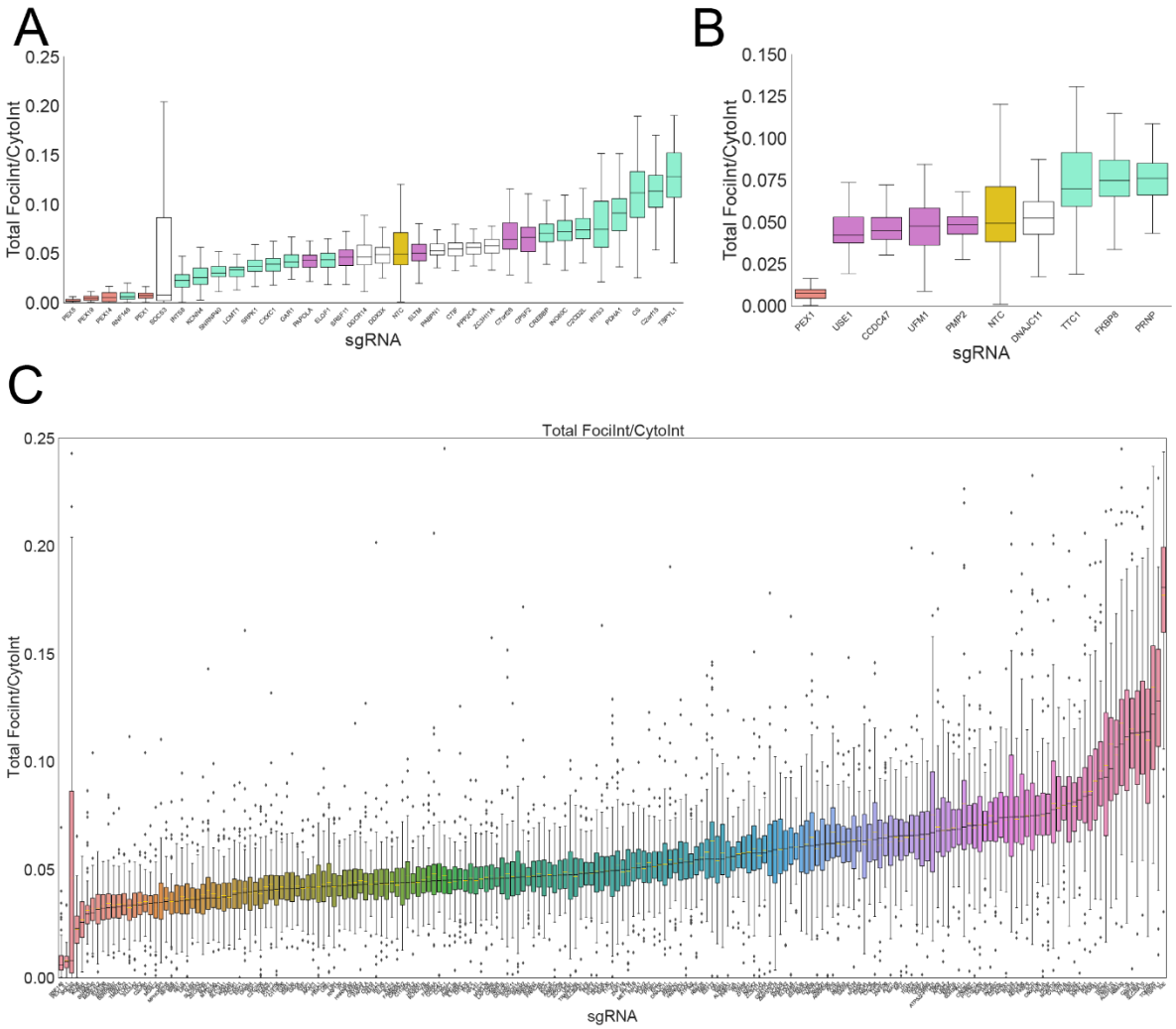

Supplementary Figure 2. (A)(B)(C) Additional data as in Figure 2A CellProfiler quantification of the ratio of mVenus-PTS1 intensity in foci and in the cytoplasm in fluorescence microscopy images acquired of live HCT116 Pex-ZeoR cells expressing sgRNAs targeting various genes. **(A)** Positive phenotype score genes from the primary genetic screen. **(B)** Negative phenotype score genes from the primary genetic screen. **(C)** All genes tested from the primary genetic screen. Data per gene constitutes m=2 unique sgRNAs with n=49 images per gene. Non-targeting control sgRNA shown in yellow, PEX1 sgRNA shown in pink, sgRNAs significantly different from NTC are in blue ($p<0.0001$, independent t-test) or purple ($p<0.05$, independent t-test), and sgRNAs with $p>0.05$ are in white.

E. RNF146-mediated loss of mVenus-PTS1 foci depends on TNKS/2, but not autophagy.

RNF146 is known to collaborate with poly(ADP-ribose) polymerases to ubiquitinate PARsylated proteins and target them for degradation. Loss of RNF146 is therefore expected to stabilize PARsylated substrates, which could act to either inhibit peroxisome biogenesis or increase peroxisome-specific autophagy. We therefore tested if the observed loss of mVenus-PTS1 foci in response to RNF146 knockdown depended on changes in the RNF146 partners TNKS/2. We first assessed TNKS/2 levels in an RNF146 knockdown, and found that knockdown of RNF146 expression in the HCT116 Pex-ZeoR cell line caused a marked increase in TNKS/2 protein levels (**Fig. 3A**). To test if RNF146's effect on peroxisomes depended on increased TNKS/2 levels, we performed a dual knockdown assay of *RNF146* and *TNKS/2* in our reporter cell line. We found that siRNA knockdown of *TNKS and TNKS2* in RNF146 CRISPRi cells rescued the import of mVenus-PTS1 (**Fig. 3A, 3B**) indicating that RNF146's effect on peroxisomes depended on TNKS/2. In an extended assay, we attempted to swap the dual KD strategies of RNF146 and TNKS, such that only TNKS (and not TNKS2) was suppressed by CRISPRi, and RNF146 expression was suppressed by siRNA treatment. We observed that there was clear rescue in the TNKS CRISPRi and RNF146 siRNA treatment, but that this rescue was not as complete as the RNF146 CRISPRi and TNKS/2 siRNA treatment, suggesting that TNKS2 may also play a role in the RNF146 KD phenotype (**Fig. S3A**). These results are consistent with previous reports that TNKS is significantly stabilized in cells lacking RNF146 [Nie et al 2020]. Although it was previously shown that TNKS mediates peroxisome-specific autophagy [Li et al 2017], we found that siRNA inhibition of ATG7 did not prevent the accumulation of TNKS/2 nor the loss of

mVenus-PTS1 foci intensity in RNF146 knockdown cells **(Fig. 3C, 3D**). This lack of dependence on autophagy was further corroborated in multiple cell lines by the treatment of RNF146 knockdown cells with autophagy inhibitors bafilomycin or hydroxychloroquine, which, despite preventing LC3BII turnover, did not substantially rescue peroxisome foci number or intensity relative to control cells **(Fig. S3B-G)**. These observations suggest that while the effect of RNF146 knockdown on peroxisomes depends on TNKS/2, it does not depend on peroxisome-specific autophagy.

Figure 3

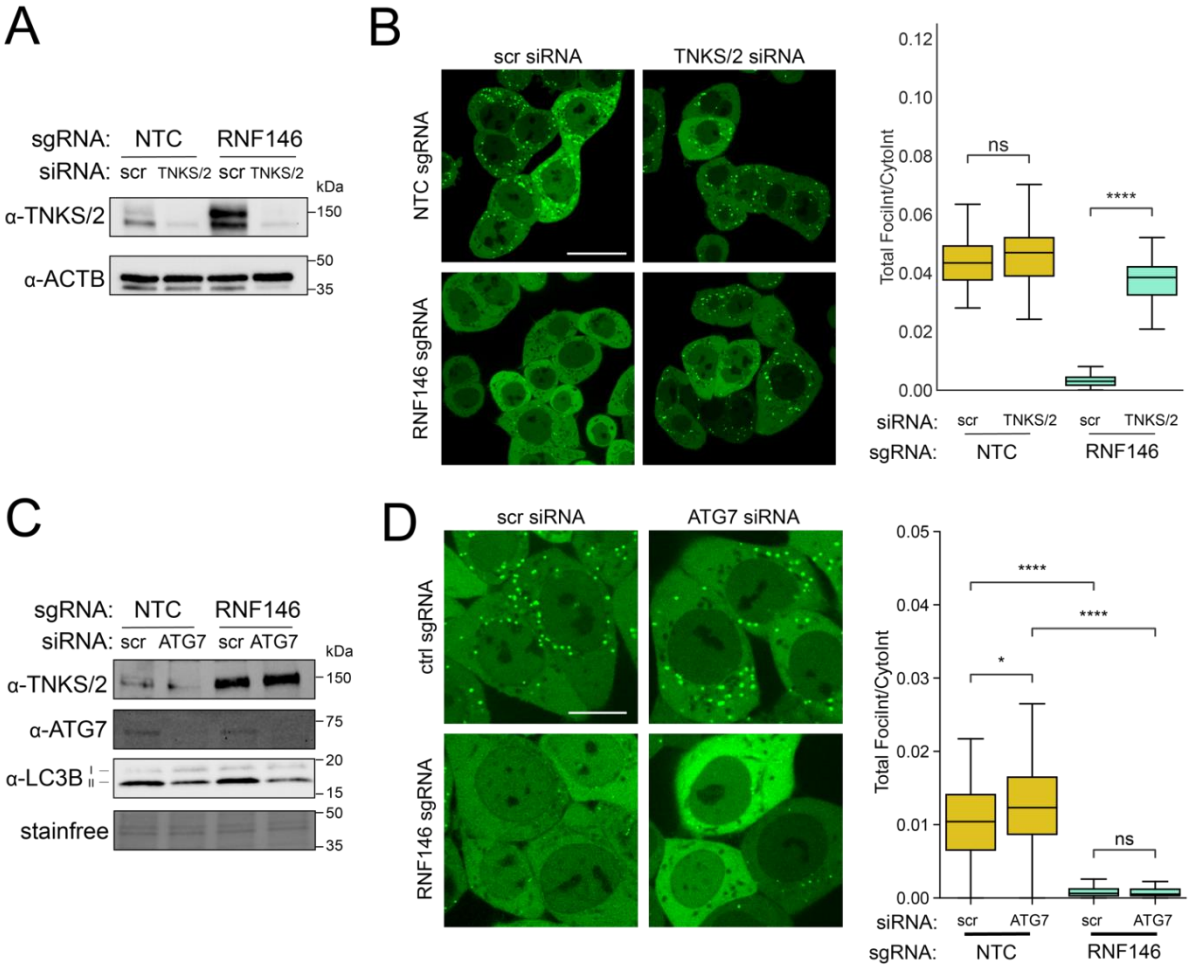

Figure 3. RNF146's effect on peroxisomes is mediated by TNKS/2, but not autophagy. (A) Immunoblots for TNKS/2 and ACTB (loading control) in lysate from scrambled or TNKS/2 siRNA treated HCT116 Pex-ZeoR cells with sgRNAs for either NTC or RNF146. **(B)** Left panel: Representative mVenus-PTS1 fluorescence microscopy images of either non-targeting control (NTC) or RNF146 sgRNA cells treated with either scrambled (scr) siRNA or TNKS siRNA. Right panel: Quantification of mVenus-PTS1 microscopy images in left panel for mVenus-PTS1 foci intensity versus total cytosol intensity in HCT116 Pex-ZeoR cells. Data is representative of 49 images per condition and 2 biological replicates. Scale bars: 10 μm. **(C)** Immunoblot for TNKS/2, ATG7, and LC3B in lysate from scrambled or ATG7 siRNA treated HCT116 Pex-ZeoR cells with sgRNAs for either NTC or RNF146. **(D)** Left panel: Fluorescence microscopy data of scrambled or ATG7 siRNA treated HCT116 Pex-ZeoR cells with sgRNAs for either non-targeting control (NTC) or RNF146. m=32 images. n=2 biological replicates. Right panel: Quantification of mVenus-PTS1 microscopy images for mVenus foci intensity versus cytosol intensity in HCT116 Pex-ZeoR cells. Scale bars: 10μm. All blots are representative of n=3 biological replicates. Asterisks denote p-values *p <0.05, ****p <0.0001, whereas ns denotes not significant, calculated by independent t-test.

Supplementary Figure 3

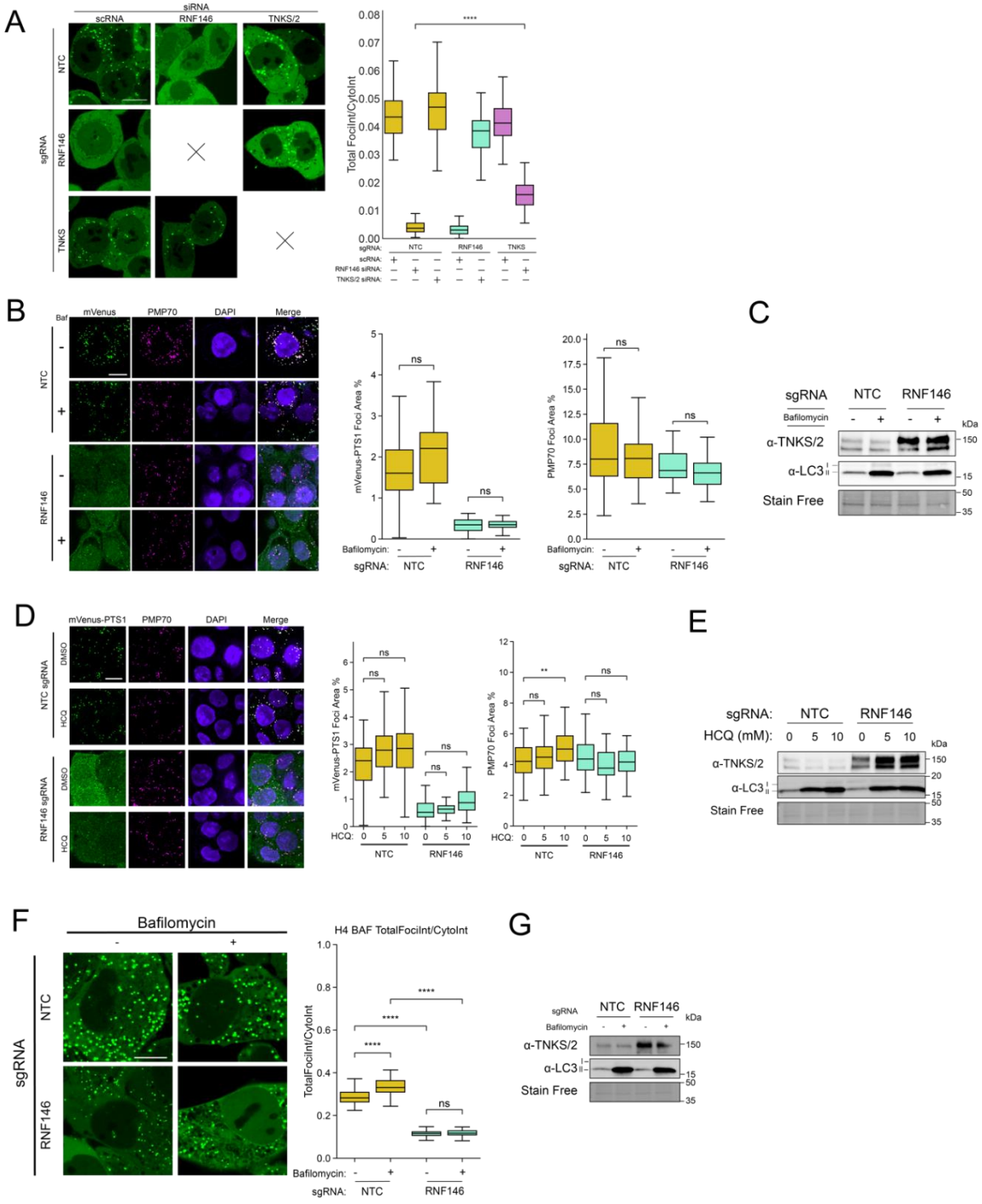

Figure S3. (A) Left Panel: Representative fluorescence microscopy images of NTC, RNF146, TNKS sgRNA expressing HCT116 Pex-ZeoR cells treated with either scrambled siRNA (scRNA), RNF146 siRNA, or TNKS/2 siRNA (10 μM) for 24 hrs. X represents no sample/image. Scale bar: 10 μm. Right Panel: Quantification of mVenus-PTS1 microscopy images in left panel for mVenus foci intensity (peroxisomes) versus total cytosol intensity. Data is representative of m=32 images per condition and n=2 biological replicates. **(B)** Left Panel: Representative immunofluorescence microscopy images of NTC and RNF146 sgRNA expressing HCT116 Pex-ZeoR cells treated with DMSO (mock) or 50 nM Bafilomycin A1 (Baf) for 15 hrs. mVenus-PTS1 in green, DAPI in blue, and PMP70 in cyan. Scale bar: 10 μm. Right panel: Quantification of percentage foci area of mVenus-PTS1 and PMP70 versus cytosolic area for m=21 images and n=2 biological replicates. **(C)** Immunoblot of TNKS and LC3B of cell lysate from conditions in B. **(D)** Left Panel: Representative immunofluorescence microscopy images of NTC and RNF146 sgRNA expressing HCT116 Pex-ZeoR cells treated with DMSO (mock), 5 μM hydroxychloroquine (HCQ), or 10 μM hydroxychloroquine for 24hrs (5 μM HCQ not shown). mVenus-PTS1 in green, PMP70 in magenta, and DAPI in blue. Scale bar: 10μm. Right panels: Quantification of immunofluorescence microscopy images for percentage foci area of mVenus and PMP70, respectively, versus cytosolic area. for m=32 images and n=2 biological replicates. **(E)** Immunoblots of cellular lysate from (D) against TNKS/2 and LC3B. **(F)** Left Panel: Representative fluorescence microscopy images of NTC and RNF146 sgRNA expressing H4 Pex-ZeoR cells treated with DMSO (mock) or 50 nM Bafilomycin A1 for 15 hrs. Scale bar: 10 μm. Right panel: Quantification of mVenus-PTS1 microscopy images in left panel for mVenus foci intensity (peroxisomes) versus total cytosol intensity. Data is representative of m=32 images per condition and n=2 biological replicates. (**G**) Immunoblots of cellular lysate from left panel against TNKS and LC3B. All immunoblots are representative of n=3 independent blots. Asterisks denote p-values *p <0.05, **p <0.01, ***p <0.001, ****p <0.0001, whereas ns denotes not significant, calculated by independent t-test.

F. Loss of RNF146 specifically inhibits import into peroxisomes.

Since the loss of RNF146 did not appear to induce peroxisome-specific autophagy, we evaluated whether the loss of RNF146 could specifically impair peroxisome biogenesis at the stage of protein import into peroxisomes. We performed immunofluorescence microscopy on the HCT116 and H4 CRISPRi Pex-ZeoR cell lines harboring sgRNAs for *NTC*, *RNF146*, *PEX5*, and *PEX19*, where PEX5 and PEX19 are the receptors for PTS1-tagged matrix protein import and peroxisomal membrane protein insertion, respectively **(Fig. 4A, S4A**). We found that knockdown of RNF146 in both HCT116 and H4 cells resembled a PEX5 knockdown, in which a peroxisome membrane protein PMP70 remains present and punctate **(Fig. 4A, 4B, S4A, S4B**), but matrix proteins, both mVenus-PTS1 and catalase, no longer form foci **(Fig. 4A, 4C, Fig. S4A, S4C**) or co-localize with PMP70 **(Fig. S4D**). These observations suggest that loss of RNF146 inhibits import of PEX5 client proteins into the peroxisome.

Efficient peroxisomal matrix protein import relies on PEX5 binding to the PTS1-tagged protein, PEX5 docking to PEX13/PEX14 at the peroxisome, and extraction of ubiquitinated PEX5 from the peroxisome membrane by the PEX1/PEX6/PEX26 motor complex for continued rounds of import. PEX5 is therefore typically distributed between both cytoplasmic and membrane fractions, with an increased proportion at the peroxisome membrane in mutants of the ubiquitination and extraction machinery [Platta et al 2005]. To determine if RNF146 knockdown alters the localization of PEX5, we probed for PEX5, mVenus-SKL, and catalase in soluble and membrane fractions after fractionation. As expected, we observed that PEX5 distributes between both membrane and soluble fractions in wild type cells. Interestingly, a larger proportion of PEX5 was soluble in RNF146

knockdown cells compared to controls cells **(Fig. 4D)**. This suggests that the impairment of import of peroxisomes may be due to reduced recruitment of PEX5 and PTS1-cargo to the peroxisome membrane. Additionally, we observed that the soluble proportion of mVenus-SKL and catalase, both PEX5 client proteins with and without, respectively, a canonical PTS1 tag, increased in RNF146 and PEX5 knockdown cells, confirming that RNF146 knockdown also impedes import of endogenous matrix proteins **(Fig. 4D).**

Figure 4

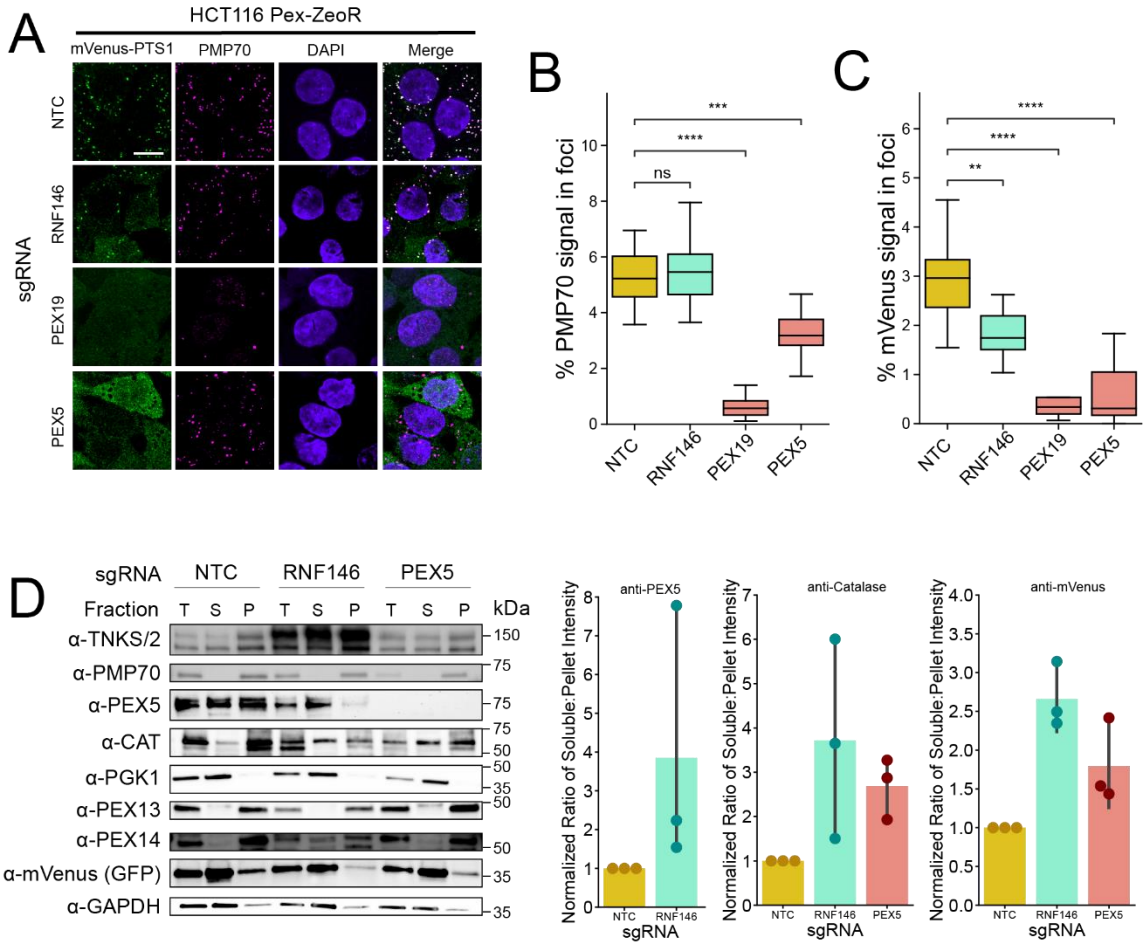

Figure 4. Loss of RNF146 impairs peroxisome protein import. (A) Representative immunofluorescence microscopy images of NTC, RNF146, PEX19, and PEX5 sgRNA expressing HCT116 Pex-ZeoR cells. mVenus-PTS1 in green, DAPI in blue, PMP70 in magenta. **(B, C)** Quantification of immunofluorescence microscopy images for percentage foci area of PMP70 (B) and mVenus-PTS1 (C) versus cytosolic area. m=25 images. n=2 biological replicates. Asterisks denote p-values **p <0.01, ***p <0.001, ****p <0.0001, whereas ns denotes not significant, calculated by independent t-test. **(D)** Immunoblot of HCT116 Pex-ZeoR with sgRNAs targeting NTC, RNF146, and PEX5. Fractions represent total lysate (T), 20,000xg supernatant (S), and 20,000xg pellet (P). Densitometry quantification of blots represents the normalized (to NTC) fold change of the densitometric ratio of soluble vs. pellet fractions (R=S/P) of selected proteins. All blots are representative of n=3 biological replicates.

Supplementary Figure 4

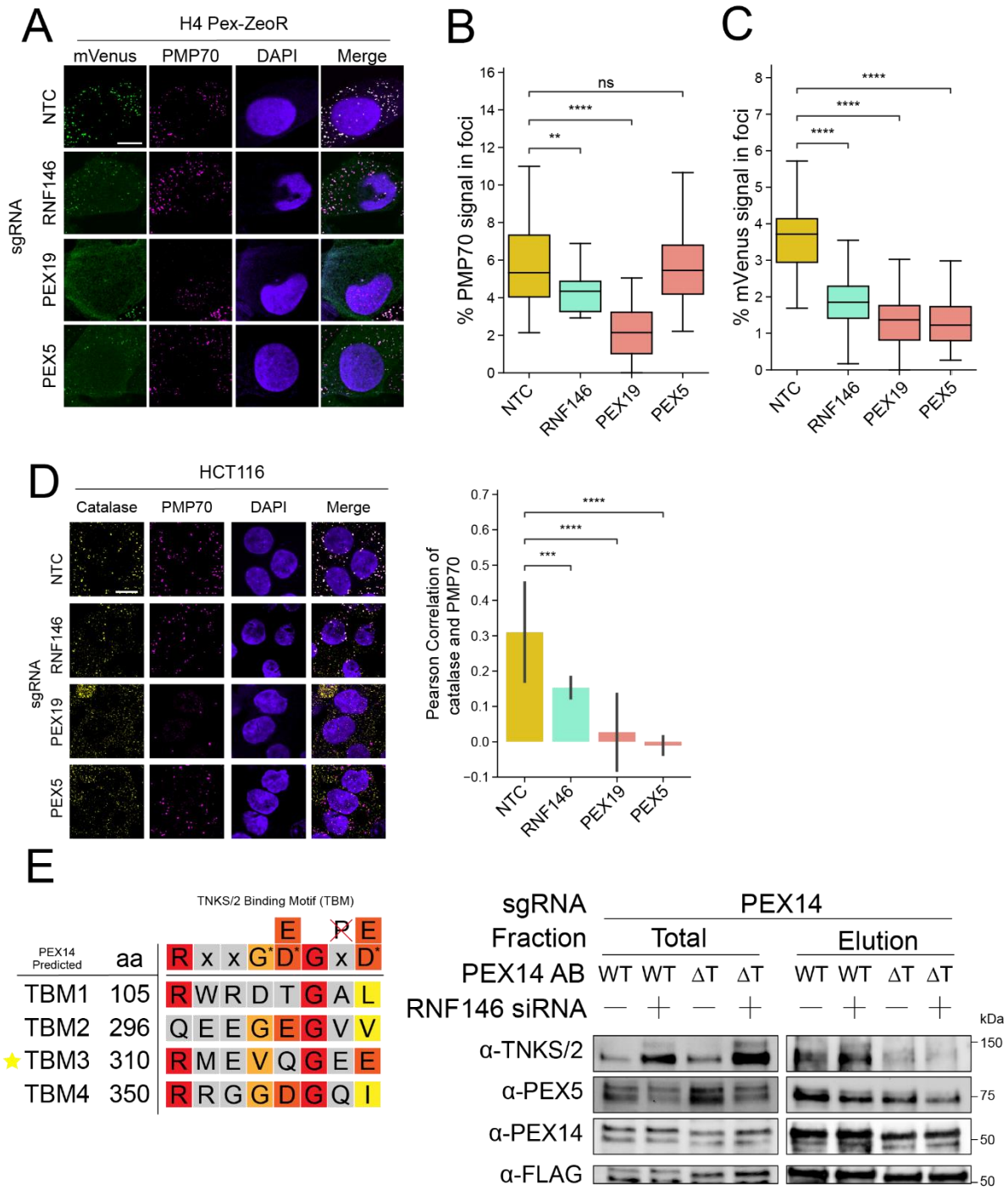

Figure S4. (A) Left Panel: Representative immunofluorescence microscopy images of NTC, RNF146, PEX19, and PEX5 sgRNA expressing H4 Pex-ZeoR cells. mVenus-PTS1 in green, DAPI in blue, PMP70 in magenta. **(B, C)** Quantification of immunofluorescence microscopy images for percentage foci area of PMP70 **(B)** and mVenus **(C)**, respectively, versus cytosolic area. n=25 images. **(D)** Left Panel: Representative immunofluorescence microscopy images NTC, RNF146, PEX19, and PEX5 sgRNA expressing cells. Catalase in yellow, DAPI in blue, PMP70 in magenta. m=25 images. n=2 biological replicates. Right panel: Quantification of Pearson's correlation coefficient of catalase and PMP70 colocalization of microscopy images. **(E)** Left Panel: Schematic showing the predicted TBMs of PEX14 with amino acid positions, compared to the predicted consensus TBMs of Guettler et al. 2016 and Pollock et al. 2017. Red=essential, dark orange=common/variable, light orange=variable, yellow=uncommon/accepted, grey=no pattern, G*= glycine or small non hydrophobic, D*= D/E with some variability, defaced P= no proline. Star = Chosen ΔTBM. Right Panel: Immunoblots of anti-FLAG immunoprecipitation total and elution fractions from HCT116 Pex-ZeoR cells expressing PEX14 sgRNAs with constitutive re-expression of either FLAG-PEX14 (WT) or FLAG-PEX14-ΔTBM3 (ΔT), treated with either NTC or RNF146 siRNA (10 nM) for 24hrs, detecting TNKS/2, PEX5, and PEX14. Blots are representative of n=3 biological replicates.

G. PARP activity of TNKS/2 impedes import into peroxisomes.

TNKS/2 contains N-terminal ankyrin repeats that bind substrates with a TBM, a SAM domain that mediates oligomerization, and a C-terminal poly(ADP-ribose) polymerase domain [Guettler et al 2011]. There are predicted, conserved TBMs in PEX14, PEX5, PEX19, and PEX11G [Guettler et al 2011]. Specifically, PEX14 was predicted to have at least 4 purported TBMs (**Fig. S4E**). We found that TNKS/2 co-immunoprecipitated both FLAG-PEX14 and PEX5 upon RNF146 knockdown **(Fig. 5A)**. Additionally, when the reciprocal experiment was performed, full length FLAG-PEX14 co-immunoprecipitated TNKS/2 and PEX5 in NTC and RNF146 knockdown cells. Notably, when the TBM3 of PEX14 was mutated, FLAG-PEX14-ΔTBM3 cells had reduced affinity for TNKS/2 interaction **(Fig. S4E)**. These results suggest TNKS/2 associates with the peroxisome membrane and peroxisome import machinery, such as PEX14, upon RNF146 knockdown. To test if RNF146's effect on peroxisome import depended on the PARP activity of TNKS/2, we tested if the TNKS/2 inhibitors G007LK and XAV939 restored peroxisome foci in RNF146 knockdown cells **(Fig. 5B, 5C)**. We found that TNKS/2 inhibitors partially restored import of mVenus-PTS1 into foci in RNF146 knockdown cells as judged by the ratio of foci to cytosolic intensity of mVenus-PTS1, but did not fully recover peroxisome number **(Fig. 5C)**. To determine if TNKS/2 PARsylated proteins at the peroxisome membrane, we immunoprecipitated PEX14-FLAG. We found that proteins in the PEX14-FLAG elution, which included PEX14-FLAG, PEX13, PEX5, and TNKS, were PARsylated (**Fig. 5D)**. While it is unclear exactly which proteins are PARsylated, PARsylation was sensitive to TNKS/2 inhibitor XAV939 and amplified by RNF146 knockdown (**Fig. 5D)**. In addition, we found that suppression of RNF146 and the concomitant increase of TNKS/2

resulted in lowered steady state levels of PEX14 and PEX13, but not peroxisome membrane protein PMP70, and that this effect was abrogated when TNKS/2 was inhibited by XAV939 (**Fig. 5E**). All together, these observations suggest that TNKS/2's PARsylation activity is important for RNF146's effect on peroxisomes. We therefore propose a model in which high levels of active TNKS/2, induced by loss of RNF146, binds PEX14 and PARsylates proteins at the peroxisome membrane, which inhibits PEX5-mediated protein import into peroxisomes (**Fig. 5F)**.

Figure 5

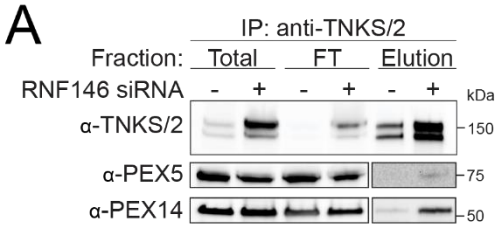
A
IP: anti-TNKS/2
Fraction: Total FT Elution
RNF146 siRNA - + - + - +
kDa
α-TNKS/2
150
α-PEX5
75
α-PEX14
50

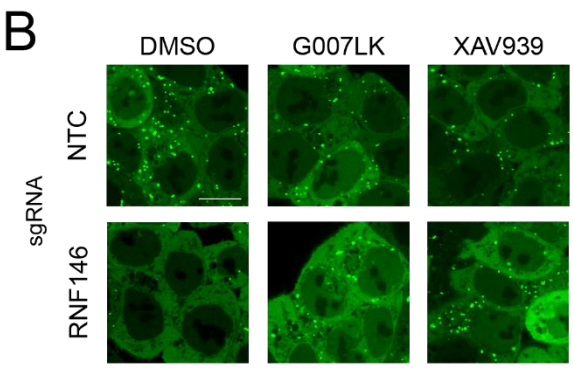
B
DMSO
G007LK
XAV939
sgRNA
NTC
RNF146

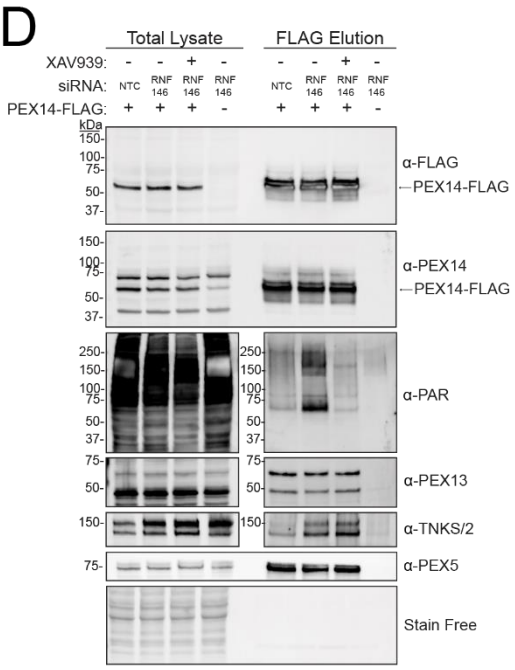
D
Total Lysate
FLAG Elution
XAV939:
siRNA: NTC RNF146 RNF146 RNF146
PEX14-FLAG:
kDa
α-FLAG
PEX14-FLAG
α-PEX14
PEX14-FLAG
α-PAR
α-PEX13
α-TNKS/2
α-PEX5
Stain Free

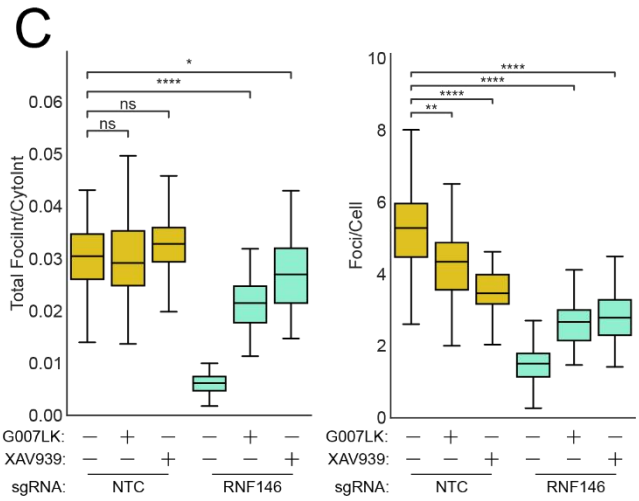
C
Total FociInt/CytoInt
Foci/Cell
G007LK:
XAV939:
sgRNA:
NTC
RNF146
ns
*
**
****

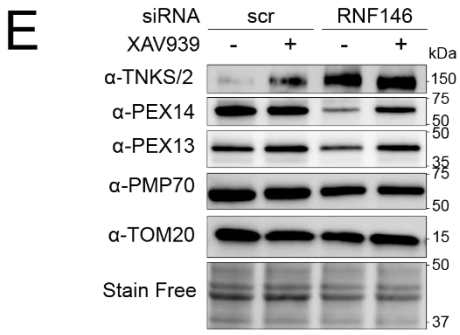
E
siRNA scr RNF146
XAV939 - + - +
kDa
α-TNKS/2
α-PEX14
α-PEX13
α-PMP70
α-TOM20
Stain Free

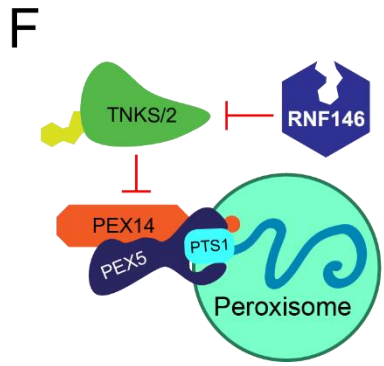
F
TNKS/2
RNF146
PEX14
PEX5
PTS1
Peroxisome

Figure 5. TNKS/2 PARP activity impairs peroxisome protein import. (A) Immunoblots of anti-TNKS/2 immunoprecipitation fractions from HCT116 Pex-ZeoR cells expressing PEX14 sgRNAs with constitutive re-expression for FLAG-PEX14 treated with either NTC or RNF146 siRNA (10 nM) for 24hrs, detecting TNKS/2, PEX5, and PEX14. **(B)** Representative live-cell fluorescence microscopy images of NTC and RNF146 sgRNA expressing HCT116 Pex-ZeoR cells treated with DMSO (mock), 500 nM G007LK, or 10 μM XAV939 for 24 hrs. mVenus-PTS1 in green. Scale bar: 10 μm. **(C)** Quantification of fluorescence microscopy images for the ratio of mVenus-PTS1 foci intensity to mVenus-PTS1 cytosolic intensity (left) and the number of foci per cell (right). m=32 images and n=2 biological replicates. Asterisks denote p-values *p <0.05, **p <0.01, ***p <0.001, ****p <0.0001, whereas ns denotes not significant, calculated by independent t-test. (**D**) Immunoblots of anti-FLAG immunoprecipitation Total Lysate (input) and Elution fractions from HCT116 Pex-ZeoR cells expressing NTC sgRNA (lane 4/8) or PEX14 sgRNAs with constitutive re-expression for PEX14-FLAG (lane 1/2/3/5/6/7) treated with either NTC or RNF146 siRNA (10 nM) for 24hrs, with or without XAV939 (1 μM) for 24hrs., and with carfilzomib (10 μM) for 4hrs, detecting FLAG, Poly-(ADP)-ribose (PAR),TNKS/2, PEX5, PEX13, and PEX14. Representative of n=2 biological replicates. **(E)** Immunoblots of lysates from HCT116 CRISPRi cells harboring NTC guides treated with either NTC or RNF146 siRNA (10 nM) for 48 hrs, and with or without XAV939 (1 μM) for 24hrs. Representative of n=4 biological replicates. (**F**) Proposed model: loss of RNF146 increases active TNKS/2, which binds PEX14 and PARsylates proteins at the peroxisome membrane impairing peroxisome import.

H. PEX proteins alter RNF146/TNKS/2 activity towards other substrates.

This model suggests that TNKS/2 binds peroxisome membrane protein PEX14 and can localize to the peroxisome. Other better-known substrates of TNKS/2, such as BLZF1, which localizes to the Golgi [Yue et al 2021], and AXIN1, which localizes to centrosomes [Lach et al 2022], have defined locations elsewhere in the cell. We thus wondered if peroxisomal recruitment of TNKS/2 could regulate access to other substrates. To test if the presence of peroxisome membranes and membrane proteins alters TNKS/2 substrate selection, we evaluated the stability of the TNKS/2/RNF146 substrates AXIN1, CASC3, and BLZF1 in cells with knockdown of the peroxisomal membrane protein *PEX14*, the peroxisomal membrane protein chaperone *PEX19*, or a non-targeting control (NTC). We found that AXIN1 and CASC3 levels were significantly depleted in *PEX19* knockdown HCT116 cells, and BLZF1 levels were depleted in both *PEX19* and *PEX14* knockdown HCT116 cells (**Fig. 6A**). Furthermore, *PEX14* and *PEX19* knockdowns also depleted AXIN1 levels in HEK293T, iPSC AICS-0090-391, and H4 CRISPRi cells (**Fig. 6B, 6C, Fig. S5A**), illustrating that this phenomenon is not specific to HCT116 cells. To confirm that the effect of *PEX19* knockdown arises from loss of PEX19, we re-expressed PEX19 using a lentiviral vector to complement the knockdown of endogenous *PEX19*, and observed a rescue of AXIN1 stability (**Fig. 6D**). Additionally, suppression of either *RNF146* or *TNKS/2* mRNA transcripts via siRNA, as well as XAV939-mediated catalytic inhibition of TNKS/2, restored AXIN1 stability in *PEX19* knockdown cells, demonstrating that loss of PEX19 activates RNF146/TNKS/2-mediated destabilization of AXIN1 (**Fig. 6D**). These

observations suggest that functional peroxisomes repress TNKS/2 activity towards some substrates, including AXIN1, BLZF1, and CASC3.

I. Increased Wnt/beta-catenin signaling in PEX knockdown cells.

AXIN1 is the limiting component for the formation of the beta-catenin destruction complex which induces the phosphorylation and subsequent degradation of the beta-catenin transcription factor. In canonical Wnt signaling, Wnt ligand binding to the Frizzled receptor dissociates the beta-catenin destruction complex, allowing beta-catenin to accumulate, enter the nucleus, and induce transcription of Wnt-responsive genes. The stabilization of AXIN1, such as by TNKS/2 inhibitors, inhibits Wnt signaling by increasing levels of the destruction complex [Huang et al 2009]. Since AXIN1 was severely destabilized in *PEX19* knockdown HCT116 cells and partially destabilized in *PEX14* and *PEX19* knockdown HEK293T, H4, and iPSC AICS-0090-391 cells, we tested if the knockdown of *PEX* genes can therefore influence the Wnt signaling pathway using the TOPFlash reporter for beta-catenin transcriptional activity. We found that HCT116 cells had a greater transcriptional response to Wnt ligand in *PEX14* and *PEX19* knockdown cells (**Fig. 6E**), as well as increased basal activity. Since HCT116 cells are derived from a colorectal carcinoma heterozygous for a dominant mutation in beta-catenin that causes constitutively active beta-catenin-TCF regulated transcription [Morin et al 1997], we also tested the effect of the PEX knockdowns on the TOPFlash reporter in HEK293T cells. Both *PEX14* and *PEX19* knockdown HEK293Ts exhibited a partial loss of AXIN1 levels (**Fig. 6B**), and consistently, also exhibited a greater response to Wnt ligand, though basal levels were not perturbed (**Fig. 6F**). Our observations show that knockdown of *PEX14* and *PEX19* increases Wnt signaling

consistent with the decreased levels of the core subunit of the beta-catenin destruction complex, AXIN1.

Figure 6

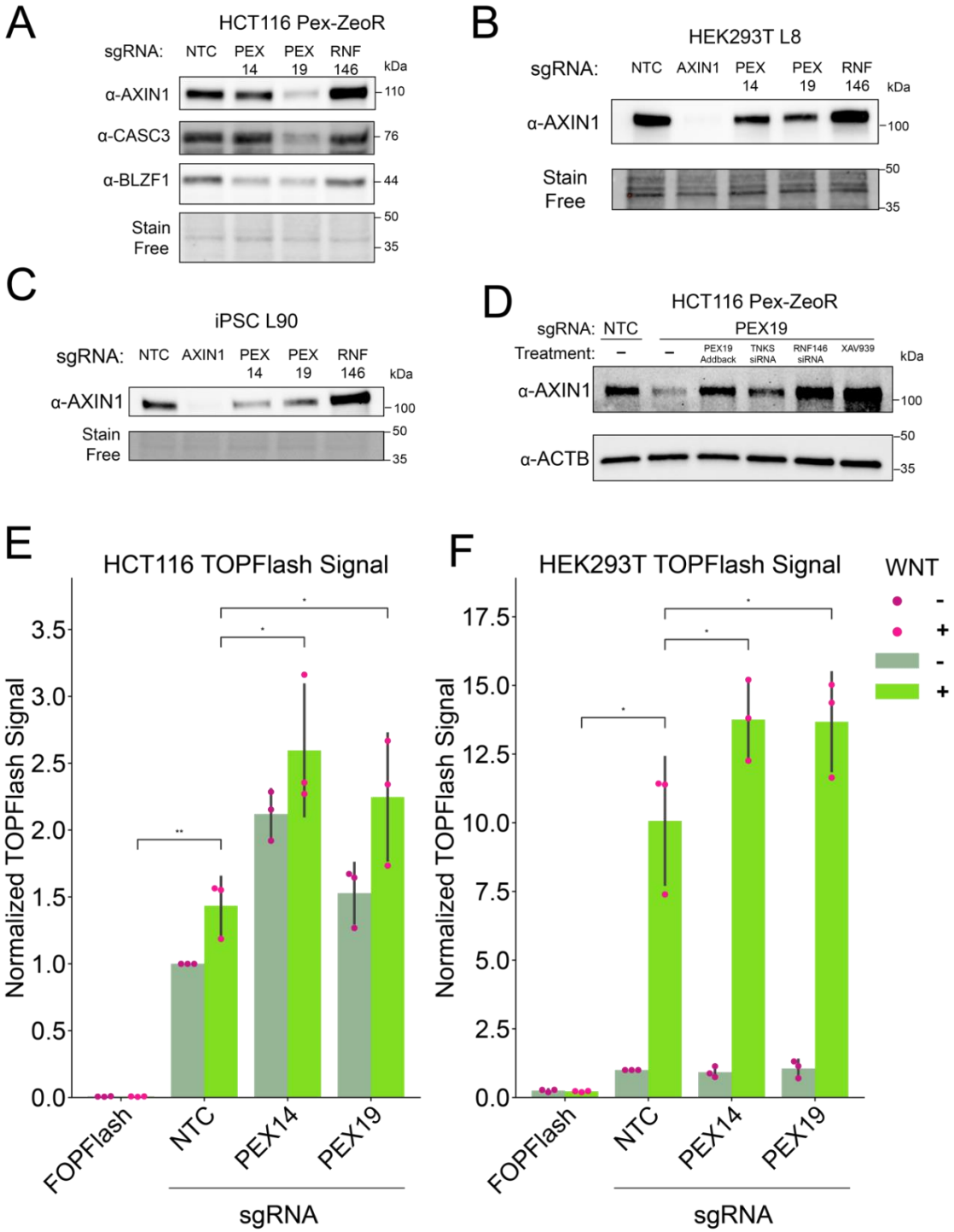
A
HCT116 Pex-ZeoR
sgRNA: NTC PEX 14 PEX 19 RNF 146
kDa
α-AXIN1
α-CASC3
α-BLZF1
Stain Free
110
76
44
50
35
B
HEK293T L8
sgRNA: NTC AXIN1 PEX 14 PEX 19 RNF 146
kDa
α-AXIN1
Stain Free
100
50
35
C
iPSC L90
sgRNA: NTC AXIN1 PEX 14 PEX 19 RNF 146
kDa
α-AXIN1
Stain Free
100
50
35
D
HCT116 Pex-ZeoR
sgRNA: NTC
PEX19
Treatment: – – PEX19 Addback TNKS siRNA RNF146 siRNA XAV939
kDa
α-AXIN1
α-ACTB
100
50
35
E
HCT116 TOPFlash Signal
Normalized TOPFlash Signal
FOPFlash
NTC
PEX14
PEX19
sgRNA
F
HEK293T TOPFlash Signal
WNT
Normalized TOPFlash Signal
FOPFlash
NTC
PEX14
PEX19
sgRNA

Figure 6. Peroxisome abundance influences RNF146/TNKS substrate selection. (A-C) Immunoblots measuring the abundance of AXIN1, CASC3, and BLZF in **(A)** HCT116 (n=3), **(B)** HEK293 (n=3), and **(C)** iPSC AICS-0090-391 (n=3) CRISPRi cells with indicated sgRNAs. **(D)** Western blot measuring abundance of AXIN1 and ACTB (loading control) in HCT116 cells with indicated sgRNAs, PEX19 knockdown cells are paired with treatments for PEX19 reexpression, TNKS siRNA (10 nM), RNF146 siRNA 10 nM), or XAV939 (10 μM). Blots shown are representative of n=1 blots. **(E-F)** TOPFlash Dual Luciferase assays measuring the induction of Wnt signaling to downstream beta-catenin transcription in PEX knockdown HCT116 cells (E) and HEK293T (F) harboring the indicated sgRNAs and treated with or without 315ng/mL Wnt3a for 24 hrs (data shown is 48 hours post-transfection with TOPFlash constructs). Luciferase activity is measured versus a Renilla transfection control and data is normalized to untreated NTC samples. FOPFlash negative control performed in NTC sgRNA cells. Data is representative of n=3 biological samples. Asterisks denote p-values *p <0.05, **p <0.01, calculated by paired t-test.

Supplementary Figure 5

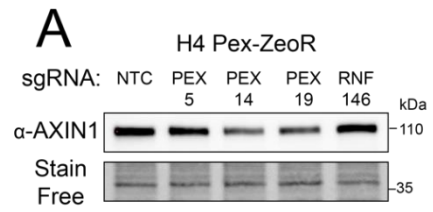

Figure S5. (A) Immunoblot measuring the abundance of AXIN1 in H4 CRISPRi cells expressing sgRNA for NTC, PEX5, PEX14, PEX19, and RNF146.

III. The influence of PEX14/PEX19 stability on Wnt induced NPC/NCSC differentiation.

We found that loss of PEX14 and PEX19 in HCT116 and HEK293T cells destabilizes AXIN1 which resulted in a significant increase in the amount of Wnt-signaling/beta-catenin activated transcription that occurs (**Fig. 6A-F**). Wnt-signaling is an important multimodal family of proteins that determines cell fate in developmental biology as well as regulatory homeostasis in adult organisms. Its dysregulation leads to various neurodegenerative diseases, such as Parkinson's and ALS, and cancers, such as colorectal cancer (Liu et al. 2022). The canonical Wnt pathway involves beta-catenin as a target downstream transcription factor for modulation. This proceeds when various Wnt proteins interact with cell surface proteins LRP5/6 and Frizzled which then recruits the "destruction complex", a conglomerate of the proteins: AXIN1/2, casein kinase 1 (CK1), glycogen synthase kinase 3 protein (GSK3B), and adenomatous polyposis coli (APC), inhibiting the destruction complex's ability to degrade beta-catenin, thus resulting in beta-catenin being shuttled to the nucleus and activating downstream TCF/LEF promoter motifs (Liu et al. 2022). Thus, a natural extension of the results of the dual luciferase topflash assays was to determine where PEX14/PEX19 knockdown induced modulation of AXIN1 and thus Wnt-signaling would be relevant in a developmental cell biology and organismal context. Phylogenetic comparison of the C-terminal region of PEX14 shows that the TBM region is conserved in mammals and as far back as turtles (this would date the motif acquisition as far back as the late Jurassic ~160 million years ago (Edwin et al. 2015)), which may suggest an important developmental role for the PEX14-TNKS interregulatory interaction. Humans and mice with lesions in peroxisome import genes including PEX1, PEX2, PEX5, PEX10, PEX13, PEX14, and

PEX11β have neurological defects in cortical neuron migration and cerebellar malformation (Evrard et al 1978, Volpe and Adams 1972; Kocherlakota et al 2023). Therefore, such a role may be related to the efficiency, or rather deficiency, of neural development in organisms with PEX14 mutations. For example, a study by Abe et al. found that mutating PEX14, by deleting the C-terminal TBM inclusive region, caused disorganization of cortical laminar structures, malformed the cerebellum, and led to immediate postnatal death in mice homozygous for the mutation, while peroxisome function was only partially impaired (Abe et al. 2018). This study may parallel the function of Wnt-signaling in neuronal cell differentiation. Cortical development requires a gradient of Wnt signaling and disruption of this gradient through ectopic expression of Wnt causes extreme morphological changes in the cortex as well as downregulation of the neurogenic marker Pax6 (Machon et al 2007). Previous research has established an essential role of Wnt-signaling in early stem cell ectoderm differentiation, specifically the cell fate decision between neural progenitor cells (NPCs) and neural crest stem cells (NCSCs) (Menendez et al. 2011). Menendez et al. discovered that Wnt-signaling strongly influenced this decision, demonstrating that increasing beta-catenin abundance through various means, such as GSK3B inhibition via BIO or Wnt3a incubation, biased cells to switch from NPCs to NCSCs in a dose dependent manner. AXIN1 is a limiting component of the destruction complex, it serves as a scaffolding complex that unites APC, CK1, and GSK3B with the purpose of degrading beta-catenin when Wnt-signaling is inactivated. Thus, we hypothesized that the interregulatory role that PEX14 had on AXIN1 stability, a component of the beta-catenin destruction complex that includes GSK3B, would extend to the developmental stem cell decision between NPCs and NCSCs as well. We theorized that suppression of PEX14 or PEX19

would destabilize the destruction complex by proteasomal degradation of AXIN1 via the increased the target specificity of RNF146/TNKS, resulting in a surfeit of beta-catenin and downstream transcriptional activation of genes biasing cells to NCSCs.

To test whether or not PEX14 expression was connected to stem cell fate via a Wnt signaling bridge we employed a differentiation assay utilizing dual SMAD inhibition, with GSK inhibition as a NCSC positive control. Dual SMAD inhibition is a widely accepted drug regimen for reliable induction of iPSCs into NPC cells, with some small population (<5%) spontaneously differentiating into NCSCs (Chambers et al. 2009). It involves the treatment of iPSCs with the small molecule SB431542, an activin/BMP/TGF-β pathway inhibitor, and the peptide Noggin, a cytokine antagonist of BMP and TGF-β ligands (Chambers et al. 2009, Chiba et al. 2008). Earlier attempts by Chambers et al. to enrich for the minority runoff population of NCSCs produced by dual SMAD inhibition were first accomplished by laborious sorting for p75+ Hnk1+ PAX6- NCSCs (Chambers et al. 2012). Contemporaneously, or at least closely so, Menendez et al. found that Wnt-signaling activation accomplished the same goal, by addition of GSK3B inhibitor BIO, GSK inhibitor CHIR99021, or cytokine Wnt3a, redirecting differentiating neural progenitors into NCSCs (Menendez et al. 2011, Menendez et al. 2013). We acquired a CRISPRi iPSC cell line from the Allen Institute (AICS-0090-391), and stably expressed the following guides: [NTC, PEX14, PEX19, AXIN1, RNF146], verifying KD (**Fig. 7B**). Cells infected with the aforementioned guides did not spontaneously differentiate when cultured in mTeSR Plus media, retaining strong expression of pluripotency markers Oct4+, Sox2++, PAX6-, and Hnk1- (**Fig. 7C**). In our initial pilot experiment, we confirmed that base CRISPRi iPSCs differentiated into majority NPCs (PAX6+ SOX2+) with dual SMAD inhibition and

differentiated into NCSCs (Hnk1+ PAX6-) upon addition of Wnt activation using BIO, thus recapitulating the research findings of Chambers et al. and Menendez et al. (**Fig. 7A, 7C**). Primary experiment differentiation revealed that, consistent with BIO induced inhibition, AXIN1 KD iPSCs preferentially differentiated into NCSCs, when compared to NTC iPSCs. Furthermore, PEX14 KD cells had increased differentiation preference for NCSCs when compared to NTC iPSCs, but to a lesser extent than AXIN1 KD cells, reflecting the partial destabilization effect PEX14 KD on AXIN1 (**Fig. 7C-D**).

Despite these interesting results, which supported our hypothesis, it is unavoidable that a major caveat must be addressed. The reason for the use of the word "Primary" in the penultimate sentence of the previous paragraph was because, although the differentiation was meant to be run in triplicate, operator error resulted in some replicates being lost to a near mass extinction event. Fortunately, about 6000 cells per sample survived and went on to differentiate and repopulate, albeit with great difficulty, slowly, and for some replicates not at all, over a period of 45 days. This summoned a horrific specter of doubt over the results of the experiment and necessitated repeat experiments. Three more repeat trials of the differentiation experiments were repeated with none being able to replicate the original results (**Fig. 7E**). These replicate experiments, however, did yield critical data and elucidated drawbacks associated with the experiment design, and were not a complete waste of resources and time, hopefully. Perhaps the most glaring major problem was with the iPSC CRISPRi system, the KDs were strong and robust only while the cells were not differentiating, it was observed that dCas9 expression decreased when the cells differentiated, somewhere around 25% for NTC cells by day 15 (by the operator, another student, and Beth Pruitt's lab) (**Fig. 7F**). This could likely lead to decreased and inconsistent

suppression of the target gene as cells differentiated and thus an incomplete CRISPRi effect or no effect at all. This was apparent when not even AXIN1 KD cells would not strongly affect differentiation whereas small molecule treatment with BIO still induced differentiation in repeat trials.

Another explanation for the primary run being successful is that the cells were culled down to a number low enough where single cells were not influenced by mosaicism, and, for some reason, did not have this dCas9 attenuation phenotype. We found that in trials 3 and 4 that the initial seeding density of stem cells upon differentiation start time had a profound impact on the final outcome of stem cell marker expression just for the CRISPRi KD cells, but not the BIO treated cells, suggesting that some sort of intercell communication negated the effects of dCas9 possibly due to mosaicism in the KD efficiency of cell neighbors, something avoided completely when the positive control NCSC condition are absolutely besotted with 2uM BIO treatment (**Fig. 7G**).

Inability to repeat the results of the primary differentiation experiment does not invalidate the original hypothesis. As was shown, even a dilettante in stem cell biology was able to replicate the findings of previous studies while partially expanding upon a novel theory. As an improvement to this experiment, we have created inducible DSB efficient CRISPR-Cas9 iPSCs capable of gene knockout (KO) upon treatment with doxycycline, harboring guides for [NTC, AXIN1, PEX14, PEX19, RNF146]. This will eliminate the consequences that might result from the silencing of dCas9 and/or any selected sgRNA during the differentiation process. An expedient step to take would be to induce Cas9 nuclease activity during iPSC maintenance, verifying strong KO by T7 and WB, and then executing the differentiation process while taking down samples from splits at various

timepoint until t=15+. KO consistency could be ascertained at all timepoints by a T7 digest assay or by WB of the target protein to guarantee KO does not somehow diminish. Differentiation completion would be checked against NTC iPSC cells that were treated with only Dual SMAD (NPC control), and Dual SMAD + BIO (NCSC control), as these would serve as the polar extremes for differentiation efficiency, with AXIN1, PEX14, and PEX19 falling somewhere in between. Ideally, because the KO is a one-shot sort of event, there should not be any strong effect of seeding density on the cells at early differentiation times, assuming knockout is complete. That being said, "only the paranoid survive", and it would behoove future researchers to run parallel seeding densities to gather data on multiple conditions and outcomes.

Another originally considered iPSC differentiation pathway that depends on Wnt-signaling is the differentiation of iPSCs to mesodermal cardiac progenitor cells (CPC) and cardiomyocytes. Generally, this differentiation protocol relies on specific temporal treatment of iPSCs with a GSK3B inhibitor, CHIR99021 (similar to BIO), early on for 3 days, a switch to Wnt-C59 (a Wnt-3a inhibitor) for 2 days, and then removal of all Wnt drugs and changes in glucose availability for the remainder of differentiation (Lian et al. 2012). Because of this tricky specific temporal confinement of Wnt activation and then sharp complete deactivation, the current cell lines that we have would likely cause large disruptions in cardiomyocyte differentiation because of either complete KO early on, or continual suppression via CRISPRi. Despite this, it could still be insightful to see if PEX14/PEX19 KO would compromise cardiomyocyte differentiation similar to how an AXIN1 KO would interfere with the rest phase of differentiation, keeping beta-catenin induced transcription running and possibly preventing cardiomyocyte differentiation at all.

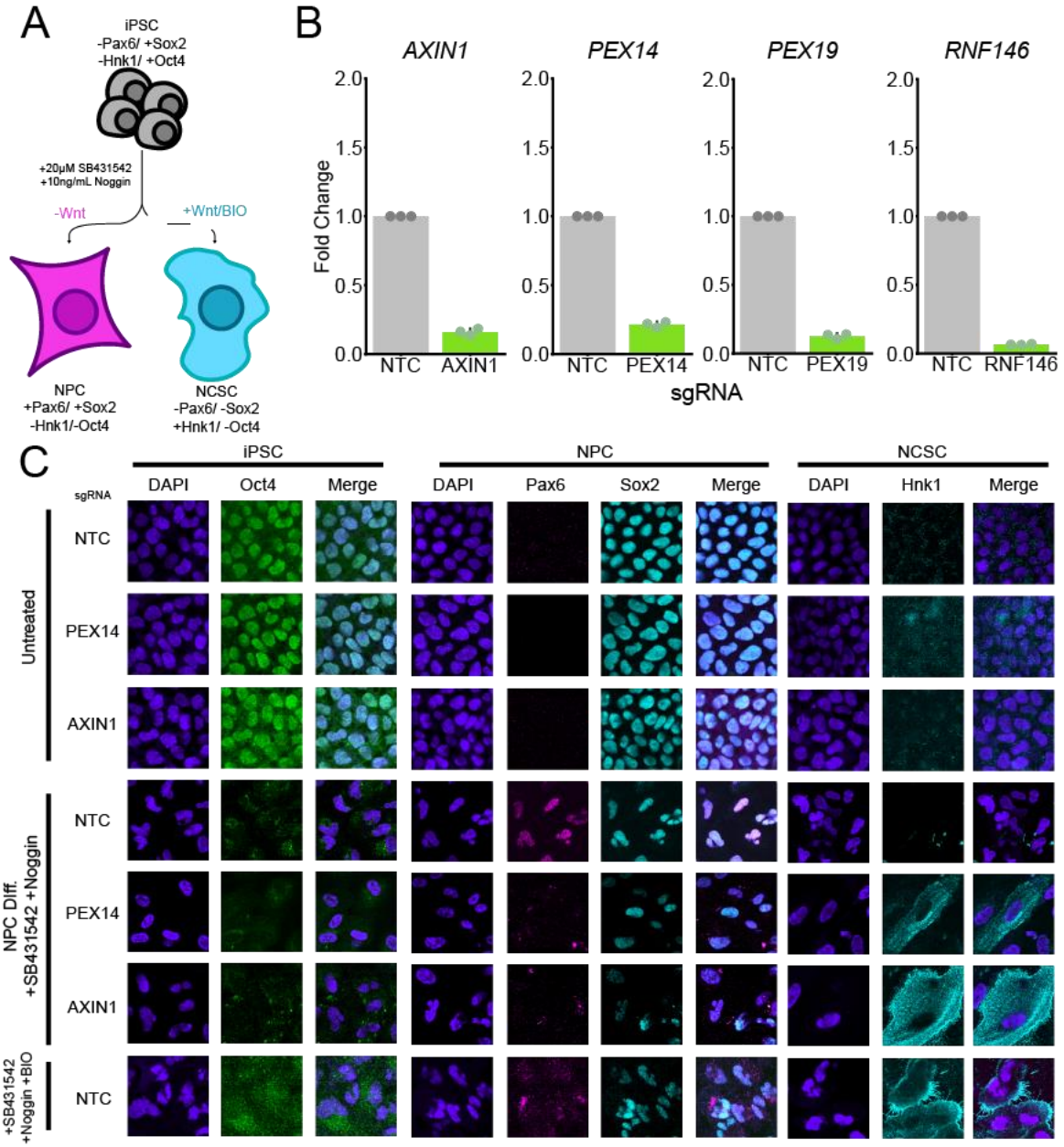

Figure 7. PEX14/PEX19 expression and the iPSC developmental fate between NPCs/NCSCs.
(A) Model of dual-Smad inhibition (SB43142 and Noggin) and Wnt-dependent differentiation of iPS cells into NPC or NCSC cells with associated markers. **(B)** RT-qPCR of iPSC CRISPRi cells with specified sgRNAs quantifying respective fold change of transcripts for AXIN1, PEX14, PEX19, and RNF146 normalized to NTC sgRNA expressing cells. n=3. **(C)** Oct4, Pax6, Sox2, and Hnk1 immunofluorescent staining of undifferentiated and differentiated iPS cells with NTC, PEX14, and AXIN1 targeting guides. BIO is a GSK3B inhibitor that activates Wnt signaling.

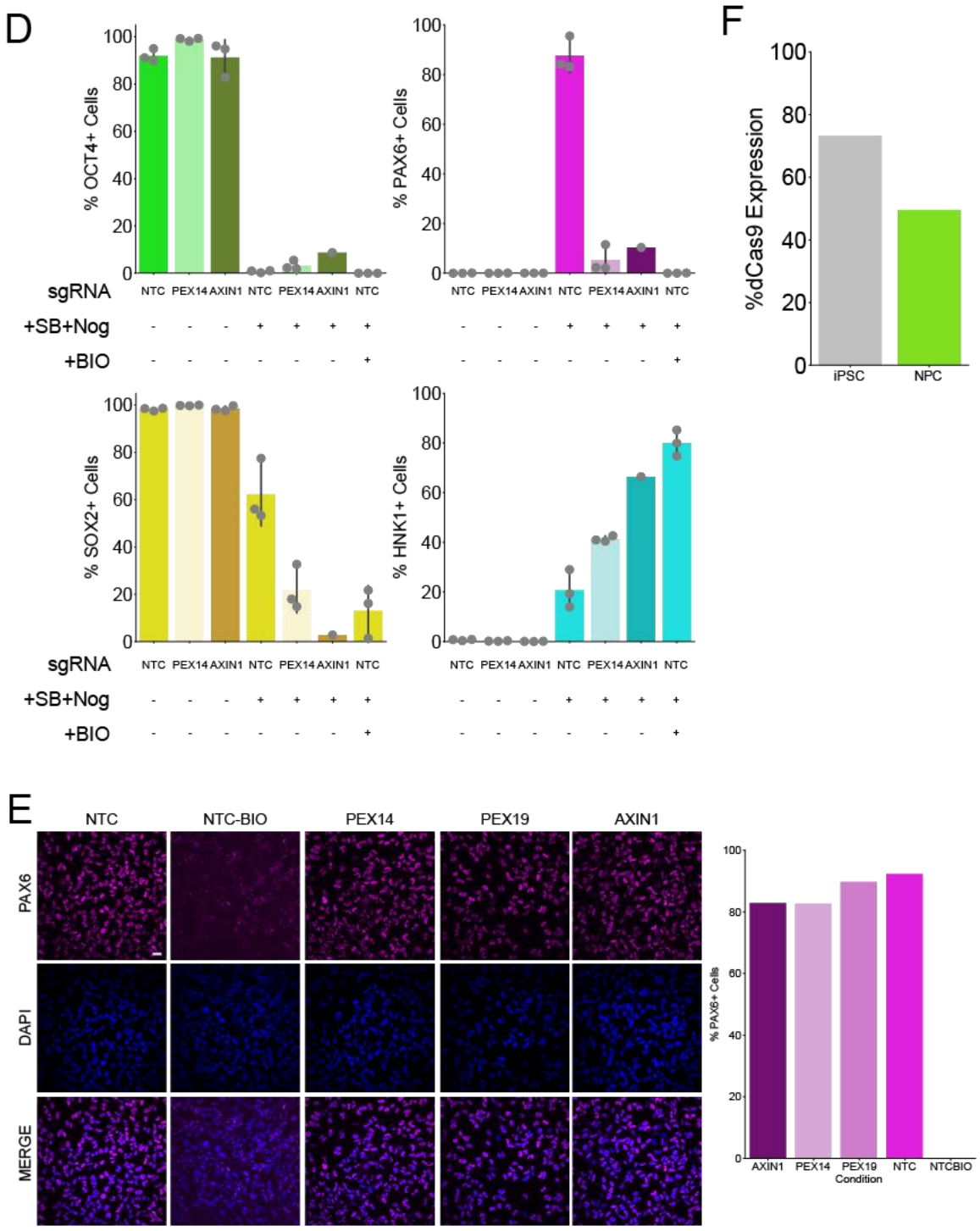

Figure 7. (D) Quantification of the percent of cells shown in (C) stained with antibodies specified. m=1-3 samples n=24 images **(E)** Left panels: Representative immunofluorescence microscopy images of differentiated (t=28) iPSC CRISPRi expressing specified sgRNAs with or without BIO treatment for NTC (horizontal axis) staining for Pax6 (magenta) and DAPI (blue). Scale bar = 10um. Right panel: Quantification of PAX6+ cells in left panels. **(F)** Quantification of flow cytometry data of % BFP+ (dCas9) undifferentiated iPSCs and differentiated NPCs expressing guides for NTC at t=14. n=1

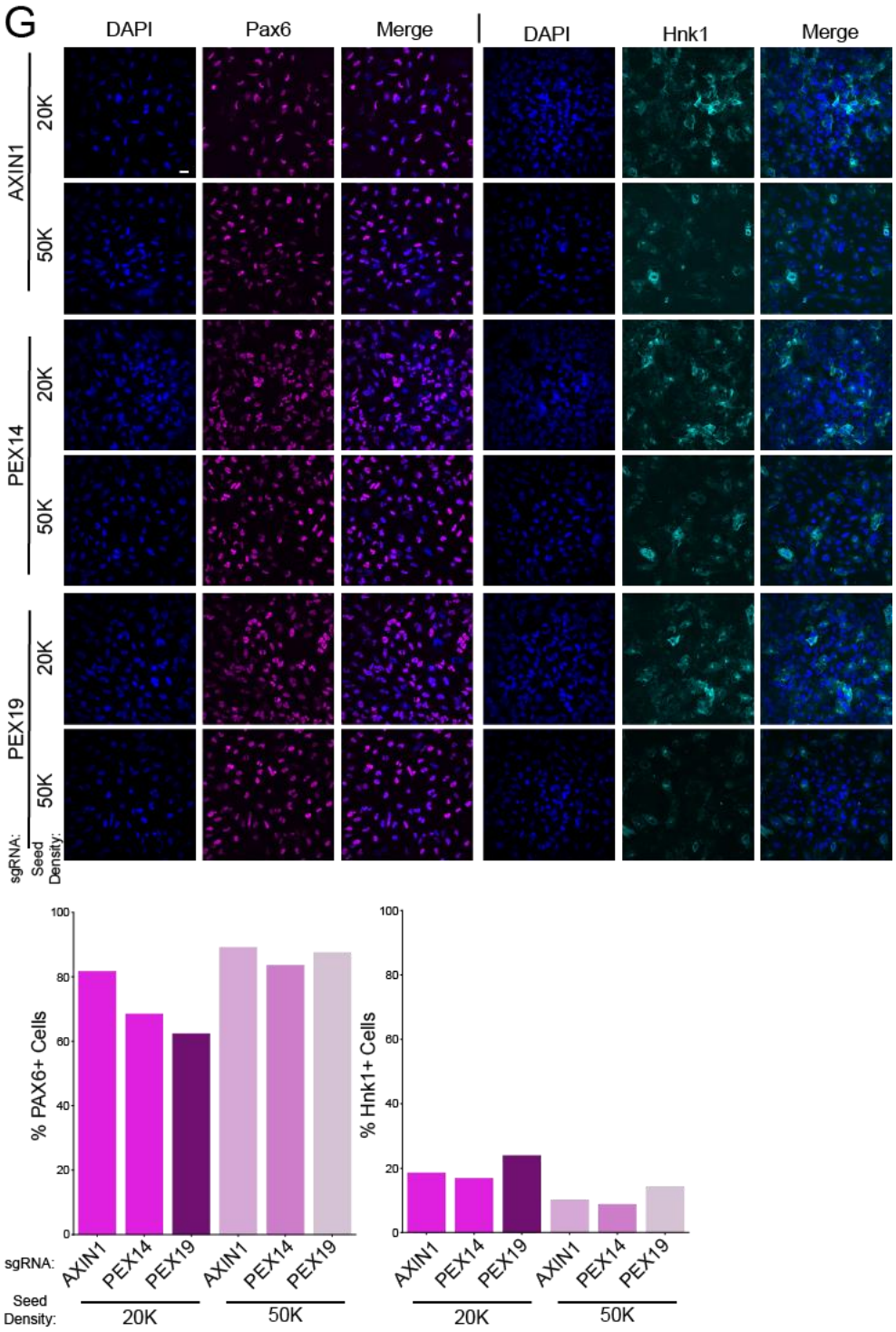

Figure 7. (G) Upper panels: Representative immunofluorescence microscopy images of differentiated (t=14) iPSC CRISPRi expressing specified sgRNAs at two starting densities, 20,000 (20K) and 50,000 (50K) (vertical axis) staining for Pax6 (magenta) or Hnk1 (teal), and DAPI (blue). Scale bar = 10um. Bottom panel: Quantification of PAX6+ and HNK1+ cells in upper panels.

IV. Peroxisome homeostasis candidate - SOCS3.

Of the results of the secondary microscopy screen, the genetic knockdown of Suppressor of Cytokine Signaling 3 (SOCS3) produced a striking phenotype that caused a near total loss of peroxisomal foci (represented by mVenus-SKL fluorescence signal) in the microscopy cell line HCT116 2055 D01 (**Fig. 8A-B**). The role of SOCS3 is that of a STAT inhibitor, induced by the cytokines IL6, IL10, and IFN-gamma, where it binds to JAK2 and inhibits its activity (Carow et al. 2014). However, of the two guides tested, only SOCS3 G1 (guide sequence: GCTGCGTGCGGGGCCGAAG) produced an effect where peroxisome import was completely lost, whereas SOCS3 G2 (guide sequence: GGGGCCGAAGCGGCAGCAG) did not exhibit the same effect. Because of this inconsistency between the two guides, there was a shadow of doubt cast upon the verisimilitude of SOCS3's effect on peroxisomes. Two additional guides were produced, SOCS3 G3 (guide sequence: GATGGAAGCCGGAGATCCC) and SOCS3 G4 (guide sequence: GCGGCCGTGAAGTCCACAA), and the KD of SOCS3 was verified along with the original two guides, by RT-qPCR, which revealed that for three of the guides, G1, G2, and G4, there was sufficiently clear loss of transcription of SOCS3 (**Fig. 8C)**. However, while SOCS3 G4 repressed transcription, similar to G2 it also did not result in the depletion of mVenus foci signal of SOCS3 G1, suggesting that loss of peroxisome foci was a G1 specific effect, not linked to SOCS3. (**Fig. 9A)**.

At this point, it was of some importance to recollect an unalienable facet of CRISPR-Cas9 targeting systems, namely that all guides carry some capacity to have off-target effects. Off-target effects are when sgRNA targeting sequences will have partial (and sometimes full) complementation to other sites throughout the genome, thus causing Cas9 to target

multiple sites beyond the intended on-target site, and potentially affecting multiple genes (Tsai et al. 2014, Lin et al. 2014). While our results with multiple SOCS3 guides suggested that SOCS3 did not have an effect on peroxisome homeostasis, SOCS3 G1 clearly targets a gene that does play a role in peroxisome homeostasis. Immunofluorescence staining of SOCS3 G1 revealed that SOCS3 G1 specifically displayed a similar knockdown phenotype to PEX19 KD where both PMP70 and mVenus signal is diffuse, and was unlike a PEX5 KD where mVenus is diffuse but PMP70 signal is preserved, suggesting that SOCS3 G1 could potentially target the PEX19 gene for suppression (**Fig. 9B)**. Although different genomic sequences may have partial homologies to sgRNAs, it is not certain whether or not any particular potential off-target site will even be affected. RT-qPCR of PEX19 expression revealed that SOCS3 G1 specifically had a KD effect on PEX19 expression whereas our NTC guide and SOCS3 G4 guides did not, further concretizing the possibility that SOCS3 G1 was indeed an off-target (**Fig. 8B**).

To determine the sites of dCas9 binding in the genome when complexed with SOCS3 guides, we performed ChIP-Seq on the HA-tag of the dCas9-KRAB protein in HCT116 cells harboring NTC, SOCS3 G1, and SOCS3 G4 guides, enriching for DNA sequences that are targeted by the respective guides (**Fig. 10A**). NTC represents a non-targeting control (NTC) guide that should not bind to the promoter region of SOCS3 or any part of PEX19, serving as a control for having an sgRNA complex with Cas9 with no specificity. SOCS3 G1 is our test condition, in which we seek to determine whether or not it interacts with PEX19, and SOCS3 G4 serves as a negative control in that it should target the SOCS3 promoter region without having any interaction with PEX19. Indeed, in alignment with our hypothesis, the results of the ChIP-Seq show that not only does SOCS3 G1 target

both the promoter region of SOCS3 and the exon 1 of PEX19, it enriched for the exon1 of PEX19 more so than any other region in the genome other than its on-target sequence in the SOCS3 promoter (**Fig. 10B-C**).

To test whether or not the loss of SOCS3 or off-target loss of PEX19 in SOCS3 G1 was the responsible party in reducing mVenus-SKL foci signal, we created addbacks (reexpressions) of SOCS3 and PEX19 on hEF1a promoters such that they would not be affected by CRISPRi, in background SOCS3 G1 cells. Readout of peroxisome abundance via live-cell microscopy confirmed our suspicions that in SOCS3 G1 cells, addback of PEX19, but not SOCS3, restored peroxisome abundance, confirming that SOCS3 G1 effect on peroxisomes was due to an off-target suppression of PEX19 (**Fig. 10D**). As a note, the PEX19 reexpression construct may be affected by the off-target effect as well but was still aggressive enough in its expression to overcome even this. This corroborates the notion that the KD of SOCS3 truly has no substantive connection to peroxisomes, rather it was only the spurious sequence homology of one sgRNA that affected PEX19 leading to an interesting, but disappointing, false positive result. Our work also suggests that off-target effects of Cas9/CRISPR can be accurately mapped by ChIP-seq using affinity tags on Cas9.

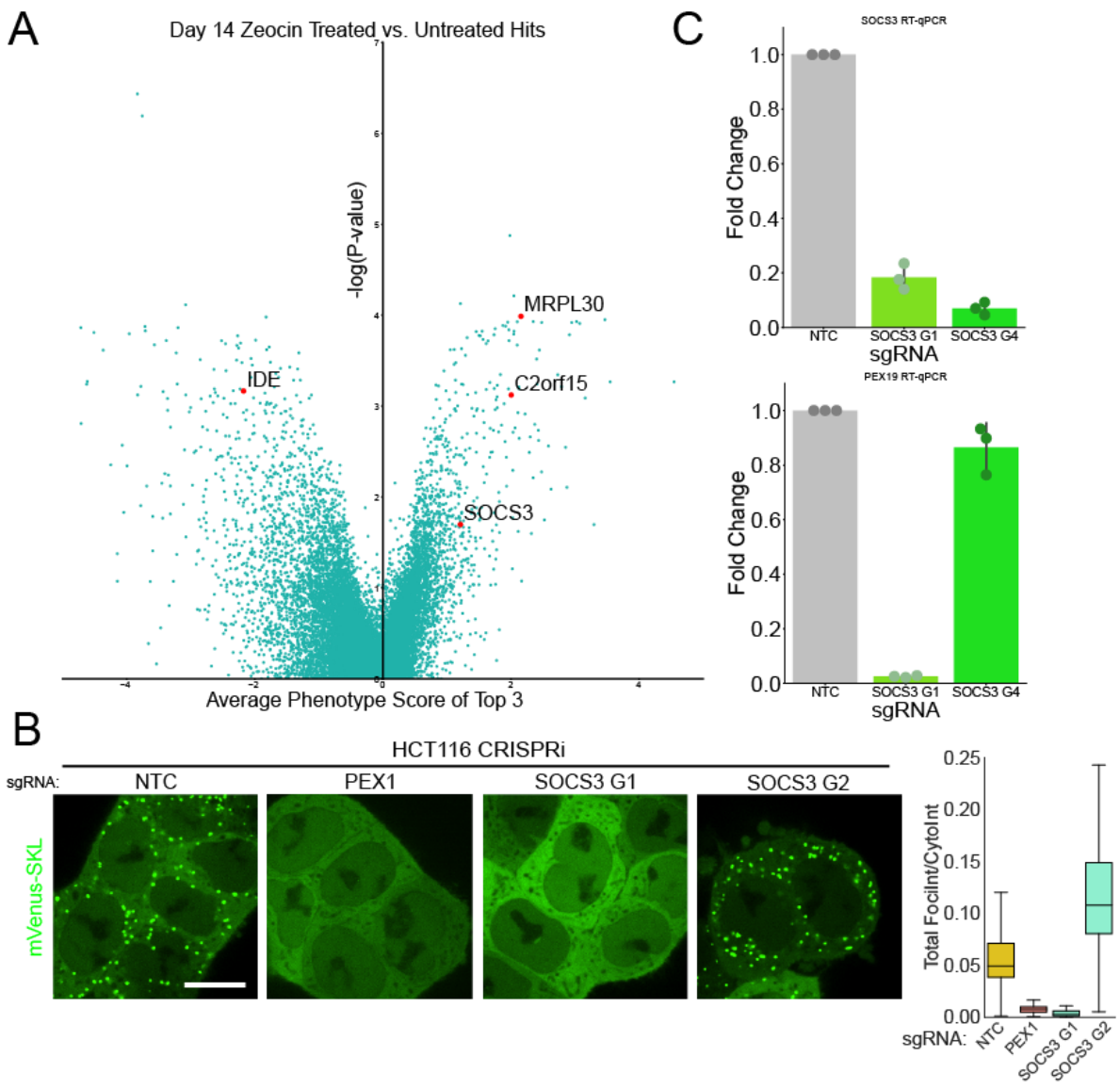

Figure 8. Dual screen strategy reveals and validates false-positive SOCS3.
(A) Volcano plot of NGS data from genome-wide screen with significance (-log base 10 of p-value, y-axis) and phenotype score (normalized fold change of cDNA guide count, x-axis) of guides targeting specific genes for cell cultures either untreated (DMSO mock treated) or treated (50ng/uL Zeocin treated) for 14 days. Red data points represent genes of interest. Data displayed was calculated from m=3 guides per gene and n=2 biological replicates. **(B)** Left Panels: Representative live cell microscopy images of mVenus-SKL signal in HCT116 2055 D01 cells harboring specified sgRNAs. m=1 samples n=32 images. Scale bar 10um. Right Panel: Quantification of total mVenus-SKL foci intensity/total cytoplasmic mVenus-SKL intensity of left panels. **(C)** RT-qPCR of HCT116 2055 D01 cells with specified sgRNAs quantifying fold change of transcripts for SOCS3 (upper panel) and PEX19 (bottom panel) normalized to NTC sgRNA expressing cells. n=3.

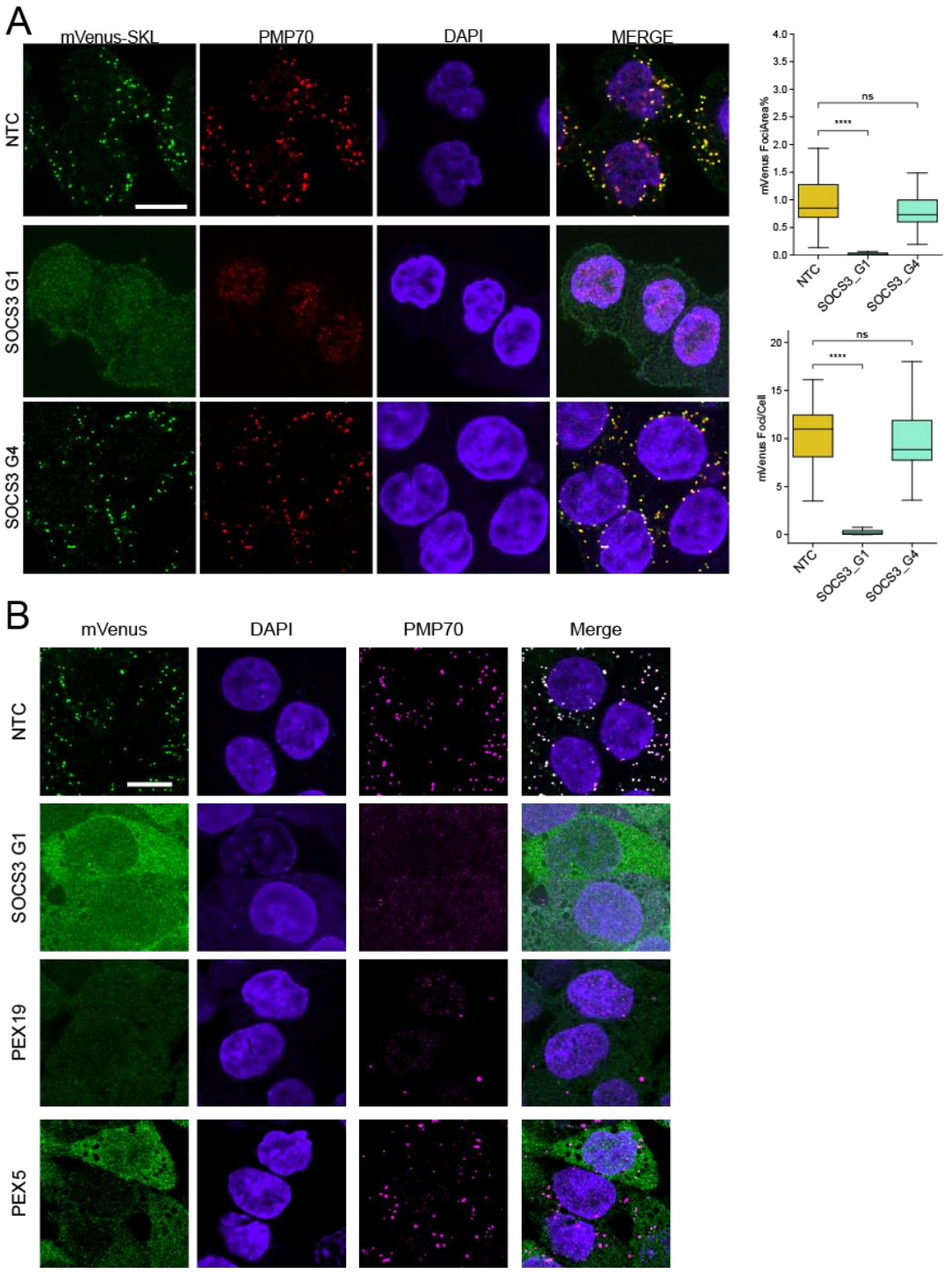

Figure 9. SOCS3 G1, but not SOCS3 G4, resembles a PEX19 KD.
(A) Left panels: Representative immunofluorescence microscopy images of HCT116 2055 D01 cells for (vertical axis) NTC, SOCS3 G1, and SOCS3 G4, staining for (horizontal axis) mVenus-SKL (green), PMP70 (red), and DAPI (blue). Right Panels: quantification of left panel mVenus-SKL foci area as a % of cell area, and of foci/cell. n=1 sample, n=24 images. Scale bar 10um. **(B)** Representative immunofluorescence microscopy images of HCT116 2055 D01 cells for (vertical axis) NTC, SOCS3 G1, PEX19, and PEX5 staining for (horizontal axis) mVenus-SKL (green), PMP70 (magenta), and DAPI (blue). n=1 sample, n=24 images. Scale bar 10um.

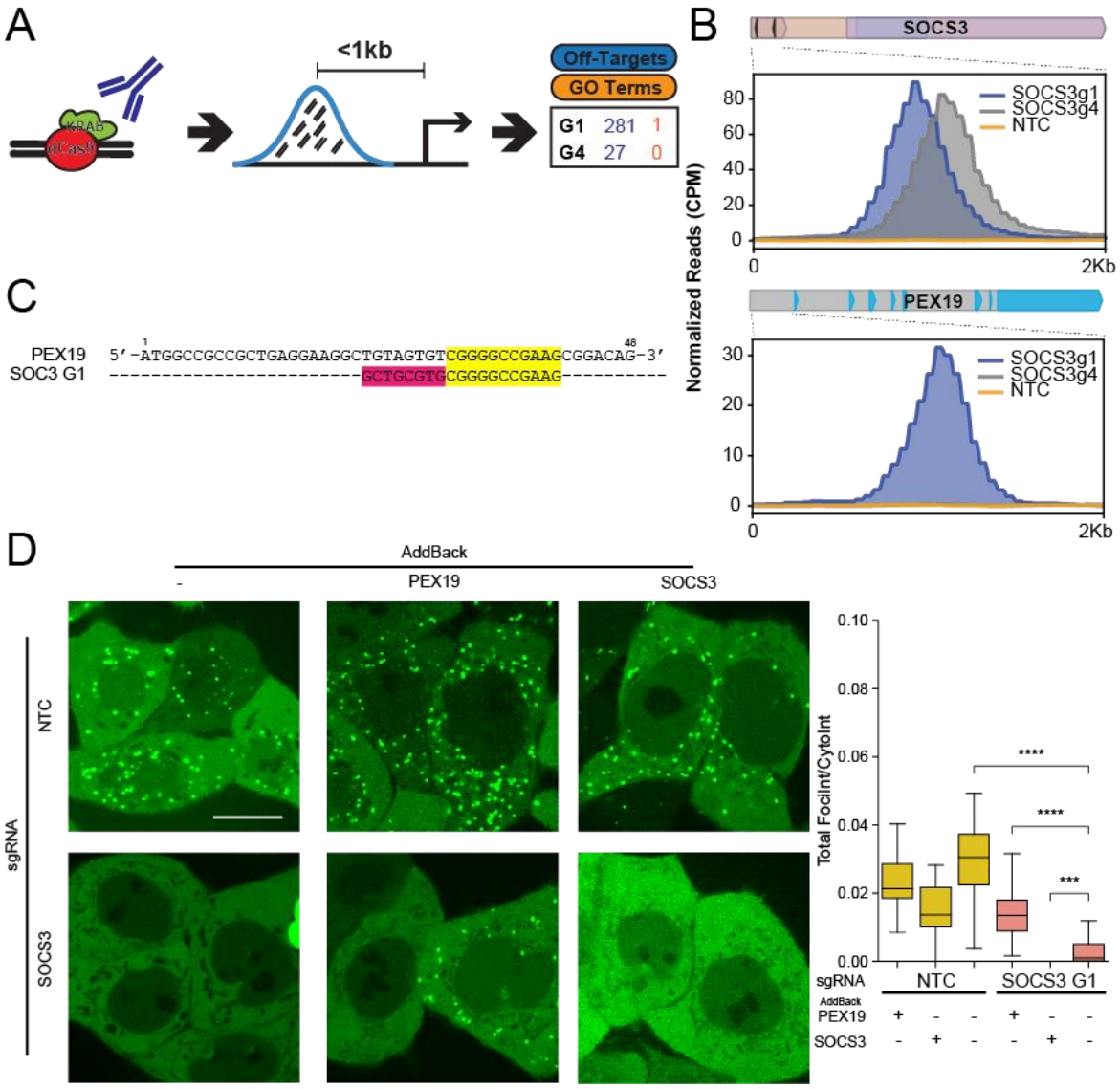

Figure 10. The peroxisome phenotype of SOCS3 G1 is based on PEX19 off-target activity.
(A) Schematic showing strategy for ChIP-seq of HA tagged Cas9 **(B)** ChIP-seq data showing histogram distributions of base reads for HCT116 CRISPRi 2055 D01 cells with sgRNAs for SOCS3 G1 (blue), SOCS3 G4 (grey), and NTC (orange), in the SOCS3 gene locus (upper) and PEX19 locus (lower). n=3. **(C)** Schematic showing the first 48 nucleotides of PEX19 (exon1) aligned with SOCS3 G1, where yellow represents homology and pink represents the portion of SOCS3 G1 that does not have homology. **(D)** Left Panels: Representative live cell microscopy images of mVenus-SKL signal in HCT116 2055 D01 cells reexpressing nothing (-), PEX19, or SOCS3, harboring specified sgRNAs. m=2 samples n=32 images. Scale bar 10um. Right Panel: Quantification of total mVenus-SKL foci intensity/total cytoplasmic mVenus-SKL intensity of left panels.

IV. Peroxisome homeostasis candidate - C2orf15/MRPL30.

C2orf15 is another candidate gene that was produced by the primary genetic screen where its knockdown increased its fitness in Zeocin treated conditions by at least 4-fold (**Fig. 8A**). However, upon further investigation, it was revealed that suppression of C2orf15 led to increased peroxisome abundance in our microscopy screening cell line, HCT116 2055 D01 (**Fig. 11A**). This was intriguing because based on our original screen logic, knockdowns that increased peroxisome abundance should sequester increased amounts of antibiotic resistance marker, and would thus sensitize cells to Zeocin treatment, reducing fitness. C2orf15 is poorly characterized and for that reason still remains to be named, because of this we first sought to verify that C2orf15 itself was being truly downregulated by our two sgRNAs. We found that, perplexingly, C2orf15 G1/G2 both did not affect C2orf15 transcript levels in any meaningful way (**Fig 11B**). Arraying C2orf15 sgRNAs sequences against the human genome, we found that the C2orf15 sgRNAs align in the same promoter region of MRPL30, where the Weissman CRISPRi V2 MRPL30 sgRNAs also align, sometimes overlapping with C2orf15 sgRNAs (**Fig. 11C**). It is important to note that C2orf15 is on the same chromosome as MRPL30 but is about 40,000 nucleotides away. RT-qPCR of MRPL30 transcripts of C2orf15 G1 and C2orf15 G2 expressing cells revealed that both guides depleted MRPL30 transcripts (**Fig. 11B)**. This would imply that the effect of the C2orf15 sgRNAs is not because of the C2orf15 gene, but because of its effect on MRPL30, the actual disguised candidate gene.

Mitochondrial Ribosomal Protein L30 (MRPL30) is, as the name implies, a mitochondrial ribosomal protein that is encoded by genes in the nucleus. In the primary screen, MRPL30 KD performance phenotype was similar to (mistargeted) C2orf15 KD,

consistent with the fact that they target the same gene (**Fig. 8A**). Future investigations of the role of MRPL30 on peroxisomes should consider that peroxisomes and mitochondria share proteins for fission (Schrader et al. 2022). Furthermore, there are quality control mechanisms on the membranes of mitochondria and peroxisomes that extract mislocalized transmembrane proteins (Weir et al. 2017). It could be the case that there is a homeostatic equilibrium between mitochondrial and peroxisomal proteins being maintained, and that a downregulation of mitochondrial proteins may result in increased peroxisome abundance, or that the cell is coping with loss of mitochondrial function and creating more peroxisomes to deal with some sort of stress of deficiency (Shpilka et al. 2022).

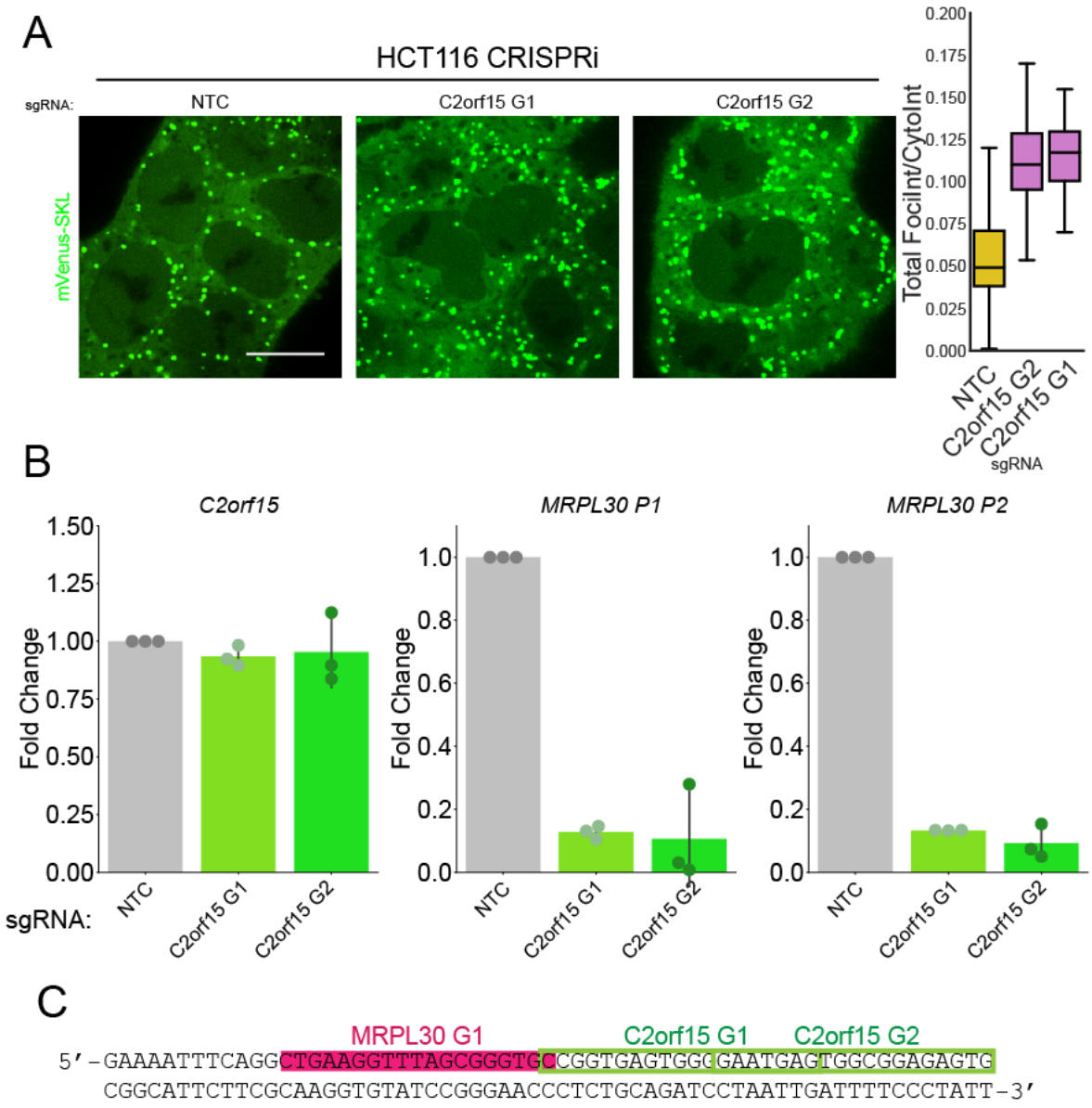

Figure 11. C2orf15 sgRNAs target the promoter region of MRPL30 causing increased peroxisomal foci. **(A)** Left Panels: Representative live cell microscopy images of mVenus-SKL signal in HCT116 2055 D01 cells harboring specified sgRNAs. m=1 samples n=32 images. Scale bar 10um. Right Panel: Quantification of total mVenus-SKL foci intensity/total cytoplasmic mVenus-SKL intensity of left panels. **(B)** RT-qPCR of HCT116 2055 D01 cells with specified sgRNAs quantifying fold change of transcripts for SOCS3 (upper panel) and PEX19 (bottom panel) normalized to NTC sgRNA expressing cells. n=3. **(C)** Schematic showing selected promoter region of MRPL30 and selected guides derived from the Weissman CRISPRi V2 library, MRPL30 G1 (magenta), C2orf15 G1/G2 (Green).

V. Peroxisome homeostasis candidate - IDE.

Alongside RNF146, the other most convincing (and parenthetically a very intriguing) gene to be uncovered by the CRISPRi and microscopy screens for genes influencing peroxisome import was insulin degrading enzyme (IDE), where depletion of the gene's expression resulted in a massive increase in the number and fluorescence intensity of mVenus-SKL foci, representing an increase in the import of peroxisome matrix cargo (**Fig. 8A, 12A**). This was found to replicate in our secondary reporter H4 CRISPRi astrocytoma cell line (**Fig. 12B**). This curious effect would suggest that IDE is nominally a suppressor of peroxisomes, either increasing peroxisome-specific autophagy, decreasing peroxisome biogenesis, or decreasing peroxisome import. IDE is a large homodimeric zinc metalloprotease, which presents itself as a spheroid globular protein with what has been described as having a cavity or clamshell created by its dimeric form, like two halves of walnut (Shen et al 2006, Aleshin et al. 2009), where potential substrates are recognized when encased by the dimer (Malito et al., 2008). IDE itself, eponymously, is a bit of a red herring in that, although it has been shown to degrade insulin *in vitro*, it has been shown to be able to degrade many other proteins and peptides, including, but not limited to, TGF-a, atrial natriuretic peptide, glucagon, amylin, and beta-endorphin (Gehm et al. 1991, Song et al 2006, Kurochkin et al. 2001, Ralat et al. 2011). Because of this seemingly sundry and omnifarious potential of target proteins/peptides and disputed localization, IDE does not seem to have a specific consensus sequence for its client proteins and peptides (Shen et al., 2006).

The two foremost characteristics of IDE that warranted investigation were the importance of its catalytic activity and its peculiar C-terminal signaling peptide. The main

peroxisomal targeting signal, PTS1, is a C-terminal tri-peptide with a conservative consensus of [S/A/C][K/R/H][L/M] where the combination of SKL is generally the most potent signal (Lametschwandtner et al. 1998). IDE is one such protein whose C-terminal tripeptide harbors a similar variant of AKL, thus suggesting import into the peroxisomal matrix. Moreover, IDE's PTS1 tag is conserved from creatures like sea urchins and fruit flies to platypus and gorillas, which may indicate that peroxisomal targeting of IDE is of evolutionary importance in the animal kingdom (**Table S7**). Previous studies have described IDE's peroxisomal localization, where deletion of the terminal tripeptide decreases peroxisomal localization (Chesneau et al. 1997), and have observed its effect on the degradation of thiolase, a PTS2 enabled peroxisome matrix localized protein, although the authors note that IDE is sparse in their sedimentation with peroxisomes (~10%) (Authier et al. 1995). Furthermore, the authors note that IDE has dual localization to both the cytoplasm and peroxisome, to the extent that even in the overexpression of IDE, combined with their digitonin permeabilization assays, IDE is still not purely localized to the peroxisomal matrix to the extent that thiolase or catalase are, reminiscent of dual localized proteins such as sterol carrier protein 2 (SCP2) (Authier et al. 1995, Ossendorp et al. 1993). Importantly, what Authier et al. discovered is that the PTS2 tag of thiolase (in a peptide form) competitively inhibits the degradation of radioactively labeled insulin by rat liver purified IDE (Authier et al. 1995). This evidence for IDE's function as a sort of processing protease correlates with other similar M16 proteases in its orthologue family such as the mitochondrial processing protease (PMPCB) (Teixeira et al. 2013, Koutnikova et al. 1998).

To interrogate the function of IDE, we designed multiple reexpression variants of IDE, to test the importance of IDE's localization via the AKL tripeptide and catalytic

activity at E111 (Hulse et al. 2009) (**Table S4**). The reexpression variants were expressed in HCT116 2055 D01 cells harboring either NTC or IDE sgRNAs. Indeed, in both NTC and IDE G1 background cells, the reexpression variants for pJV-0026-0029 had detectable IDE and FLAG, where the reexpression variant was immune to IDE G1 CRISPRi KD (**Fig. 13B)**. We found through live cell microscopy that, of the pJV_0026-0029 reexpression variants, the only one that restored (decreased) close to WT levels of mVenus-SKL foci signal intensity in background IDE KD cells was pJV_0027, the variant that has both the AKL and catalytic activity (**Fig. 13A**). This was important because it proved that IDE needed to be both catalytically active and, most likely, had to be localized properly to have its PTS1 related peroxisomal effect. Unexpectedly, all IDE variants when overexpressed in NTC background cells caused a *loss* in mVenus-SKL foci intensity (and thus peroxisome cargo import) relative to WT cells. This would suggest that only one half of the homodimer of IDE has to be catalytically functional or has to have the AKL tag to be sufficient in activity and, even more importantly, that the efficiency of peroxisome import is inversely correlated to the steady state abundance of IDE.

This astounding result prompted us to attempt to look at the proteomic profile of the IDE reexpression variants' interactors and client proteins. It was possible that IDE was directly interacting with peroxisomal matrix import cargo, and that pulldown of FLAG-IDE would reveal a full client list. We co-immunoprecipitated (CO-IP) our FLAG-IDE variants, with downstream LC-MS/MS to identify what possible peroxisomal proteins were being degraded by IDE (**Fig. 14A)**. There was also the added benefit that our catalytically dead variants might have stronger interactions with their cleavage targets and that our -AKL variants may help us control for cytoplasmic or non-peroxisome interactions. Despite the

CO-IP enriching for the FLAG-IDE variants, there were no peptides detected that would have indicated that any known PEX proteins nor peroxisomal matrix proteins were clients of our FLAG-IDE in any of the variant forms (**Table S5**).

We hypothesized, at this point, that perhaps IDE was degrading another regulator of peroxisome import, specifically an unknown peroxisome import enhancer. We selected various genes from our mass spectrometry results that looked promising and arrayed these genetic KDs in our HCT116 2055 D01 test cell line with either control scRNA or siRNA depleting IDE transcripts (**Table S6**). We reasoned that the hypothetical target enhancer would be found in the +AKL samples but not in the -AKL samples, that it might have an increased peptide count in the E111Q samples, and that if it were dually KD with IDE, cells would not have the increased import phenotype (**Fig. 14B)**. We found that none of our selected genes were the prospective enhancer that we were looking for, as none of the candidate genes when simultaneously suppressed with IDE exhibited restoration of peroxisome import to WT levels (**Fig. 14C)**.

Previous studies suggest that IDE co-sedimented with peroxisomes from rat liver, and that digitonin permeabilization assays enhanced colocalization of overexpressed IDE and catalase by IF (Authier et al. 1995). To ascertain whether or not IDE colocalized with peroxisomes we implemented three approaches: first to immunostain and acquire IF microscopy images of IDE localization, second to directly fuse mCherry to IDE to visualize localization, and third to attach an N-terminal AGPS-derived PTS2 tag to force IDE into the peroxisome to distinguish whether the AKL was functioning as an actual peroxisome import signal or had some other role.

Immunofluorescence of PMP70 and FLAG/IDE stained IDE reexpression cells revealed that IDE was largely found throughout the cytoplasm in both -AKL and +AKL cell lines. Despite there being some overlap between PMP70 and FLAG/IDE, it was not clear that IDE preferentially localized to the peroxisomal matrix unlike the overlap between mVenus and PMP70 (**Fig. 15A**). Additionally, it did not appear obvious that +AKL IDE variants were localizing with either mVenus or PMP70 at a greater frequency than -AKL IDE variants.

Similarly, the mCherry-IDE reexpression variants recapitulated IDE's cytoplasmic patterning, with overlap for the internal mVenus-SKL marker, and when stained for PMP70, overlapped with PMP70. However, because there was not a clear preferential sequestration or increase in intensity of mCherry-IDE when overlapped with PMP70 or mVenus-SKL it was not clear that this overlap was truly from IDE being imported into the peroxisomal matrix or from coincidental overlap due to how ubiquitous IDE was in the cytoplasm (**Fig. 15A)**. Similar to the FLAG-IDE variants it was unclear whether or not +AKL variants had increased colocalization with PMP70.

To test the function of IDE's AKL tripeptide, specifically whether or not it is purely for peroxisome internalization, we appended an N-terminal PTS2 tag derived from AGPS inspired from previous studies of PTS2 (Skowyra et al. 2022). The PTS2 tag, in theory, should act as a forcing mechanism to sequester IDE into the peroxisomal matrix, independent of its AKL tag, therefore if the AKL tag only has a function as a signaling peptide, the PTS2 should be an adequate substitute and the reexpression of PTS2-IDE sans AKL tripeptide (pJV_0040) should restore WT levels of mVenus-SKL import. However, if the AKL tripeptide has a significant role outside of peroxisomal import, the pJV_0040

construct should not restore the WT phenotype. Preliminary immunofluorescence microscopy of PTS2-IDE (pJV_0040/0041) again did not show IDE being forced into peroxisomes, that is, there was no clear increase of IDE into the peroxisome matrix relative to the cytoplasm (**Fig. 15B)**. In retrospect, all of the IF experiments would have benefitted from digitonin permeabilization to reduce the IDE signal in the cytoplasm and to verify if there was significant IDE import into the peroxisome.

An offshoot theory that we entertained was that IDE was directly degrading mVenus-SKL in WT cells, especially the mVenus-SKL that was inside the peroxisomal matrix. This would imply that there should be more mVenus-SKL in IDE KD cells relative to NTC cells. To test this theory, we immunoblotted mVenus in NTC and IDE cell lines, harboring either no addback constructs or one of the following: [pJV_0026, pJV_0027, pJV_0028, pJV_0029]. If IDE was actually degrading mVenus, we would expect that mVenus would be hyperstabilized in all IDE KD cells except for IDE KD cells with WT IDE (pJV_0027) reexpression. Furthermore, we would expect that there would be loss of signal in NTC cells harboring addbacks for IDE. Western blot data of the lysates of the aforementioned cell lines nullified this theory, none of the cell lines had any clear perceptible change in total cellular mVenus abundance (**Fig. 16A**). This would imply that IDE is not directly and fully degrading PTS1 peroxisomal cargo, and that loss of IDE or overexpression of IDE does not lead to perceptible changes in overall PTS1 cargo abundance. Another idea that was considered was that IDE may be degrading PEX5 itself. We found that immunoblot data of PEX5 abundance in various KD cell lines and an array of our IDE reexpression variants did not support this notion as none of the addback variants, or IDE KD by itself, seemed to strongly modify total PEX5 abundance (ignore the fading of

lane 9 and 10) (**Fig. 16B**). Additionally, with respect to this data, previous IF microscopy data staining for catalase and mVenus in NTC and IDE KD cells show that IDE KD cells have increased intensity in catalase foci and mVenus intensity relative to NTC cells providing supporting evidence for IDE as a peroxisome import regulator (**Fig. 16C)**.

As a matter of curiosity, and partly because we had already produced IDE reexpression variants, we pondered the possibility that the peroxisomal effect that IDE KD evokes might be interlinked with cell cycling. We dual stained cell lines corresponding to: HCT116 2055 D01[NTC sgRNA, IDE sgRNA, IDE sgRNA + pJV_0026, IDE sgRNA + pJV_0027, IDE sgRNA + pJV_0028, IDE sgRNA + pJV_0029] with propidium iodide (PI) and EdU, to measure levels of DNA abundance and thymidine incorporation, respectively, with readout via flow cytometry. Cells with low PI and EdU incorporation would represent G1-phase cells; only cells that were actively replicating DNA would incorporate EdU into their genome, thus representing S-phase cells; and cells that had increased PI staining, and thus DNA, but were low EdU due to not actively incorporating new nucleotides, would be G2-phase cells. We observed that cells that had suppressed IDE and cells that had non-WT IDE reexpression variants [pJV_0026, 0028, 0029] all had a stalled S-phase to G2-phase transition, resulting in a higher proportion of cells accumulating in S-phase compared to NTC (**Fig. 16D)**. This would imply that IDE's (probable) peroxisomal localization and its catalytic activity play a role in affecting cell cycle, especially S-phase.

In light of these mixed results, the mechanism by which IDE is recognizing and modifying peroxisome matrix cargo continues to be elusive. So far these results would seem to collectively imply that IDE requires both its catalytic activity and AKL tripeptide to act as a regulator of peroxisome import and does not appear to be fully degrading peroxisome

import cargo of the PTS1 sort. Based on available data, and other studies, one possible model is that IDE suppresses peroxisome import by recognizing and cleaving the signaling peptide of peroxisome matrix localized proteins, which would prevent import into the peroxisome matrix. In order for this phenomenon to occur, IDE needs its AKL to increase the probability by which it is brought into proximal vicinity of other PTS1 proteins by PEX5, where it would recognize and cleave proteins before they may ingress into the peroxisome. This model would be consistent with the changes in fluorescence intensity of mVenus, where cytoplasmic mVenus intensity actually decreases, and peroxisomal mVenus signal increases in an IDE KD cell line. In order to buttress this model, one avenue of exploration would be to subcellularly fractionate NTC and IDE KD cell lines arrayed with reexpression constructs, checking for IDE localization and any peroxisome import cargo such as catalase, mVenus-SKL, or thiolase. Any shift in the localization abundance of IDE reexpression constructs to either the cytoplasm or peroxisomal pellet fraction would indicate whether or not IDE is colocalized with the peroxisome using its PTS1 tag. Then, if IDE only regulates import and does not lead to protein degradation, firstly there should be no noticeable size shift in import cargo, secondly peroxisome cargo should be equal in abundance in the total fraction of all KDs and reexpression contructs, and thirdly peroxisome import cargo should be strongly concentrated in the peroxisomal pellet fraction while being depleted in the cytoplasmic fraction for IDE KD cells and IDE KD cells with non-WT reeexpression constructs. IDE KD cells with WT IDE addback should look similar to NTC sgRNA cells. NTC sgRNA cells with any overexpression construct should have increased cytoplasmic abundance of import cargo, and the share of pellet localized cargo should decrease.

The aforementioned experiment should answer the majority of the functional questions of IDE and would replicate older studies, although the precise recognition sequence of IDE would still not be revealed in this process. Further follow-up experiments, given that it is found that IDE degrades peroxisomal import cargo, could include site directed mutagenesis of terminal PTS1 signals, one residue at a time, to reveal a preferred motif, or lack thereof. It may be the case that IDE is promiscuous and indiscriminatory in its prey peptides, and thus relies on being shuttled by other targeting proteins to have localized activity. Another mechanistic insight that would be valuable would be how much of any particular peptide IDE cleaves. Assuming that IDE does indeed cleave signaling peptides, an *in vitro* assay that would reveal this process would involve incubating purified IDE with purified mVenus-SKL (or some other cargo protein), and then using size exclusion chromatography to separate the cleaved cargo from uncleaved cargo.

There still remains another model that has not been fully explored, as well, it could be the case that IDE is a promoter of pexophagy, and that knockdown of it causes peroxisome proliferation. A simple way to test this would be to treat NTC sgRNA expressing cells harboring overexpression constructs for IDE with bafilomycin, or an siRNA targeting a component of autophagy, and measuring via microscopy and western blotting changes in mVenus-SKL or other import cargo. If the selected autophagy inhibition strategy increases import in WT overexpression cell lines more so than restores import to NTC only samples, it would suggest that IDE is regularly inducing pexophagy.

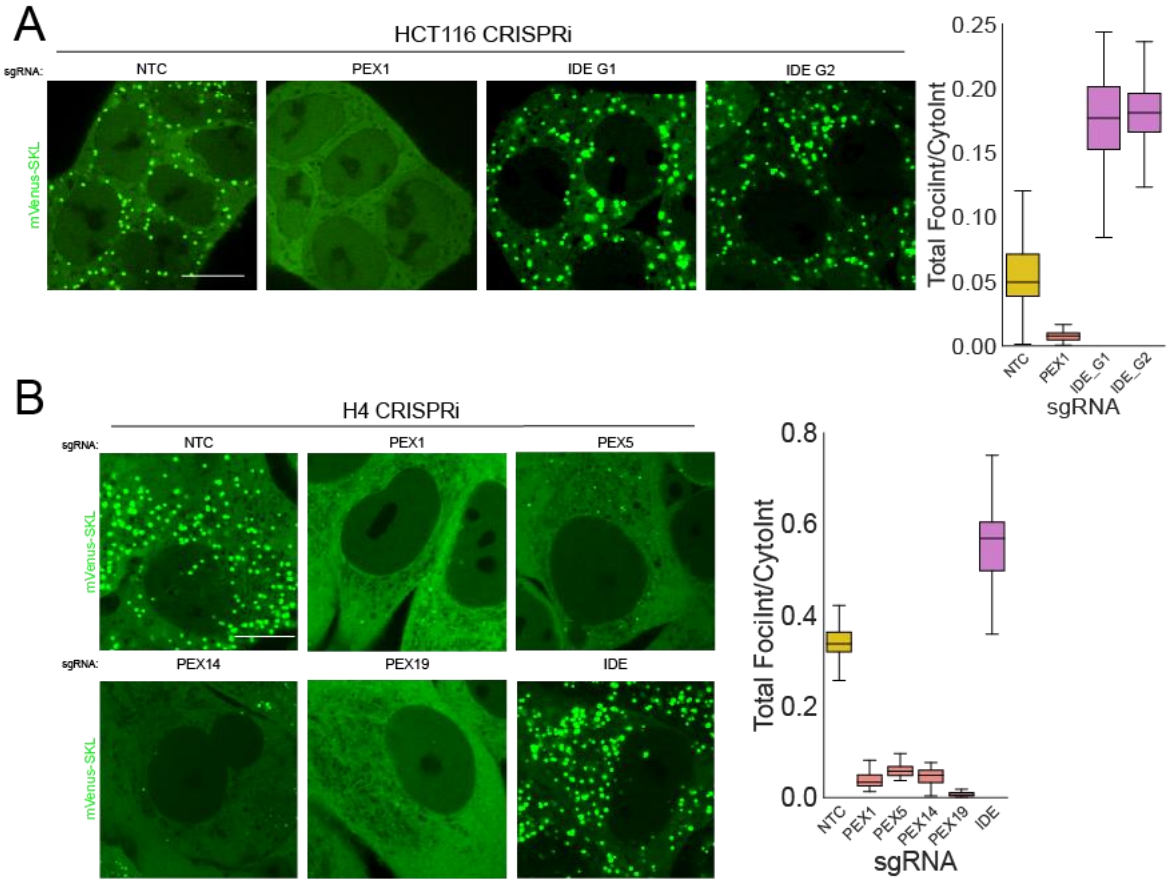

Figure 12. IDE KD causes increase in peroxisomal foci.
(A) Left Panels: Representative live cell microscopy images of mVenus-SKL signal in HCT116 2055 D01 cells harboring specified sgRNAs. m=1 samples n=32 images. Scale bar 10um. Right Panel: Quantification of total mVenus-SKL foci intensity/total cytoplasmic mVenus-SKL intensity of left panels. **(B)** Left Panels: Representative live cell microscopy images of mVenus-SKL signal in H4 2055 Z7 cells harboring specified sgRNAs. m=2 samples n=32 images. Scale bar 10um. Right Panel: Quantification of total mVenus-SKL foci intensity/total cytoplasmic mVenus-SKL intensity of left panels.

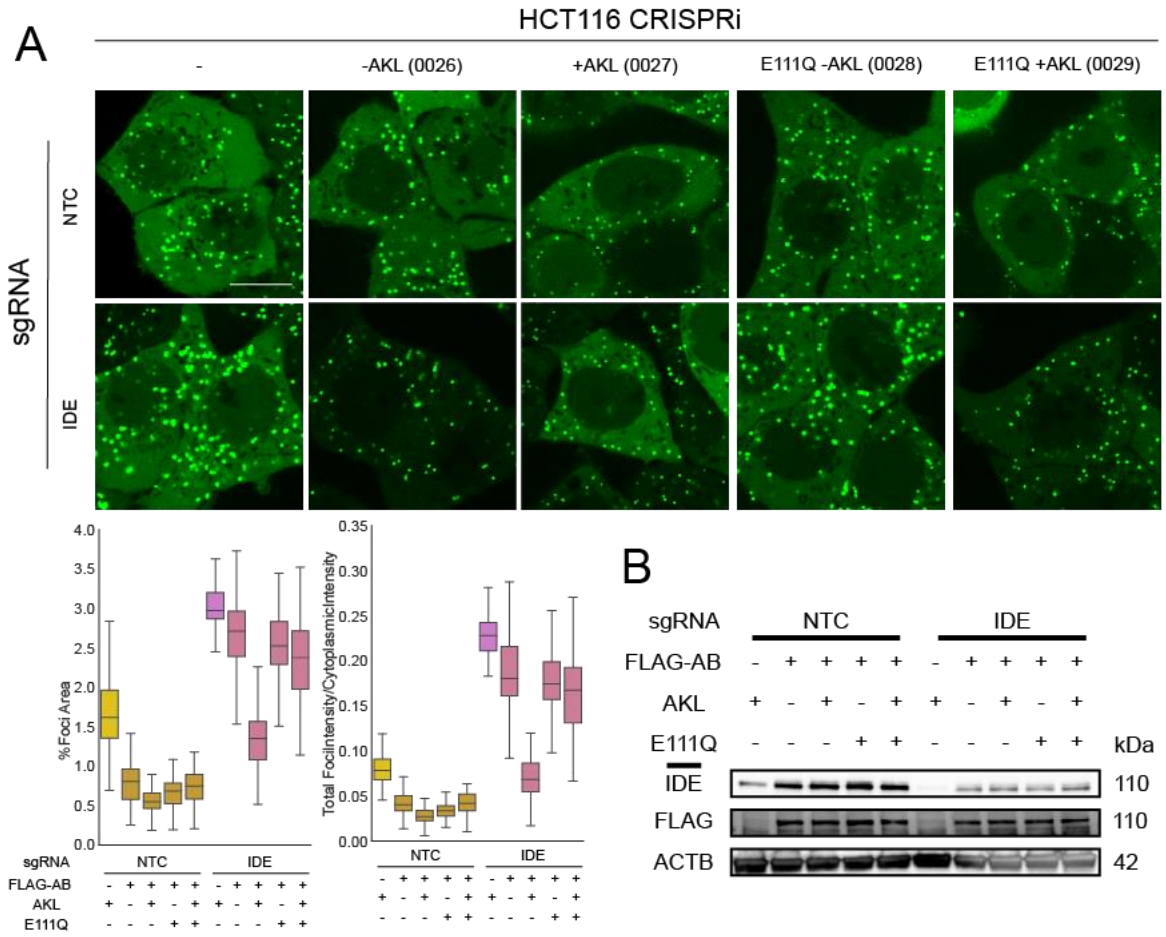

Figure 13. IDE nominally suppresses peroxisome homeostasis via its catalytic activity and PTS1 tag. **(A)** Western blot of lysate of HCT116 2055 D01 cells expressing NTC or IDE sgRNAs with no reexpression, or FLAG-IDE reexpressions with the indicated features: +/-AKL, +/- E111Q catalytic mutation. n=1 **(B)** Upper Panels: Representative live cell microscopy images of mVenus-SKL signal in HCT116 2055 D01 cells harboring specified sgRNAs and FLAG-IDE reexpression variants. m=2 samples n=32 images. Scale bar 10um. Bottom Panels: Quantification of foci area is a % of cytoplasmic area and total mVenus-SKL foci intensity/total cytoplasmic mVenus-SKL intensity of upper panels.

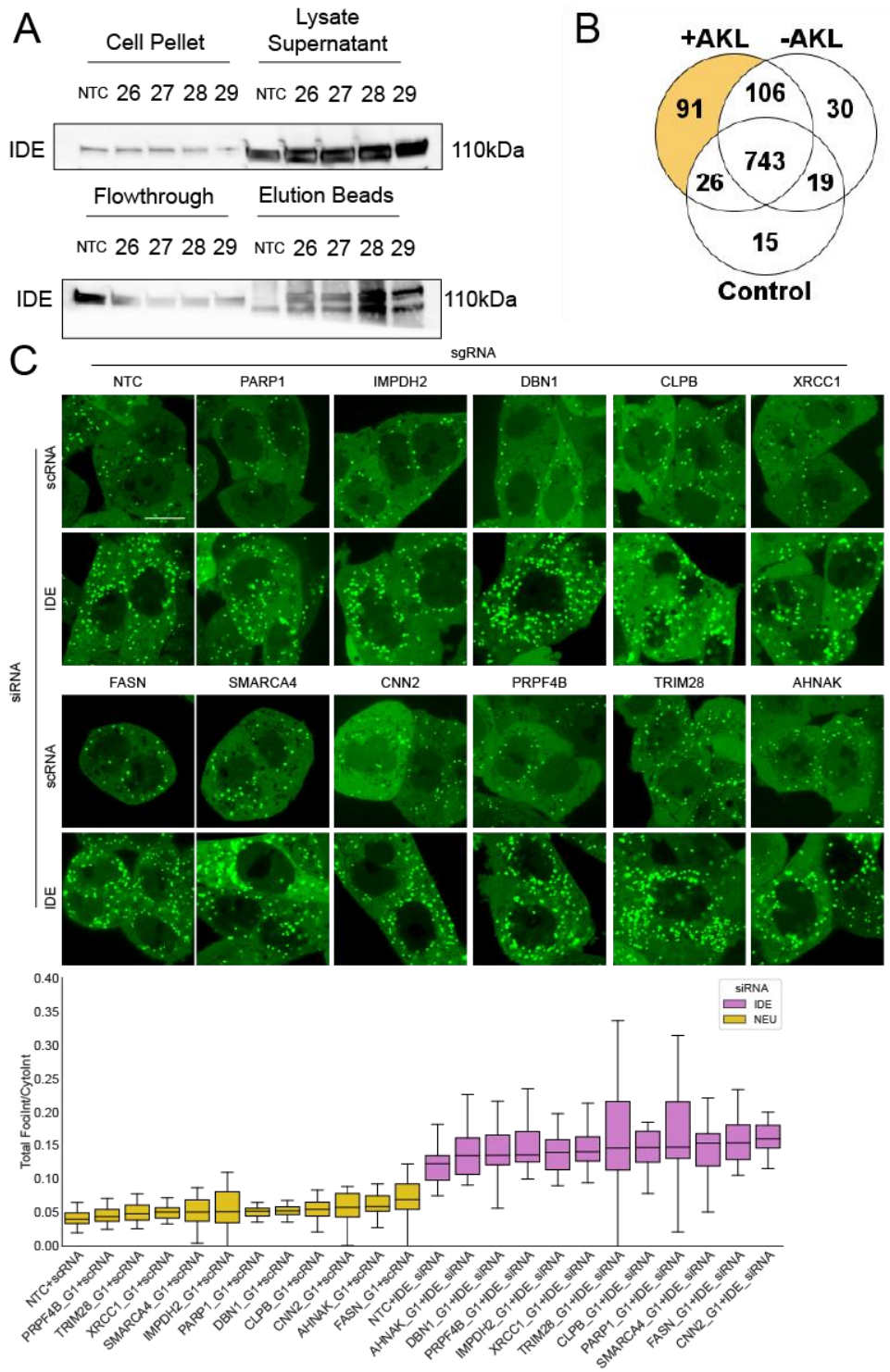

Figure 14. LC-MS/MS of IDE FLAG-IP does not reveal IDE peroxisome regulator target.
(A) Immunoblots of FLAG-IP fractions of HCT116 2055 D01 cells expressing NTC with no reexpression (lane 1,6), and IDE G1 (lane 2-5,7-10) with reexpressions for pJV_00[26-29] refer to **Table S4**. **(B)** Venn diagram (Scaffold) of mass spectrometry identified proteins partitioned into control groups (NTC) and samples with +AKL(27,29), and -AKL(26,28). **(C)** Upper Panels: Representative live cell microscopy images of mVenus-SKL signal in HCT116 2055 D01 cells harboring specified sgRNAs and treated with either scRNA or IDE siRNA 20nM. m=2 samples n=32 images. Scale bar 10um. Bottom Panels: Quantification of total mVenus-SKL foci intensity/total cytoplasmic mVenus-SKL intensity of upper panels.

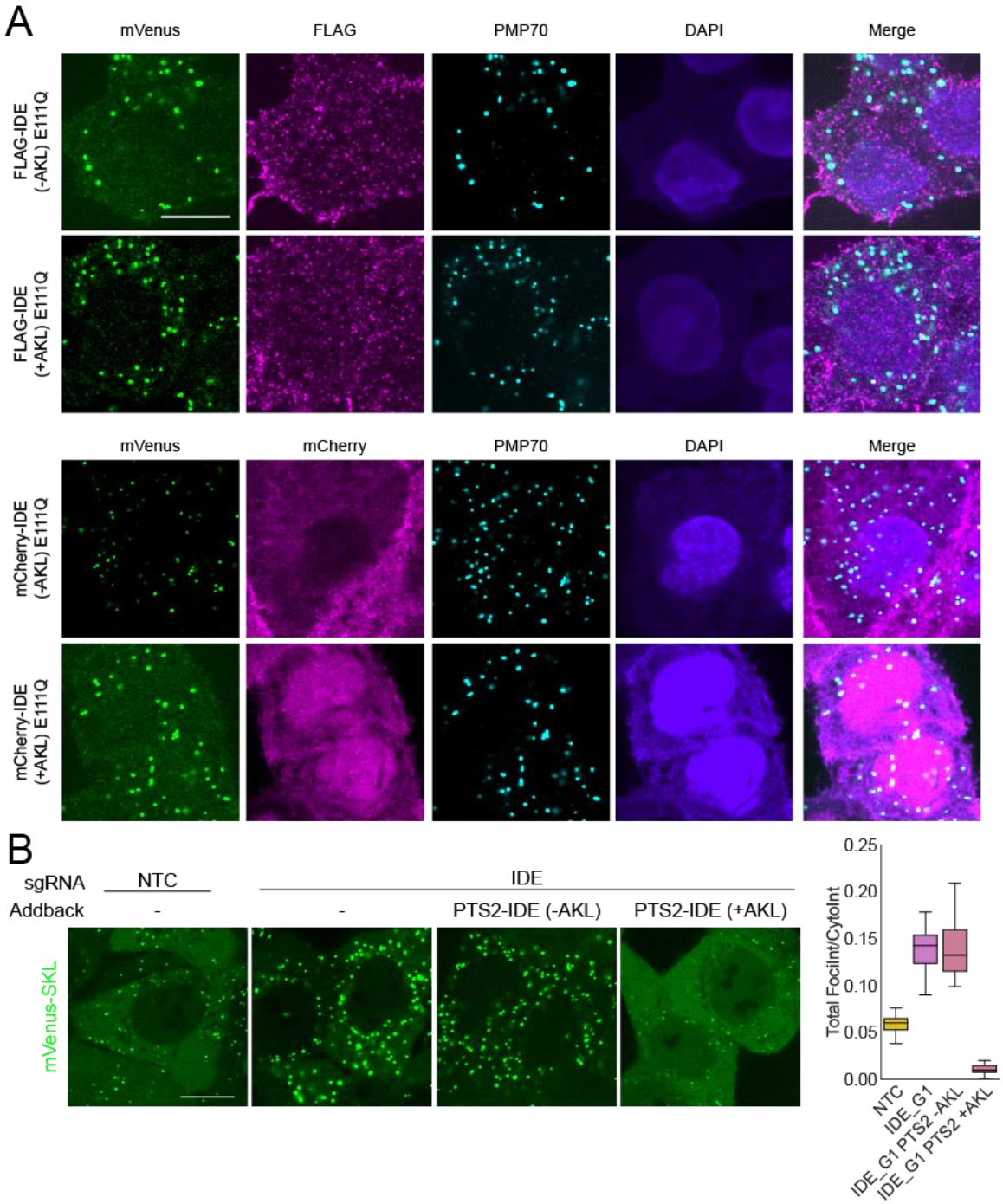

Figure 15. IDE overlaps with peroxisomes but does not have singular localization to the peroxisomal matrix.

(A) Representative immunofluorescence microscopy images of HCT116 2055 D01 cells with indicated reexpression constructs (vertical axis) staining for (horizontal axis) mVenus-SKL (green), FLAG or mCherry (red), PMP70 (teal), and DAPI (blue). n=2 samples, n=24 images. Scale bar 10um. **(B)** Left Panels: Representative live cell microscopy images of mVenus-SKL signal in HCT116 2055 D01 cells with NTC or IDE G1 sgRNAs reexpressing nothing (-), PTS2-IDE (-AKL), or PTS2-IDE (+AKL). m=2 samples n=32 images. Scale bar 10um. Right Panel: Quantification of total mVenus-SKL foci intensity/total cytoplasmic mVenus-SKL intensity of left panels.

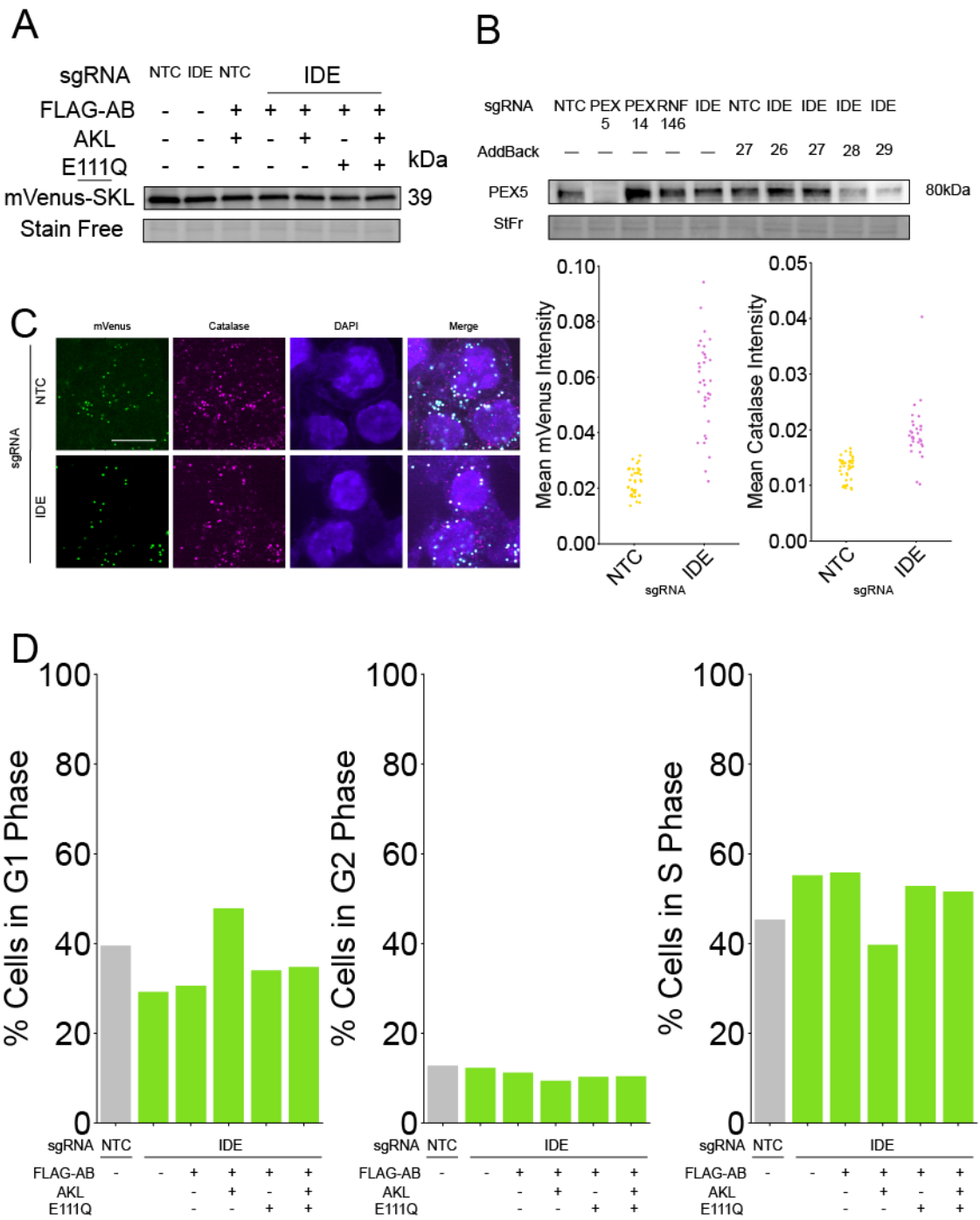

Figure 16. IDE does not strongly modulate PEX5 or PTS1 cargo stability but modulates localization. **(A)** Western blot of HCT116 2055 D01 cells with NTC or IDE G1 sgRNAs reexpressing nothing (-) or indicated FLAG-IDE variants (refer to Table S4 for pJV_00[26-29]), staining for mVenus-SKL(GFP). n=1 **(B)** Western blot of HCT116 2055 D01 cells with NTC, PEX5, PEX14, RNF146, or IDE G1 sgRNAs reexpressing nothing (-), or indicated FLAG-IDE variants (refer to Table S4 for pJV_00[26-29]), staining for PEX5. n=1 **(C)** Left panels: Representative immunofluorescence microscopy images of HCT116 2055 D01 cells with specified sgRNAs (vertical axis) staining for (horizontal axis) mVenus-SKL (green), catalase (red), and DAPI (blue). n=2 samples, n=24 images. Scale bar 10um. Right Panels: Quantification of mean mVenus and catalase intensity of left panels. **(D)** Quantification of % of cells stained with PI (DNA abundance) and EdU (thymine incorporation) representing, G1, G2, and S-phase, derived from flow cytometry data of HCT116 2055 D01 cells with NTC or IDE G1 sgRNAs with or without reexpression constructs referred to in **Table S4.** n=1.

Materials and Methods

Cell Lines, Culture Conditions, Lentiviral Production and Transduction

H4 dCas9-KRAB (a gift from the laboratory of Diego Acosta-Alvear, UCSB), HEK293T, and HCT116 dCas9-KRAB (a gift from the laboratory of J. Corn, ETH Zürich) cells were cultured in Dulbecco's Modified Eagle Media (10565018, DMEM, Gibco) supplemented with 10% fetal bovine serum (FBS, S11150H, R&D Systems), 1% penicillin/streptomycin (15140122, Gibco), and 2 mM L-Glutamine, and kept at 37°C and 5% CO_2 in a humidified incubator. Generation of lentivirus was performed by transfecting HEK293T cells with standard delta VPR and VSVG packaging vectors paired with TransIT-LTI Transfection Reagent (MIR2305, Mirus). Lentivirus was harvested 72 hrs following transfection and frozen at -80°C.

Zeocin resistance harboring HCT116 CRISPRi cell lines were constructed by transducing cells with lentivirus expressing mVenus-ZeoR-PTS1 constructs with either a PGK (pCR2054) or hEF-1α (pCR2055) promoter and 'spinfecting' cells in a centrifuge at 1000 rpm for 2 hrs. ZeoR expressing cells were single-cell sorted by flow cytometry (Sony SH800S) for mVenus expression at 488 nm excitation, where modestly fluorescent monoclonal cells were selected for both promoter types.

Re-expression constructs were made by Gibson cloning desired CDS sequences into the pLentiX-CD90 Thy1.1 vector backbone, with subsequent cell sorting of Thy1.1 positive cells by immunolabeling with CD90.1 Thy-1.1 antibody (17-0900-82, Thermo Scientific).

For drug treatment conditions, cells were treated with 50 nM bafilomycin (B1793, Sigma-Aldrich) for 15 hours, 5-10 µM hydroxychloroquine (H0915, Sigma-Aldrich) for 24 hours, 500 nM G007-LK (S7239, Selleck) for 24 hours, 1 µM XAV939 (575545, EMD Millipore) for 24 hours, and Carfilzomib (PR-171, Selleck) 10 µM for 4 hours.

For siRNA treatment conditions, cells were transfected with 10 nM of desired siRNA using Lipofectamine RNAiMAX (13778150, ThermoFisher) according to the manufacturer's protocol for 24-48 hrs.

iPS cells

AICS-0090-391 (WTC-CLYBL-dCas9-TagBFP-KRAB-cl391) cells were cultured in 10 ml sterile-filtered mTeSR-Plus (100-0276, STEMCELL) on a Matrigel-coated plate (354277, Corning) and grown to 80% confluency, five days post-thaw at 37°C and 5% CO2 in a humidified incubator. For routine passaging, at 80% confluency, media was aspirated and cells were washed with 4 ml room temp DPBS prior to dissociation. iPSCs were then treated with 2 ml pre-warmed Accutase (AT104, Stem Cell Technologies) and the vessel was incubated at 37ºC for 10 mins. Once cells began to detach, 4 mLs DMEM/F12 were added to the Accutase-treated cells and dissociated cells were triturated. Cells were rinsed with an additional 7 ml of DPBS for a final wash, and the dissociated cell suspension was transferred to a 15 ml conical tube and centrifuged at 500g for 5 min at room temp. DMEM/F12/Accutase supernatant was carefully aspirated and cells were resuspended in 10 ml fresh mTeSR-Plus containing 10µM Y-27632 2HCl (ROCK Inhibitor, S1049, Selleck) (ROCKi) and counted via flow cytometry. Cells were then seeded into a Matrigel-coated

six-well dish at a density of 1.5e+05 per well in 3 ml mTeSR-Plus containing ROCKi. Old media containing ROCKi was aspirated from each well the next day and replaced with fresh mTeSR1 without ROCKi. mTeSR-Plus was changed daily, and ROCKi was used for each passaging event, and always removed 24 hours thereafter. NPC differentiation was performed using DMEM/F12 (11320082, Gibco), 15% Knockout-Serum (10828028, Gibco), 1% Penicillin/Streptomycin, 20µM SB431542 (72234, Tocris), and 10ng/mL Noggin. NCSC control differentiation media is identical to NPC media except for 2µM BIO(S7198, Selleck). Cultures were differentiated for 17 days (or more), where differentiation was monitored by immunostaining for Oct4, Sox2, Pax6, and Hnk1. iPSC media, irrespective of maintenance or differentiation, was replaced every day. Cells harboring sgRNAs were maintained in 1µg/mL puromycin.

Genome-wide Pooled CRISPRi Screen and Analysis

HCT116 CRISPRi pCR2054 cells were transduced with lentivirus harboring constructs expressing sgRNAs from the genome-wide pooled CRISPRi v2 library with 8µg/mL of polybrene (TR-1003-G, EMD Millipore) at a multiplicity of infection (MOI) of <1. hCRISPRi-v2 library was a gift from Jonathan Weissman (Addgene ID #83969). Cells were then selected with 1.5 µg/mL puromycin (A1113803, Gibco) for 1 week in 15 cm dishes and expanded to 3.60 x 10^8 cells to allow for T0 condition takedowns as well as base seed for Zeocin (R25001, Invitrogen) treated and untreated samples. Treated cells were subjected to Zeocin 25 ng/µL final concentration and untreated cells were substituted with DMSO. Cells were maintained at >500X coverage per library element per replicate per condition throughout the screen. Cells were then cultured for 35 days in 5-Chamber CellStack vessels,

splitting cells every 48-72hrs. and harvesting 2.40 x 10^8 cells every 7 days per condition, where the treated and untreated conditions reached ~8 and ~16 doublings at day 14, respectively. Genomic DNA was purified using Macherey-Nagel NucleoSpin Blood XL Maxi Kit (740950.50, Macherey-Nagel) and prepared as previously described [Kampmann et al 2014] with modifications: Sbf1 (R3642S, NEB) was used instead of PvuII for the restriction digest. Next-Generation Sequencing (NGS) was performed using an Illumina NovaSeq SP with 2x50 paired end reads using custom read primers:

Read 1:

GTGTGTTTTGAGACTATAAGTATCCCTTGGAGAACCACCTTGTTGG

Read 2:

CTAGCCTTATTTAAACTTGCTATGCTGTTTCCAGCTTAGCTCTTAAAC

NGS data was then quantified and phenotype scores were generated using python scripts from the Horlbeck Lab's ScreenProcessing pipeline as previously described [Horlbeck et al 2016].

Immunofluorescence Staining

Cells were plated on glass bottom 96-well plates and fixed using 4% paraformaldehyde (15710, Electron Microscopy Sciences) in DPBS (14190250, Gibco) for 10 minutes and washed twice with DPBS. Cells were then permeabilized using 0.25% Triton X-100 (A16046.AP, Thermo Fisher) in DPBS for 10 minutes, blocked with 3% BSA (BP9703100, Fisher Scientific) in PBST (DPBS, Gibco; 0.1% Tween 20, AAJ20605AP, Thermo Fisher) for 30 minutes, and then probed with desired antibody in 3% BSA PBST for 1 hour at RT. Cells were then washed 3 times with PBST and incubated with secondary antibody and

DAPI (D1306, Invitrogen) in 3% BSA PBST for 1 hour at RT in darkness. Cells were then washed 3 times in PBST and stored in DPBS prior to image acquisition.

A list of antibodies used in the manuscript is available in **Table S3.**

Confocal Microscopy and Analysis

Fluorescent image acquisition was performed using a Nikon Eclipse Ti2 configured with a spinning disk confocal scanner (Yokogawa, CSU-W1), CFI Plan Apochromat Lambda D 40X air objective lens, CFI Apochromat TIRF 100X/1.49 oil-immersion objective lens, and NIS-Elements AR software (Nikon, version 5.31.01). Green (mVenus), blue (BFP, DAPI), red, and far red were excited with 488, 405, 561, and 640 nm lasers, respectively. Microscopy images were post-processed using ImageJ/FIJI software (version 2.0.0). Quantification and analysis of microscopy images was performed using CellProfiler [Stirling et al 2021] (version 4.2.4). For live cell images, acquired images were thresholded by global minimum cross entropy to select for and differentiate between cell cytoplasm area and mVenus foci area in an unbiased manner; downstream mVenus foci number, area, and intensity was measured within a range of size and ROI. For immunofluorescence microscopy, images were processed by, first, defining nuclei stained by DAPI by adaptive Otsu 3-class thresholding to differentiate between background and nuclei; second, by expanding from nuclei objects to define cytoplasm based on distance and Otsu 2-class thresholding and then subtracting nuclei from this area; third, by selecting, within the cytoplasm area, foci objects for mVenus, Catalase, or PMP70 of a defined size and ROI

determined by adaptive Otsu 3-class thresholding. All of the previously mentioned objects are then measured for number, area, intensity, and colocalization by Pearson's correlation.

Fluorescence-activated Cell Sorting

Flow cytometry was performed using an Attune NxT Flow Cytometer (Invitrogen) or SH800S (Sony). Excitation wavelengths of 488 nm (530/30 filter) and 405 nm (450/40 filter) were used to analyze mVenus and BFP expression, respectively. For selection of cells re-expressing PEX14 or PEX19, cells were sorted for Thy1.1 positive cells after immunolabeling with APC-conjugated CD90.1 Thy-1.1 antibody (17-0900-82, Thermo Scientific) at excitation wavelength of 638 nm (720/60 filter). FCS data was analyzed and visualized using FlowJo (version 10.6.2).

Immunoblotting

Cells were trypsinized (0.05% Trypsin, 25300062, Gibco), quenched, spun down at 300 x g for 5 minutes, decanted, and washed using DPBS (14190250, Gibco). Cells were lysed using RIPA lysis buffer (0.1% SDS, BP8200100, Fisher Scientific, 1% IPEGAL CA630, 8896, EMD-Millipore; 0.5% sodium deoxycholate, D6750, Sigma, 50mM Tris, BP152-5, Fisher Scientific; 150mM NaCl, S271-10, Fisher Scientific) with benzonase (101697, EMD Millipore) and protease inhibitor (78430, Thermo Scientific) for 30 minutes on ice and spun down at 14,000 rpm for 5 minutes and supernatant collected. Total protein concentrations were quantified using Bio-Rad Protein Assay (5000006, Bio-Rad). Protein samples were normalized to 10-20 µg, mixed with 4X Laemmli sample buffer (62.5mM Tris, 10% glycerol, 1%SDS, 0.005% bromophenol blue) containing beta-mercaptoethanol (M6250,

Sigma-Aldrich), and incubated for 5 minutes at 95 deg C. Samples were loaded and resolved on 4-20% SDS-PAGE gels (#4561095, Bio-Rad), semi-dry transferred to 0.45 µm LF PVDF membranes (1620264, Bio-Rad), blocked in 5% milk (Nestle) in TBST (50mM Tris, 150mM NaCl, pH 7.4), and probed with desired antibody in 3% BSA TBST (BSA, BP9703100, Fisher Scientific) overnight at 4C. Membranes were then washed and probed with secondary HRP-conjugated antibodies, with visualization of chemiluminescence using Pierce ECL2 Western Blotting Substrate (PI80196, Thermo Scientific) on a ChemiDoc MP Imaging System (Bio-Rad).

PI EdU Cell Cycle Stain

EdU(A10044, Invitrogen) is prepared (at 10uM final (1000X dilution) in 37C prewarmed cell appropriate media, and cells are incubated for 20 minutes to 1 hour. Cells are then washed once with 5 ml of ice cold DPBS, stopping replication. Cells are lifted, washed, and then 150 µL of 4 % PFA in PBS is added, mixed, and incubated for 10 minutes protected from light. Fixative is removed and cells are washed with 1 mL of DPBS. Wash solution is removed and resuspended in 200 µL of 0.5% Triton®X-100 in DPBS (10ml + 500ul of 10% triton) and incubated for 15 minutes on ice. Sodium Ascorbate reaction cocktail is prepared in order of addition of 880uL of Reaction Buffer (50 mM Tris, 150 mM NaCl, pH 7.5. Dissolve 3.02 g of Tris, 4.4 g of NaCl in 500 mL of water, adjust pH to 7.5, sterile filter), 20uL of copper sulfate 50mM (C1297, Sigma), 4uL of sodium azide 2mM (S2002, Sigma) (unstable made fresh), and 100uL of 11.1mg/mL sodium ascorbate (PHR1279, Sigma) (unstable made fresh). Cells are spun down at 800 x g and 150ul of the reaction cocktail is added to each tube, and briefly vortexed. Cells are then incubated at RT

for 30 min. in the dark. Cells are then washed once with 1 mL of 0.5% Triton X-100 in DPBS, spun down, and supernatant decanted. Each cell sample is resuspended in 500uL of DPBS, 1uL of RNAse A, and 5uL of PI (1mg/mL, P4170, Sigma) and then incubated at 37C for 10 minutes.

TOPFlash

HEK293T ZIM3-dCas9 and HCT116 dCas9-KRAB cells harboring NTC, PEX14, and PEX19 sgRNAs were transfected in 96-well plates by lipofectamine (TransIT LT-1, Mirus). A normalized 55 ng of total plasmid DNA was used at a ratio of 50:5 TOPFlash/FOPFlash:Renilla. Cells were treated with either BSA or human recombinant WNT3a (5036-WN-010, R&D Systems) 24 hours later. Cells were then lysed 24 hours after treatment and luciferase activity was measured using the Dual Luciferase Assay (E1910, Promega) according to manufacturer's protocol, and luminosity was read out using a microplate reader (SpectraMax M5, Molecular Devices). Plasmids used were: TopFLASH (Addgene#12456), FopFLASH (Addgene#12457), Renilla (Addgene#27163). M50 Super 8x TOPFlash and M51 Super 8x FOPFlash (TOPFlash mutant) were a gift from Randall Moon (Addgene plasmid # 12456, #12457) [Veeman et al 2003]. pRL-SV40P was a gift from Ron Prywes (Addgene plasmid # 27163) [Chen and Prywes 1999].

Subcellular Fractionation

Designated cell lines were harvested at 25-30 million cells (equalized among experimental replicates), spun down, washed, and resuspended in Homogenization Buffer (HB) (250 mM sucrose, 5 mM MOPS, 1 mM EDTA, 2 mM PMSF, 1 mM DTT, 1 mM ε-aminocaproic acid,

pH 7.4 adjusted with KOH) based on Manner and Islinger et al. 2018. Cells were quickly freeze thawed and mechanically homogenized via dounce, with a minimum of 10 passes, to lyse the extracellular membrane while retaining intracellular organelles. Total lysate was collected. The remainder of the product was centrifuged at 600 × g max, 10 min, 4 ℃, the supernatant collected, pellet was then collected and resuspended with HB, homogenized via dounce, with a minimum of 10 passes again, centrifuged at 600 × g max, 10 min, 4 ℃, supernatant collected and combined with previously collected supernatant, whereas the remaining pellet is considered the nuclear pellet. The supernatant was then fractionated at 20,000xg for 30 minutes at 4°C. The fractionated supernatant was harvested (cytoplasmic fraction), leaving behind the heavy mitochondrial/light mitochondrial/peroxisomal organellar pellet. The pellet is washed by resuspension in 1 mL of homogenization buffer, spun down at 20,000xg for 15 minutes at 4°C, the wash supernatant is discarded, and then washed again in the same manner. The resulting organellar pellet is lysed by RIPA lysis buffer; this is considered the cell pellet.

Co-Immunoprecipitation

Designated cell lines were harvested at 10-15 million cells (equalized among experimental replicates), spun down, and resuspended in LB1 (60 mM HEPES pH 7.6, 150 mM NaCl, 150 mM KCl, 10 mM MgCl2, 0.2% IPEGAL CA630 (Sigma), 0.1% sodium deoxycholate (Sigma), 1X Protease Inhibitor, with or without 1X Benzonase). For FLAG-IP assaying for PARsylation: no benzonase, 1 µM PARGi, and 10 µM carfilzomib was included in the LB1. The suspension quickly undergoes freeze-thaw, is then dounce homogenized (with a minimum of 10 passes), and then is incubated for 30 minutes at 4°C with inversion. Total

lysate samples are acquired and the remaining lysate is centrifuged for 5 min, 20,000xg at 4°C to separate the sample into soluble and insoluble fractions. The supernatant (soluble fraction) is collected and spun at 20,000 xg at 4°C for 30 minutes to clear out any remaining insoluble proteins or cell debris, this is the lysate supernatant. The insoluble fraction is washed with LB1, spun down, decanted, and resuspended in LB1, this is the pellet. In an optional step, the lysate supernatant is pre-cleared with protein G agarose beads for 30 minutes at 4°C and washed. For FLAG-IPs, supernatant is incubated with M2 FLAG conjugated agarose beads (M8823, Millipore) for 2-3 hrs at 4°C with inversion. For TNKS immunoprecipitations, supernatant is incubated with 10 µg of TNKS antibody (sc-365897, Santa Cruz Biotech) for 3 hrs at 4°C with inversion, and then conjugated to Protein G Dynabeads (10004D, Invitrogen) for 3hrs. at 4°C with inversion. Beads are then washed 5X in LB2 buffer (LB1 buffer without protease inhibitors or benzonase) with either centrifugation or magnetic stand (where applicable). Beads are then eluted using 50 µL of freshly prepared (day of) Elution Buffer (100 mM $NaHCO_3$, 1% SDS) at 65°C for 15 min on a heated shaker (1200 rpm) twice, or for FLAG-IP assaying for PARsylation, 90ul of 300ug/ml FLAG peptide is dissolved in LB2, and samples are eluted at 4°C shaking at 1100rpm for 30 minutes, then spun down, and supernatant is collected.

RNA-Seq

HCT116 Pex-ZeoR cell lines harboring either NTC or RNF146 sgRNAs were harvested, spun down, and RNA was extracted using RNeasy Mini Kit (Qiagen #74104) according to manufacturer instructions, in triplicate. Purified RNA samples were poly-(A) enriched, reverse transcribed, and sequenced on an Illumina NovaSeq to produce paired-end 150 bp

reads (Novogene). Raw fastq reads were trimmed using fastp v0.23.2 [Chen et al. 2018], alignment was done via STAR v 2.7.11a [Dobin et al. 2013], count tables were generated using htseq2 v. 2.0.2 [Putri et al. 2022] and differential expression analysis was performed using the R-package DESeq2 v. 1.40.1 [Love et al. 2014]. Differential expression comparisons were made between experimental and nontargeting CRISPRi strains in biological triplicate.

ChIP-Seq

ChIP-Seq is performed according to Weinert et al. 2019, the following is a near quote of their methods section: Between 2×10^6 to 1×10^7 cells were used for each immunoprecipitation. For each ChIP-Seq of edited cells we also performed ChIP-Seq on cells that have been edited with a non-targeting sgRNA. Cells were harvested and single cell suspensions in growth media without supplement were prepared by passing cell suspension through a 23G needle. Single cells were crosslinked with 1% formaldehyde for 15 min at room temperature, and the reaction was quenched with glycine at a final concentration of 125 mM. Crosslinked cells were then lysed on ice following a three step protocol: Lysis buffer (LB) 1 for 10 min (50 mM Hepes–KOH, pH 7.5; 140 mM NaCl; 1 mM EDTA; 10% glycerol; 0.5% NP-40 or Igepal CA-630; 0.25% Triton X-100, all Sigma), LB2 for 5 min (10 mM Tris–HCl, pH8.0; 200 mM NaCl; 1 mM EDTA; 0.5 mM EGTA, all Sigma) and nuclei were then resuspended in LB3 (10 mM Tris–HCl, pH 8; 100 mM NaCl; 1 mM EDTA; 0.5 mM EGTA; 0.1% Na–Deoxycholate; 0.5% N-lauroylsarcosine, all Sigma). Nuclei suspensions in LB3 were then sonicated to obtain ~ 300–500 bp fragments of chromatin. After sonication Triton-X100 (Sigma) was added to a final concentration of 1% and adjusted

with LB3 to 3 mL total volume per IP. Fragmented chromatin was pulled down rotating at 4 °C overnight using antibodies against HA (ab9110, Abcam), bound to 100 µl of protein A dynabeads (Invitrogen). Beads were washed six times with RIPA buffer (50 mM Hepes–KOH, pH 7.5; 500 mM LiCl; 1 mM EDTA; 1% NP-40 or Igepal CA-630; 0.7% Na–Deoxycholate, all Sigma) and once with TBS (20 mM Tris–HCl, pH 7.6; 150 mM NaCl). Crosslinking was then reversed and DNA was eluted from beads rotating at 65 °C overnight in elution buffer 50 mM Tris–HCl, pH 8; 10 mM EDTA; 1% SDS). DNA was purified using a PCR clean up kit (Qiagen). Libraries are prepped via TruSeq DNA Nano Kit (Illumina).

References

Abe, Y., Honsho, M., Itoh, R., Kawaguchi, R., Fujitani, M., Fujiwara, K., Hirokane, M., Matsuzaki, T., Nakayama, K., Ohgi, R., Marutani, T., Nakayama, K. I., Yamashita, T., & Fujiki, Y. (2018). Peroxisome biogenesis deficiency attenuates the BDNF-TrkB pathway-mediated development of the cerebellum. Life Science Alliance, 1(6), e201800062. https://doi.org/10.26508/lsa.201800062

Aleshin, A. E., Gramatikova, S., Hura, G. L., Bobkov, A., Strongin, A. Y., Stec, B., Tainer, J. A., Liddington, R. C., & Smith, J. W. (2009). Crystal and solution structures of a prokaryotic m16b peptidase: An open and shut case. Structure, 17(11), 1465–1475. https://doi.org/10.1016/j.str.2009.09.009

Andrabi, S. A., Kang, H. C., Haince, J.-F., Lee, Y.-I., Zhang, J., Chi, Z., West, A. B., Koehler, R. C., Poirier, G. G., Dawson, T. M., & Dawson, V. L. (2011). Iduna protects the brain from glutamate excitotoxicity and stroke by interfering with poly(ADP-ribose) polymer-induced cell death. Nature Medicine, 17(6), 692–699. https://doi.org/10.1038/nm.2387

Antonenkov, V. D., & Hiltunen, J. K. (2006). Peroxisomal membrane permeability and solute transfer. Biochimica et Biophysica Acta (BBA) - Molecular Cell Research, 1763(12), 1697–1706. https://doi.org/10.1016/j.bbamcr.2006.08.044

Aoi, T., Yae, K., Nakagawa, M., Ichisaka, T., Okita, K., Takahashi, K., Chiba, T., & Yamanaka, S. (2008). Generation of pluripotent stem cells from adult mouse liver and stomach cells. Science, 321(5889), 699–702. https://doi.org/10.1126/science.1154884

Authier, F., Bergeron, J. J., Ou, W. J., Rachubinski, R. A., Posner, B. I., & Walton, P. A. (1995). Degradation of the cleaved leader peptide of thiolase by a peroxisomal proteinase. Proceedings of the National Academy of Sciences of the United States of America, 92(9), 3859–3863. https://doi.org/10.1073/pnas.92.9.3859

Bhardwaj, A., Yang, Y., Ueberheide, B., & Smith, S. (2017). Whole proteome analysis of human tankyrase knockout cells reveals targets of tankyrase-mediated degradation. Nature Communications, 8(1), 2214. https://doi.org/10.1038/s41467-017-02363-w

Braverman, N. E., Raymond, G. V., Rizzo, W. B., Moser, A. B., Wilkinson, M. E., Stone, E. M., Steinberg, S. J., Wangler, M. F., Rush, E. T., Hacia, J. G., & Bose, M. (2016). Peroxisome biogenesis disorders in the Zellweger spectrum: An overview of current diagnosis, clinical manifestations, and treatment guidelines. Molecular Genetics and Metabolism, 117(3), 313–321. https://doi.org/10.1016/j.ymgme.2015.12.009

Braverman, N., Steel, G., Obie, C., Moser, A., Moser, H., Gould, S. J., & Valle, D. (1997). Human PEX7 encodes the peroxisomal PTS2 receptor and is responsible for rhizomelic chondrodysplasia punctata. Nature Genetics, 15(4), 369–376. https://doi.org/10.1038/ng0497-369

Cadena, E. (2015). A global phylogeny of Pelomedusoides turtles with new material of Neochelys franzeni Schleich, 1993 (Testudines, podocnemididae) from the middle Eocene, Messel Pit, of Germany. PeerJ, 3, e1221. https://doi.org/10.7717/peerj.1221

Carow, B., & Rottenberg, M. E. (2014). Socs3, a major regulator of infection and inflammation. Frontiers in Immunology, 5. https://doi.org/10.3389/fimmu.2014.00058

Chambers, S. M., Fasano, C. A., Papapetrou, E. P., Tomishima, M., Sadelain, M., & Studer, L. (2009). Highly efficient neural conversion of human ES and iPS cells by dual inhibition of SMAD signaling. Nature Biotechnology, 27(3), 275–280. https://doi.org/10.1038/nbt.1529

Chambers, S. M., Qi, Y., Mica, Y., Lee, G., Zhang, X.-J., Niu, L., Bilsland, J., Cao, L., Stevens, E., Whiting, P., Shi, S.-H., & Studer, L. (2012). Combined small-molecule inhibition accelerates developmental timing and converts human pluripotent stem cells into nociceptors. Nature Biotechnology, 30(7), 715–720. https://doi.org/10.1038/nbt.2249

Chen, S., Zhou, Y., Chen, Y., & Gu, J. (2018). Fastp: An ultra-fast all-in-one fastq preprocessor. Bioinformatics, 34(17), i884–i890. https://doi.org/10.1093/bioinformatics/bty560

Chen, X., & Prywes, R. (1999). Serum-induced expression of the cdc25a gene by relief of e2f-mediated repression. Molecular and Cellular Biology, 19(7), 4695–4702. https://doi.org/10.1128/MCB.19.7.4695

Chesneau, V., Perlman, R. K., Li, W., Keller, G.-A., & Rosner, M. R. (1997). Insulin-degrading enzyme does not require peroxisomal localization for insulin degradation*. Endocrinology, 138(8), 3444–3451. https://doi.org/10.1210/endo.138.8.5344

Dammai, V., & Subramani, S. (2001). The human peroxisomal targeting signal receptor, pex5p, is translocated into the peroxisomal matrix and recycled to the cytosol. Cell, 105(2), 187–196. https://doi.org/10.1016/S0092-8674(01)00310-5

DaRosa, P. A., Wang, Z., Jiang, X., Pruneda, J. N., Cong, F., Klevit, R. E., & Xu, W. (2015). Allosteric activation of the RNF146 ubiquitin ligase by a poly(ADP-ribosyl)ation signal. Nature, 517(7533), 223–226. https://doi.org/10.1038/nature13826

Defourny, J., Aghaie, A., Perfettini, I., Avan, P., Delmaghani, S., & Petit, C. (2019). Pejvakin-mediated pexophagy protects auditory hair cells against noise-induced damage. Proceedings of the National Academy of Sciences, 116(16), 8010–8017. https://doi.org/10.1073/pnas.1821844116

Deosaran, E., Larsen, K. B., Hua, R., Sargent, G., Wang, Y., Kim, S., Lamark, T., Jauregui, M., Law, K., Lippincott-Schwartz, J., Brech, A., Johansen, T., & Kim, P. K. (2012a).

NBR1 acts as an autophagy receptor for peroxisomes. Journal of Cell Science, jcs.114819. https://doi.org/10.1242/jcs.114819

Deosaran, E., Larsen, K. B., Hua, R., Sargent, G., Wang, Y., Kim, S., Lamark, T., Jauregui, M., Law, K., Lippincott-Schwartz, J., Brech, A., Johansen, T., & Kim, P. K. (2012b). NBR1 acts as an autophagy receptor for peroxisomes. Journal of Cell Science, jcs.114819. https://doi.org/10.1242/jcs.114819

Di Cara, F., Sheshachalam, A., Braverman, N. E., Rachubinski, R. A., & Simmonds, A. J. (2017). Peroxisome-mediated metabolism is required for immune response to microbial infection. Immunity, 47(1), 93-106.e7. https://doi.org/10.1016/j.immuni.2017.06.016

Dixit, E., Boulant, S., Zhang, Y., Lee, A. S. Y., Odendall, C., Shum, B., Hacohen, N., Chen, Z. J., Whelan, S. P., Fransen, M., Nibert, M. L., Superti-Furga, G., & Kagan, J. C. (2010). Peroxisomes are signaling platforms for antiviral innate immunity. Cell, 141(4), 668–681. https://doi.org/10.1016/j.cell.2010.04.018

Dobin, A., Davis, C. A., Schlesinger, F., Drenkow, J., Zaleski, C., Jha, S., Batut, P., Chaisson, M., & Gingeras, T. R. (2013). STAR: Ultrafast universal RNA-seq aligner. Bioinformatics (Oxford, England), 29(1), 15–21. https://doi.org/10.1093/bioinformatics/bts635

Drocourt, D., Calmels, T., Reynes, J.-P., Baron, M., & Tiraby, G. (1990). Cassettes of the Streptoalloteichus hindustanus ble gene for transformation of lower and higher eukaryotes to phleomycin resistance. Nucleic Acids Research, 18(13), 4009–4009. https://doi.org/10.1093/nar/18.13.4009

Dubreuil, M. M., Morgens, D. W., Okumoto, K., Honsho, M., Contrepois, K., Lee-McMullen, B., Traber, G. M., Sood, R. S., Dixon, S. J., Snyder, M. P., Fujiki, Y., & Bassik, M. C. (2020). Systematic identification of regulators of oxidative stress reveals non-canonical roles for peroxisomal import and the pentose phosphate pathway. Cell Reports, 30(5), 1417-1433.e7. https://doi.org/10.1016/j.celrep.2020.01.013

Elgersma, Y., & Tabak, H. F. (1996). Proteins involved in peroxisome biogenesis and functioning. Biochimica et Biophysica Acta (BBA) - Reviews on Biomembranes, 1286(3), 269–283. https://doi.org/10.1016/S0304-4157(96)00012-3

Evrard, P., Caviness, V. S., Prats-Vinas, J., & Lyon, G. (1978). The mechanism of arrest of neuronal migration in the Zellweger malformation: An hypothesis based upon cytoarchitectonic analysis. Acta Neuropathologica, 41(2), 109–117. https://doi.org/10.1007/BF00689761

Gehm, B. D., Kuo, W. L., Perlman, R. K., & Rosner, M. R. (1993). Mutations in a zinc-binding domain of human insulin-degrading enzyme eliminate catalytic activity but not insulin binding. The Journal of Biological Chemistry, 268(11), 7943–7948.

Gerö, D., Szoleczky, P., Chatzianastasiou, A., Papapetropoulos, A., & Szabo, C. (2014). Modulation of poly(Adp-ribose) polymerase-1 (PARP-1)-mediated oxidative cell injury by ring finger protein 146 (Rnf146) in cardiac myocytes. Molecular Medicine, 20(1), 313–328. https://doi.org/10.2119/molmed.2014.00102

Gilbert, L. A., Horlbeck, M. A., Adamson, B., Villalta, J. E., Chen, Y., Whitehead, E. H., Guimaraes, C., Panning, B., Ploegh, H. L., Bassik, M. C., Qi, L. S., Kampmann, M., & Weissman, J. S. (2014). Genome-scale crispr-mediated control of gene repression and activation. Cell, 159(3), 647–661. https://doi.org/10.1016/j.cell.2014.09.029

Guettler, S., LaRose, J., Petsalaki, E., Gish, G., Scotter, A., Pawson, T., Rottapel, R., & Sicheri, F. (2011). Structural basis and sequence rules for substrate recognition by tankyrase explain the basis for cherubism disease. Cell, 147(6), 1340–1354. https://doi.org/10.1016/j.cell.2011.10.046

Horlbeck, M. A., Gilbert, L. A., Villalta, J. E., Adamson, B., Pak, R. A., Chen, Y., Fields, A. P., Park, C. Y., Corn, J. E., Kampmann, M., & Weissman, J. S. (2016). Compact and highly active next-generation libraries for CRISPR-mediated gene repression and activation. eLife, 5, e19760. https://doi.org/10.7554/eLife.19760

Huang, S.-M. A., Mishina, Y. M., Liu, S., Cheung, A., Stegmeier, F., Michaud, G. A., Charlat, O., Wiellette, E., Zhang, Y., Wiessner, S., Hild, M., Shi, X., Wilson, C. J., Mickanin, C., Myer, V., Fazal, A., Tomlinson, R., Serluca, F., Shao, W., … Cong, F. (2009). Tankyrase inhibition stabilizes axin and antagonizes Wnt signalling. Nature, 461(7264), 614–620. https://doi.org/10.1038/nature08356

Hulse, R. E., Ralat, L. A., & Wei-Jen, T. (2009). Structure, function, and regulation of insulin-degrading enzyme. Vitamins and Hormones, 80, 635–648. https://doi.org/10.1016/S0083-6729(08)00622-5

Ito, M., Ito, R., Huang, Y., Miura, S., Imamura, A., Suzuki, Y., & Shimozawa, N. (2000). Rapid isolation and characterization of CHO mutants deficient in peroxisome biogenesis using the peroxisomal forms of fluorescent proteins. Biochimica et Biophysica Acta (BBA) - Molecular Cell Research, 1496(2–3), 232–242. https://doi.org/10.1016/S0167-4889(00)00019-7

Jain, I. H., Calvo, S. E., Markhard, A. L., Skinner, O. S., To, T.-L., Ast, T., & Mootha, V. K. (2020). Genetic screen for cell fitness in high or low oxygen highlights mitochondrial and lipid metabolism. Cell, 181(3), 716-727.e11. https://doi.org/10.1016/j.cell.2020.03.029

Kampmann, M., Bassik, M. C., & Weissman, J. S. (2014). Functional genomics platform for pooled screening and generation of mammalian genetic interaction maps. Nature Protocols, 9(8), 1825–1847. https://doi.org/10.1038/nprot.2014.103

Kang, H. C., Lee, Y.-I., Shin, J.-H., Andrabi, S. A., Chi, Z., Gagné, J.-P., Lee, Y., Ko, H. S., Lee, B. D., Poirier, G. G., Dawson, V. L., & Dawson, T. M. (2011). Iduna is a poly(ADP-ribose) (Par)-dependent E3 ubiquitin ligase that regulates DNA damage. Proceedings of the National Academy of Sciences, 108(34), 14103–14108. https://doi.org/10.1073/pnas.1108799108

Kim, P. K., Hailey, D. W., Mullen, R. T., & Lippincott-Schwartz, J. (2008a). Ubiquitin signals autophagic degradation of cytosolic proteins and peroxisomes. Proceedings of the National Academy of Sciences, 105(52), 20567–20574. https://doi.org/10.1073/pnas.0810611105

Kim, P. K., Hailey, D. W., Mullen, R. T., & Lippincott-Schwartz, J. (2008b). Ubiquitin signals autophagic degradation of cytosolic proteins and peroxisomes. Proceedings of the National Academy of Sciences, 105(52), 20567–20574. https://doi.org/10.1073/pnas.0810611105

Koch, J., Pranjic, K., Huber, A., Ellinger, A., Hartig, A., Kragler, F., & Brocard, C. (2010a). PEX11 family members are membrane elongation factors that coordinate peroxisome proliferation and maintenance. Journal of Cell Science, 123(19), 3389–3400. https://doi.org/10.1242/jcs.064907

Koch, J., Pranjic, K., Huber, A., Ellinger, A., Hartig, A., Kragler, F., & Brocard, C. (2010b). PEX11 family members are membrane elongation factors that coordinate peroxisome proliferation and maintenance. Journal of Cell Science, 123(Pt 19), 3389–3400. https://doi.org/10.1242/jcs.064907

Kocherlakota, S., Das, Y., Swinkels, D., Vanmunster, M., Callens, M., Vinckier, S., Vaz, F. M., Sinha, D., Van Veldhoven, P. P., Fransen, M., & Baes, M. (2023). The murine retinal pigment epithelium requires peroxisomal β-oxidation to maintain lysosomal function and prevent dedifferentiation. Proceedings of the National Academy of Sciences, 120(43), e2301733120. https://doi.org/10.1073/pnas.2301733120

Koutnikova, H. (1998). Maturation of wild-type and mutated frataxin by the mitochondrial processing peptidase. Human Molecular Genetics, 7(9), 1485–1489. https://doi.org/10.1093/hmg/7.9.1485

Kurochkin, I. V. (2001). Insulin-degrading enzyme: Embarking on amyloid destruction. Trends in Biochemical Sciences, 26(7), 421–425. https://doi.org/10.1016/S0968-0004(01)01876-X

Lach, R. S., Qiu, C., Kajbaf, E. Z., Baxter, N., Han, D., Wang, A., Lock, H., Chirikian, O., Pruitt, B., & Wilson, M. Z. (2022). Nucleation of the destruction complex on the centrosome accelerates degradation of β-catenin and regulates Wnt signal transmission. Proceedings of the National Academy of Sciences, 119(36), e2204688119. https://doi.org/10.1073/pnas.2204688119

Lametschwandtner, G., Brocard, C., Fransen, M., Van Veldhoven, P., Berger, J., & Hartig, A. (1998). The difference in recognition of terminal tripeptides as peroxisomal targeting signal 1 between yeast and human is due to different affinities of their receptor Pex5p to the cognate signal and to residues adjacent to it. The Journal of Biological Chemistry, 273(50), 33635–33643. https://doi.org/10.1074/jbc.273.50.33635

Levaot, N., Voytyuk, O., Dimitriou, I., Sircoulomb, F., Chandrakumar, A., Deckert, M., Krzyzanowski, P. M., Scotter, A., Gu, S., Janmohamed, S., Cong, F., Simoncic, P. D., Ueki, Y., La Rose, J., & Rottapel, R. (2011). Loss of tankyrase-mediated destruction of 3bp2 is the underlying pathogenic mechanism of cherubism. Cell, 147(6), 1324–1339. https://doi.org/10.1016/j.cell.2011.10.045

Li, W., Han, Q., Zhu, Y., Zhou, Y., Zhang, J., Wu, W., Li, Y., Liu, L., Qiu, Y., Hu, K., & Yin, D. (2023). SUMOylation of RNF146 results in Axin degradation and activation of Wnt/β-catenin signaling to promote the progression of hepatocellular carcinoma. Oncogene, 42(21), 1728–1740. https://doi.org/10.1038/s41388-023-02689-4

Li, X., Han, H., Zhou, M.-T., Yang, B., Ta, A. P., Li, N., Chen, J., & Wang, W. (2017). Proteomic analysis of the human tankyrase protein interaction network reveals its role in pexophagy. Cell Reports, 20(3), 737–749. https://doi.org/10.1016/j.celrep.2017.06.077

Lian, X., Hsiao, C., Wilson, G., Zhu, K., Hazeltine, L. B., Azarin, S. M., Raval, K. K., Zhang, J., Kamp, T. J., & Palecek, S. P. (2012). Robust cardiomyocyte differentiation from human pluripotent stem cells via temporal modulation of canonical Wnt signaling. Proceedings of the National Academy of Sciences of the United States of America, 109(27), E1848-1857. https://doi.org/10.1073/pnas.1200250109

Liang, J. R., Lingeman, E., Ahmed, S., & Corn, J. E. (2018). Atlastins remodel the endoplasmic reticulum for selective autophagy. Journal of Cell Biology, 217(10), 3354–3367. https://doi.org/10.1083/jcb.201804185

Lin, Y., Cradick, T. J., Brown, M. T., Deshmukh, H., Ranjan, P., Sarode, N., Wile, B. M., Vertino, P. M., Stewart, F. J., & Bao, G. (2014). CRISPR/Cas9 systems have off-target activity with insertions or deletions between target DNA and guide RNA sequences. Nucleic Acids Research, 42(11), 7473–7485. https://doi.org/10.1093/nar/gku402

Liu, J., Xiao, Q., Xiao, J., Niu, C., Li, Y., Zhang, X., Zhou, Z., Shu, G., & Yin, G. (2022). Wnt/β-catenin signalling: Function, biological mechanisms, and therapeutic opportunities. Signal Transduction and Targeted Therapy, 7(1), 3. https://doi.org/10.1038/s41392-021-00762-6

Love, M. I., Huber, W., & Anders, S. (2014). Moderated estimation of fold change and dispersion for RNA-seq data with DESeq2. Genome Biology, 15(12), 550. https://doi.org/10.1186/s13059-014-0550-8

Luiken, J. J., van den Berg, M., Heikoop, J. C., & Meijer, A. J. (1992). Autophagic degradation of peroxisomes in isolated rat hepatocytes. FEBS Letters, 304(1), 93–97. https://doi.org/10.1016/0014-5793(92)80596-9

Machon, O., Backman, M., Machonova, O., Kozmik, Z., Vacik, T., Andersen, L., & Krauss, S. (2007). A dynamic gradient of Wnt signaling controls initiation of neurogenesis in the mammalian cortex and cellular specification in the hippocampus. Developmental Biology, 311(1), 223–237. https://doi.org/10.1016/j.ydbio.2007.08.038

Malito, E., Ralat, L. A., Manolopoulou, M., Tsay, J. L., Wadlington, N. L., & Tang, W.-J. (2008). Molecular bases for the recognition of short peptide substrates and cysteine-directed modifications of human insulin-degrading enzyme. Biochemistry, 47(48), 12822–12834. https://doi.org/10.1021/bi801192h

Manner, A., & Islinger, M. (2017). Isolation of peroxisomes from rat liver and cultured hepatoma cells by density gradient centrifugation. Methods in Molecular Biology (Clifton, N.J.), 1595, 1–11. https://doi.org/10.1007/978-1-4939-6937-1_1

Martino-Echarri, E., Brocardo, M. G., Mills, K. M., & Henderson, B. R. (2016). Tankyrase inhibitors stimulate the ability of tankyrases to bind axin and drive assembly of β-catenin degradation-competent axin puncta. PLOS ONE, 11(3), e0150484. https://doi.org/10.1371/journal.pone.0150484

Matsui, S., Funahashi, M., Honda, A., & Shimozawa, N. (2013). Newly identified milder phenotype of peroxisome biogenesis disorder caused by mutated PEX3 gene. Brain & Development, 35(9), 842–848. https://doi.org/10.1016/j.braindev.2012.10.017

Matsumoto, Y., Larose, J., Kent, O. A., Lim, M., Changoor, A., Zhang, L., Storozhuk, Y., Mao, X., Grynpas, M. D., Cong, F., & Rottapel, R. (2017). RANKL coordinates multiple osteoclastogenic pathways by regulating expression of ubiquitin ligase RNF146. Journal of Clinical Investigation, 127(4), 1303–1315. https://doi.org/10.1172/JCI90527

Menendez, L., Kulik, M. J., Page, A. T., Park, S. S., Lauderdale, J. D., Cunningham, M. L., & Dalton, S. (2013). Directed differentiation of human pluripotent cells to neural crest stem cells. Nature Protocols, 8(1), 203–212. https://doi.org/10.1038/nprot.2012.156

Mignarri, A., Vinciguerra, C., Giorgio, A., Ferdinandusse, S., Waterham, H., Wanders, R., Bertini, E., Dotti, M. T., & Federico, A. (2012). Zellweger spectrum disorder with mild phenotype caused by pex2 gene mutations. JIMD Reports, 6, 43–46. https://doi.org/10.1007/8904_2011_102

Morand, O., Allen, L., Zoeller, R., & Raetz, C. (1990). A rapid selection for animal cell mutants with defective peroxisomes. Biochimica et Biophysica Acta (BBA) - General Subjects, 1034(2), 132–141. https://doi.org/10.1016/0304-4165(90)90066-6

Morin, P. J., Sparks, A. B., Korinek, V., Barker, N., Clevers, H., Vogelstein, B., & Kinzler, K. W. (1997). Activation of β-catenin-tcf signaling in colon cancer by mutations in β-catenin or apc. Science, 275(5307), 1787–1790. https://doi.org/10.1126/science.275.5307.1787

Morvay, P. L., Baes, M., & Van Veldhoven, P. P. (2017). Differential activities of peroxisomes along the mouse intestinal epithelium. Cell Biochemistry and Function, 35(3), 144–155. https://doi.org/10.1002/cbf.3255

Murray, V., Chen, J. K., & Galea, A. M. (2014). The anti-tumor drug bleomycin preferentially cleaves at the transcription start sites of actively transcribed genes in human cells. Cellular and Molecular Life Sciences, 71(8), 1505–1512. https://doi.org/10.1007/s00018-013-1456-4

Nie, L., Wang, C., Li, N., Feng, X., Lee, N., Su, D., Tang, M., Yao, F., & Chen, J. (2020). Proteome-wide analysis reveals substrates of e3 ligase rnf146 targeted for degradation. Molecular & Cellular Proteomics, 19(12), 2015–2030. https://doi.org/10.1074/mcp.RA120.002290

Nuttall, J. M., Motley, A. M., & Hettema, E. H. (2014). Deficiency of the exportomer components Pex1, Pex6, and Pex15 causes enhanced pexophagy in Saccharomyces cerevisiae. Autophagy, 10(5), 835–845. https://doi.org/10.4161/auto.28259

Olivieri, M., Cho, T., Álvarez-Quilón, A., Li, K., Schellenberg, M. J., Zimmermann, M., Hustedt, N., Rossi, S. E., Adam, S., Melo, H., Heijink, A. M., Sastre-Moreno, G., Moatti, N., Szilard, R. K., McEwan, A., Ling, A. K., Serrano-Benitez, A., Ubhi, T., Feng, S., … Durocher, D. (2020). A genetic map of the response to dna damage in human cells. Cell, 182(2), 481-496.e21. https://doi.org/10.1016/j.cell.2020.05.040

Ossendorp, B. C., & Wirtz, K. W. (1993). The non-specific lipid-transfer protein (Sterol carrier protein 2) and its relationship to peroxisomes. Biochimie, 75(3–4), 191–200. https://doi.org/10.1016/0300-9084(93)90077-6

Platta, H. W., El Magraoui, F., Bäumer, B. E., Schlee, D., Girzalsky, W., & Erdmann, R. (2009a). Pex2 and pex12 function as protein-ubiquitin ligases in peroxisomal protein import. Molecular and Cellular Biology, 29(20), 5505–5516. https://doi.org/10.1128/MCB.00388-09

Platta, H. W., El Magraoui, F., Bäumer, B. E., Schlee, D., Girzalsky, W., & Erdmann, R. (2009b). Pex2 and pex12 function as protein-ubiquitin ligases in peroxisomal protein import. Molecular and Cellular Biology, 29(20), 5505–5516. https://doi.org/10.1128/MCB.00388-09

Platta, H. W., Grunau, S., Rosenkranz, K., Girzalsky, W., & Erdmann, R. (2005). Functional role of the AAA peroxins in dislocation of the cycling PTS1 receptor back to the cytosol. Nature Cell Biology, 7(8), 817–822. https://doi.org/10.1038/ncb1281

Pollock, K., Ranes, M., Collins, I., & Guettler, S. (2017). Identifying and validating tankyrase binders and substrates: A candidate approach. Methods in Molecular Biology (Clifton, N.J.), 1608, 445–473. https://doi.org/10.1007/978-1-4939-6993-7_28

Putri, G. H., Anders, S., Pyl, P. T., Pimanda, J. E., & Zanini, F. (2022). Analysing high-throughput sequencing data in Python with HTSeq 2.0. Bioinformatics, 38(10), 2943–2945. https://doi.org/10.1093/bioinformatics/btac166

Schrader, T. A., Carmichael, R. E., Islinger, M., Costello, J. L., Hacker, C., Bonekamp, N. A., Weishaupt, J. H., Andersen, P. M., & Schrader, M. (2022). PEX11β and FIS1 cooperate in peroxisome division independently of mitochondrial fission factor. Journal of Cell Science, 135(13), jcs259924. https://doi.org/10.1242/jcs.259924

Shen, Q., Wang, Y., Dimos, J. T., Fasano, C. A., Phoenix, T. N., Lemischka, I. R., Ivanova, N. B., Stifani, S., Morrisey, E. E., & Temple, S. (2006). The timing of cortical neurogenesis is encoded within lineages of individual progenitor cells. Nature Neuroscience, 9(6), 743–751. https://doi.org/10.1038/nn1694

Sheng, Z., Xu, Y., Wang, S., Yuan, Y., Huang, T., & Lu, P. (2018). XPO1-mediated nuclear export of RNF146 protects from angiotensin II-induced endothelial cellular injury. Biochemical and Biophysical Research Communications, 503(3), 1544–1549. https://doi.org/10.1016/j.bbrc.2018.07.077

Shpilka, T., Naresh, N. U., Du, Y., Watts, J. L., & Haynes, C. M. (2022). ATFS-1 regulates peroxisome assembly genes and protects both mitochondria and peroxisomes during peroxin perturbations. https://doi.org/10.1101/2022.09.09.507280

Skowyra, M. L., & Rapoport, T. A. (2022). PEX5 translocation into and out of peroxisomes drives matrix protein import. Molecular Cell, 82(17), 3209-3225.e7. https://doi.org/10.1016/j.molcel.2022.07.004

Song, E. S., Cady, C., Fried, M. G., & Hersh, L. B. (2006). Proteolytic fragments of insulysin (Ide) retain substrate binding but lose allosteric regulation. Biochemistry, 45(50), 15085–15091. https://doi.org/10.1021/bi061298u

Stiebler, A. C., Freitag, J., Schink, K. O., Stehlik, T., Tillmann, B. A. M., Ast, J., & Bölker, M. (2014). Ribosomal readthrough at a short uga stop codon context triggers dual localization of metabolic enzymes in fungi and animals. PLoS Genetics, 10(10), e1004685. https://doi.org/10.1371/journal.pgen.1004685

Stirling, D. R., Swain-Bowden, M. J., Lucas, A. M., Carpenter, A. E., Cimini, B. A., & Goodman, A. (2021a). CellProfiler 4: Improvements in speed, utility and usability. BMC Bioinformatics, 22(1), 433. https://doi.org/10.1186/s12859-021-04344-9

Stirling, D. R., Swain-Bowden, M. J., Lucas, A. M., Carpenter, A. E., Cimini, B. A., & Goodman, A. (2021b). CellProfiler 4: Improvements in speed, utility and usability. BMC Bioinformatics, 22(1), 433. https://doi.org/10.1186/s12859-021-04344-9

Teixeira, P. F., & Glaser, E. (2013). Processing peptidases in mitochondria and chloroplasts. Biochimica Et Biophysica Acta, 1833(2), 360–370. https://doi.org/10.1016/j.bbamcr.2012.03.012

Thoms, S., Harms, I., Kalies, K.-U., & Gärtner, J. (2012). Peroxisome formation requires the endoplasmic reticulum channel protein Sec61. Traffic (Copenhagen, Denmark), 13(4), 599–609. https://doi.org/10.1111/j.1600-0854.2011.01324.x

Thorvaldsen, T. E., Pedersen, N. M., Wenzel, E. M., Schultz, S. W., Brech, A., Liestøl, K., Waaler, J., Krauss, S., & Stenmark, H. (2015). Structure, dynamics, and functionality of tankyrase inhibitor-induced degradasomes. Molecular Cancer Research, 13(11), 1487–1501. https://doi.org/10.1158/1541-7786.MCR-15-0125

Titorenko, V. (2001). Dynamics of peroxisome assembly and function. Trends in Cell Biology, 11(1), 22–29. https://doi.org/10.1016/S0962-8924(00)01865-1

Tsai, S. Q., Wyvekens, N., Khayter, C., Foden, J. A., Thapar, V., Reyon, D., Goodwin, M. J., Aryee, M. J., & Joung, J. K. (2014). Dimeric CRISPR RNA-guided FokI nucleases for highly specific genome editing. Nature Biotechnology, 32(6), 569–576. https://doi.org/10.1038/nbt.2908

Tsukamoto, T., Yokota, S., & Fujiki, Y. (1990). Isolation and characterization of Chinese hamster ovary cell mutants defective in assembly of peroxisomes. The Journal of Cell Biology, 110(3), 651–660. https://doi.org/10.1083/jcb.110.3.651

van Zutphen, T., Baerends, R. J. S., Susanna, K. A., de Jong, A., Kuipers, O. P., Veenhuis, M., & van der Klei, I. J. (2010). Adaptation of Hansenula polymorpha to methanol: A transcriptome analysis. BMC Genomics, 11, 1. https://doi.org/10.1186/1471-2164-11-1

Veeman, M. T., Slusarski, D. C., Kaykas, A., Louie, S. H., & Moon, R. T. (2003). Zebrafish prickle, a modulator of noncanonical wnt/fz signaling, regulates gastrulation movements. Current Biology, 13(8), 680–685. https://doi.org/10.1016/S0960-9822(03)00240-9

Volpe, J. J., & Adams, R. D. (1972). Cerebro-hepato-renal syndrome of Zellweger: An inherited disorder of neuronal migration. Acta Neuropathologica, 20(3), 175–198. https://doi.org/10.1007/BF00686900

Wanders, R. J. A. (2004). Metabolic and molecular basis of peroxisomal disorders: A review. American Journal of Medical Genetics. Part A, 126A(4), 355–375. https://doi.org/10.1002/ajmg.a.20661

Wanders, R. J. A., & Waterham, H. R. (2006). Biochemistry of mammalian peroxisomes revisited. Annual Review of Biochemistry, 75(1), 295–332. https://doi.org/10.1146/annurev.biochem.74.082803.133329

Weir, N. R., Kamber, R. A., Martenson, J. S., & Denic, V. (2017). The AAA protein Msp1 mediates clearance of excess tail-anchored proteins from the peroxisomal membrane. eLife, 6, e28507. https://doi.org/10.7554/eLife.28507

Wienert, B., Wyman, S. K., Richardson, C. D., Yeh, C. D., Akcakaya, P., Porritt, M. J., Morlock, M., Vu, J. T., Kazane, K. R., Watry, H. L., Judge, L. M., Conklin, B. R., Maresca, M., & Corn, J. E. (2019). Unbiased detection of CRISPR off-targets in vivo using DISCOVER-Seq. Science (New York, N.Y.), 364(6437), 286–289. https://doi.org/10.1126/science.aav9023

Wilhelm, L. P., Zapata-Muñoz, J., Villarejo-Zori, B., Pellegrin, S., Freire, C. M., Toye, A. M., Boya, P., & Ganley, I. G. (2022). bnip3l / nix regulates both mitophagy and pexophagy. The EMBO Journal, 41(24), e111115. https://doi.org/10.15252/embj.2022111115

Xu, H., Luo, P., Zhao, Y., Zhao, M., Yang, Y., Chen, T., Huo, K., Han, H., & Fei, Z. (2013). Iduna protects HT22 cells from hydrogen peroxide-induced oxidative stress through interfering poly(ADP-ribose) polymerase-1-induced cell death (Parthanatos). Cellular Signalling, 25(4), 1018–1026. https://doi.org/10.1016/j.cellsig.2013.01.006

Xu, Y.-R., Shi, M.-L., Zhang, Y., Kong, N., Wang, C., Xiao, Y.-F., Du, S.-S., Zhu, Q.-Y., & Lei, C.-Q. (2022). Tankyrases inhibit innate antiviral response by PARylating VISA/MAVS and priming it for RNF146-mediated ubiquitination and degradation. Proceedings of the National Academy of Sciences, 119(26), e2122805119. https://doi.org/10.1073/pnas.2122805119

Yagita, Y., Abe, Y., & Fujiki, Y. (2022). De novo formation and maintenance of mammalian peroxisomes in the absence of pex16. Journal of Cell Science, jcs.258377. https://doi.org/10.1242/jcs.258377

Yeh, T.-Y. J., Beiswenger, K. K., Li, P., Bolin, K. E., Lee, R. M., Tsao, T.-S., Murphy, A. N., Hevener, A. L., & Chi, N.-W. (2009). Hypermetabolism, hyperphagia, and reduced adiposity in tankyrase-deficient mice. Diabetes, 58(11), 2476–2485. https://doi.org/10.2337/db08-1781

Yue, X., Tiwari, N., Zhu, L., Ngo, H. D. T., Lim, J.-M., Gim, B., Jing, S., Wang, Y., Qian, Y., & Lee, I. (2021). Tankyrase-1-mediated degradation of Golgin45 regulates glycosyltransferase trafficking and protein glycosylation in Rab2-GTP-dependent manner. Communications Biology, 4(1), 1370. https://doi.org/10.1038/s42003-021-02899-0

Zhang, J., Tripathi, D. N., Jing, J., Alexander, A., Kim, J., Powell, R. T., Dere, R., Tait-Mulder, J., Lee, J.-H., Paull, T. T., Pandita, R. K., Charaka, V. K., Pandita, T. K., Kastan, M. B., & Walker, C. L. (2015a). ATM functions at the peroxisome to induce pexophagy in response to ROS. Nature Cell Biology, 17(10), 1259–1269. https://doi.org/10.1038/ncb3230

Zhang, J., Tripathi, D. N., Jing, J., Alexander, A., Kim, J., Powell, R. T., Dere, R., Tait-Mulder, J., Lee, J.-H., Paull, T. T., Pandita, R. K., Charaka, V. K., Pandita, T. K., Kastan, M. B., & Walker, C. L. (2015b). ATM functions at the peroxisome to induce pexophagy in response to ROS. Nature Cell Biology, 17(10), 1259–1269. https://doi.org/10.1038/ncb3230

Zhang, Y., Liu, S., Mickanin, C., Feng, Y., Charlat, O., Michaud, G. A., Schirle, M., Shi, X., Hild, M., Bauer, A., Myer, V. E., Finan, P. M., Porter, J. A., Huang, S.-M. A., & Cong, F. (2011). RNF146 is a poly(ADP-ribose)-directed E3 ligase that regulates axin degradation and Wnt signalling. Nature Cell Biology, 13(5), 623–629. https://doi.org/10.1038/ncb2222

Zheng, J., Chen, X., Liu, Q., Zhong, G., & Zhuang, M. (2022a). Ubiquitin ligase MARCH5 localizes to peroxisomes to regulate pexophagy. Journal of Cell Biology, 221(1), e202103156. https://doi.org/10.1083/jcb.202103156

Zheng, J., Chen, X., Liu, Q., Zhong, G., & Zhuang, M. (2022b). Ubiquitin ligase MARCH5 localizes to peroxisomes to regulate pexophagy. Journal of Cell Biology, 221(1), e202103156. https://doi.org/10.1083/jcb.202103156

Zheng, J., Chen, X., Liu, Q., Zhong, G., & Zhuang, M. (2022c). Ubiquitin ligase MARCH5 localizes to peroxisomes to regulate pexophagy. Journal of Cell Biology, 221(1), e202103156. https://doi.org/10.1083/jcb.202103156

Zoeller, R. A., & Raetz, C. R. (1986). Isolation of animal cell mutants deficient in plasmalogen biosynthesis and peroxisome assembly. Proceedings of the National Academy of Sciences, 83(14), 5170–5174. https://doi.org/10.1073/pnas.83.14.5170